ABSTRACT

Title of dissertation:	The Study and Development of Automatic Data Acquisition System for Spin-Stand Imaging and Drive Independent Recovery of Hard Disk Data
	Chun-Yang Tseng, Ph.D., 2007
Dissertation directed by:	Professor Isaak D. Mayergoyz
	Department of Electrical and Computer Engineering

In this thesis, an automatic data acquisition system for spin-stand imaging and drive independent data recovery is developed. This system enables a user to perform data acquisition of on-track hard disk data by using a commercial spin-stand. At the heart of this system are the three techniques: the track-centering technique, the dynamic track-following technique and the servo-based track-following technique.

By using the track-centering technique, we are able to efficiently make the center of the prewritten data tracks coincide with the rotational center of the spin-stand spindle so that the track eccentricity can be eliminated. Both the dynamic track-following and servo-based track-following techniques utilize a small piezoelectric actuator (PZT) as the micro-positioning device. The former is of an open-loop controlling scheme, and the desired tracking trajectory is extracted from the whole-track spin-stand images. The latter is of a closed-loop feedback control scheme, and the feedback signals are from the existing servo patterns on the disk. The former deals with PZT hysteresis by using a special algorithm based on the Preisach model while the approach taken by the latter is

based on iterative compensation.

By using the developed techniques, we are able to perform spin-stand microscopy on hard disks with longitudinal and perpendicular modes of recording taken from latest commercial hard disk drives (HDDs) with ultra-high areal densities (as high as 131.5 Gbits/in^2). The automatic data acquisition system has been successfully applied to recover actual hard disk data from failed HDDs.

The Study and Development of Automatic Data Acquisition System for Spin-Stand Imaging and Drive Independent Recovery of Hard Disk Data

by

Chun-Yang Tseng

Dissertation submitted to the Faculty of the Graduate School of the
University of Maryland, College Park in partial fulfillment
of the requirements for the degree of
Doctor of Philosophy
2007

Advisory Committee:

    Professor Isaak D. Mayergoyz, Chair/Advisor
    Professor P.S. Krishnaprasad
    Professor Romel D. Gomez
    Professor Thomas E. Murphy
    Professor Dianne P. O'Leary

DEDICATION

To my parents and family, for their love and continuous support
during the entire time of my graduate studies.

ACKNOWLEDGMENTS

First and foremost, I would like to give my thanks and respect to my advisor, Prof. Isaak Mayergoyz, for his prudent guidance, unceasing encouragement, and tremendous inspiration to me. Through these years of my thesis research with him, I have learned a lot not only from his distinguished scientific talent and knowledge but also from his highly respectable virtues. His firm resolution and fearlessness toward obstacles encountered in scientific research has left a strong impression in me. He is definitely a great pattern of an explorer of sciences. I feel very grateful and fortunate to be one of his students during my Ph. D studies.

I would also like to thank Dr. Charles Krafft for his advice and assistance for solving issues occurred in the research and experiments. I would like to acknowledge Dr. Chun Tse for introducing me to the spin-stand microscopy technique. I am grateful to Dr. Michael Dreyer for showing me the method of controlling the displacement of a piezoelectric actuator. I am indebted to Les Lorenz and Peter Krusen for helping me with the modification of the head cartridge of the spin-stand. I am also thankful to Lisa Lucas for instructing me to desolder magnetic recording heads from a commercial hard disk drive and to solder these heads with a proper interface for them to be functional on a spin-stand. Special thank to my fellow graduate student, Patrick McAvoy, with whom I endeavored on many challenging research projects.

I would like to especially thank my wife, I-Chun, for her continuous support and understanding. Finally, I would like to thank my parents for their support and encouragement during the entire time of my graduate studies.

TABLE OF CONTENTS

LIST OF FIGURES

LIST OF TABLES

LIST OF PUBLICATIONS

- C. Tse, C. Tseng, P. McAvoy, I. Mayergoyz, and C. Krafft, "Whole-track imaging and diagnostics of hard disk data using the spin-stand imaging technique," *J. Appl. Phys.*, vol. 97, 10P104, 2005.

- C. Tseng, I. Mayergoyz, C. Tse, P. McAvoy, and C. Krafft, "Dynamic following of off-centered hard disk tracks in spin-stand imaging," *J. Appl. Phys.*, vol. 97, 10R301, 2005.

- C. Tse, C. Krafft, I. Mayergoyz, P. McAvoy, and C. Y. Tseng, "Forensic recovery of hard disk data by using the spin-stand imaging technique," *Proc. SPIE*, vol. 5778, pp. 595–606, May 2005.

- I. Mayergoyz, P. McAvoy, C. Tse, C. Krafft, and C. Tseng, "The 2-D Hilbert transform in magnetic recording," *IEEE Trans. Magn.*, vol. 42, pp. 2282–2284, 2006.

- C. Tseng, I. Mayergoyz, and P. McAvoy, "Iterative compensation for hysteresis effects in tracking problems," accepted for presentation to the *6th International Symposium on Hysteresis Modeling and Micromagnetics*, Naples, Italy 4-6 June, 2007.

Chapter 1

Introduction

1.1 Technological evolution of hard disk drives

The first hard disk drive (HDD), called RAMAC (random access method of accounting and control), was invented by IBM in 1956 [1]. It was configured with 50 magnetic disks, each 24 inches in diameter, for a capacity of 5 megabytes. The whole unit was 60 inches long, 68 inches high and 29 inches deep. Nearly a half century later, one can put 5 gigabytes of data in his pocket with a micro drive. It is expected that 3.5-inch HDDs with capacity of more than 1 terabytes will be shipped to the market in 2007. Such tremendous progress has mainly resulted from the exponential increase of the areal density (the amount of user data stored per unit area of disk surface).

Figure 1.1 shows the areal density increase over the years in log scale. The areal density of the first HDD, RAMAC, was about 2000 bits/in^2. It can been seen that the
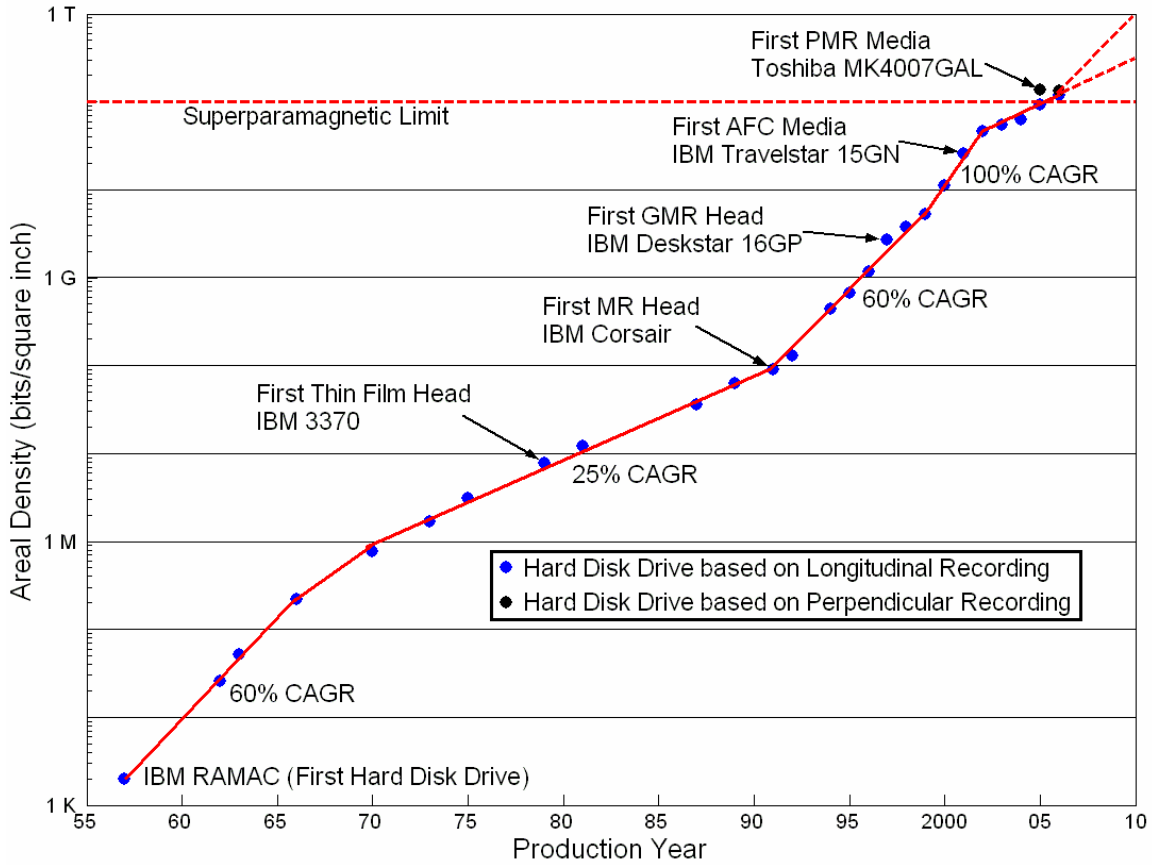
Figure 1.1: Areal density increase versus product year.

areal density was increasing at a compound annual growth rate (CAGR) of more than 60% during the first ten years of HDD history. Then, this rate gradually slowed down. Throughout the 1970s and the 1980s, the growth rate remained constant at 25%. With the introduction of the magnetoresistance (MR) heads in 1991, the rate increased to more than 60% again. Because of the introduction of the giant magnetoresistance (GMR) heads in the late 1990s, the CAGR has increased to more than 100% for a few years. However, the CAGR has slowed down since 2002 because the areal density has been approaching the limit of longitudinal recording imposed by the superparamagnetic effect, which occurs when the magnetic grains become so small that thermal fluctuation can cause the direction of magnetization to flip back and forth [2]-[4].

In 2005, Toshiba introduced the MK4007GAL, which is the first HDD based on perpendicular recording technology. Unlike conventional longitudinal recording which aligns the data bits horizontally, perpendicular recording aligns the data bits vertically. This revolutionary technology has turned another page in the HDD history since its recording scheme allows the superparamagnetic limit to be pushed further out. The MK4007GAL has an areal density of 136.15 Gbits/in^2, which is already beyond the superparamagnetic limit of longitudinal recording. Hitachi demonstrated an areal density of 230 Gbits/in^2 on perpendicular recording technology in March 2005 and expects to ship HDDs with such areal density in 2007 [5]. In September 2006, Seagate also announced the results of a magnetic recording demonstration, using perpendicular recording technology to achieve a world record of 421 Gbits/in^2 [6]. According to Fig. 1.1, we should see HDDs with areal density of more than 1 Tbits/in^2 shipping to the market in the 2010s.

In order to further increase the areal density, technologists are already beginning to explore other methods of recording data. In the future, heat-assisted magnetic recording (HAMR) and patterned media are considered to be the most likely candidates for extremely high recording densities. HAMR, which combines both magnetic and optical recording technology, was originally proposed by Katayama [7]-[8] and Saga [9] separately. The idea behind HAMR is to temporarily reduce the coercivity of the recording media by locally heating the media with a laser beam during the writing process. In this way, it is possible to write on high-coercivity recording media, which have higher stability against superparamagnetism, thus allowing for higher recording densities.

The concept of lithographically patterning a hard disk was originally introduced to improve head positioning and signal-to-noise ratio [10], but it has been drawing much more attention as a means of extending recording density [11]-[13]. A pattern medium consists of a regular array of magnetic discrete elements, each of which is a single domain with uniaxial magnetic anisotropy. The easy axis can be oriented parallel or perpendicular to the substrate. Each element stores one bit (depending on its magnetization state). Since each element acts as a single bounded domain, each element can theoretically contain a single magnetic grain and still remain thermally stable, instead of requiring many grains for one bit as the conventional thin film media do. As a result, patterned media offer the possibility of substantially extending the recording density [14]. It is expected that areal density as high as 300 Tbits/in^2 might be achievable by using perpendicular recording with HAMR on patterned media [15].

While HDD capacity has been significantly increasing due to the astonishing growth rate of areal density since the early 1990s, the cost of storing information on the unit area of disk surface has also been falling rapidly. Figure 1.2 compares the average price per megabyte of HDD, DRAM, flash and paper/film over the years [16]. For the past few years, it has been cheaper to store data on HDDs than on paper or film. It can also be seen that a megabyte of HDD storage is 50 to 100 times cheaper than a megabyte in a flash-memory card or DRAM chip. When one needs a lot of storage, a HDD is certainly the most economical choice. Because of the large capacity and low production cost, HDDs have been the dominant storage devices during the recent couple of decades. Nowadays, HDD technology can be found not only in personal computers but also in many other applications, including MP3 players, digital camcorders, GPS navigation systems, car

4

entertainment systems and mobile phones, with different form factors as their storage platforms.
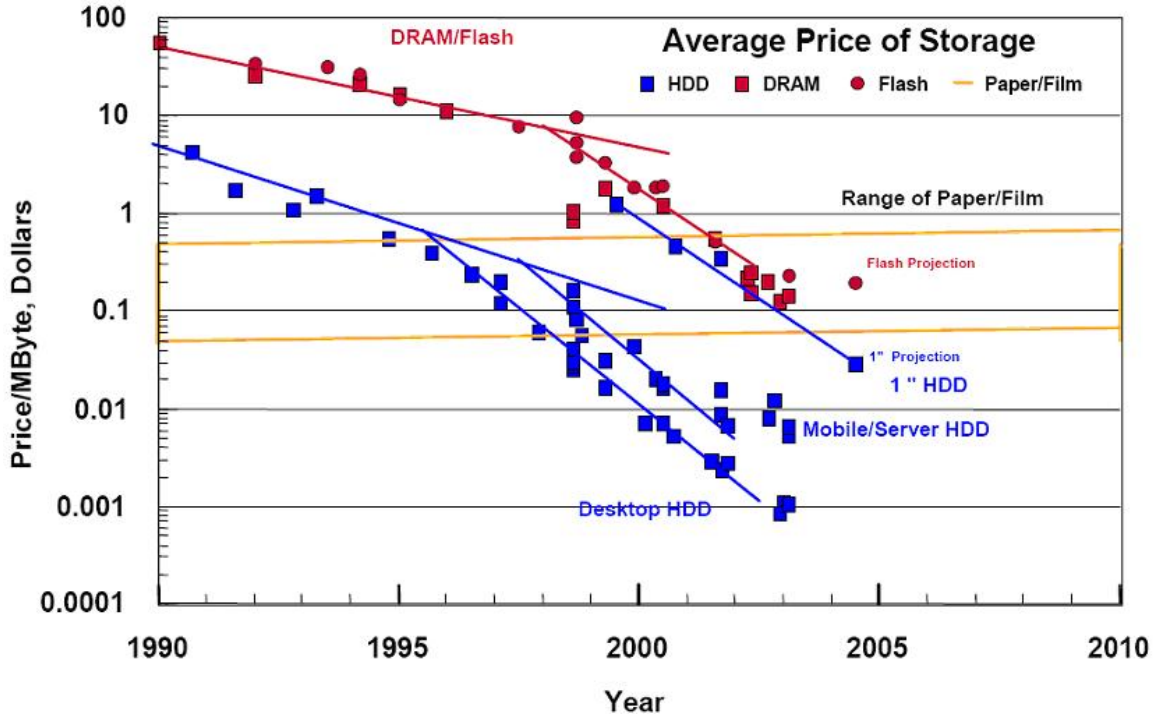
Figure 1.2: Average price of storage (from Hitachi Global Storage Technologies).

1.2 The spin-stand based magnetic microscopy

Magnetic microscopy, giving a detailed understanding of magnetism on the submicron or even nanometer scale, is a valuable tool for advancing magnetic recording technology. Since Martin and Wickramasinghe proposed the magnetic force microscopy (MFM) in 1987 [17], it has become the most popular microscopic technique for studying magnetization patterns on hard disks [18]-[24]. MFM utilizes a sharp magnetic tip as its sensor. By measuring the interaction between the tip and the sample, MFM can image the spatial variation of magnetic forces on a sample surface. However, although MFM has many advantages over many other magnetic imaging techniques, it has been realized that

5

MFM has many limitations such as low rate of image acquisition, limited image area and the difficulty of a complete separation of magnetic and non-magnetic forces.

In May 2000, Mayergoyz *et al.* proposed a new magnetic imaging technique on a spin-stand [25] that is freed from the limitations of MFM. A spin-stand is designed as a platform to hold and operate the magnetic media and head stack. One can write any particular data pattern on any specific location on the hard disk media on a spin-stand. The magnetic patterns written on the hard disk media can also be readily located and accessed. Because of the ease of use, a spin-stand has become an important tool in the study of magnetic recording. The HDD industry routinely utilizes spin-stands for testing heads, media and read channels. Extensive research on different aspects of magnetic recording has been performed on spin-stands [26]-[33]. Recently, a spin-stand is also recognized as a potent tool for the purpose of magnetic microscopy [25]. The spin-stand based magnetic microscopy technique can be used for various applications [34]-[41].

In this technique, the hard disk is scanned in both the along-track and cross-track directions by the read head of the spin-stand. As the spindle finishes one revolution of rotation, the read head will have also scanned one entire circumferential track. The readback signal from the read head can be accessed through a dedicated output port on the preamplifier board of the spin-stand. A data acquisition card is used to sample the readback signal. The sampled waveform is then sent to a personal computer through the data acquisition card. Rows of waveforms are acquired by microstepping the head in the cross-track direction. The target area is located by setting the trigger delay, the number of samples to be recorded, and the sampling rate of the data acquisition card. The drive index from the spindle of the spin-stand is used as the triggering signal. By piecing these
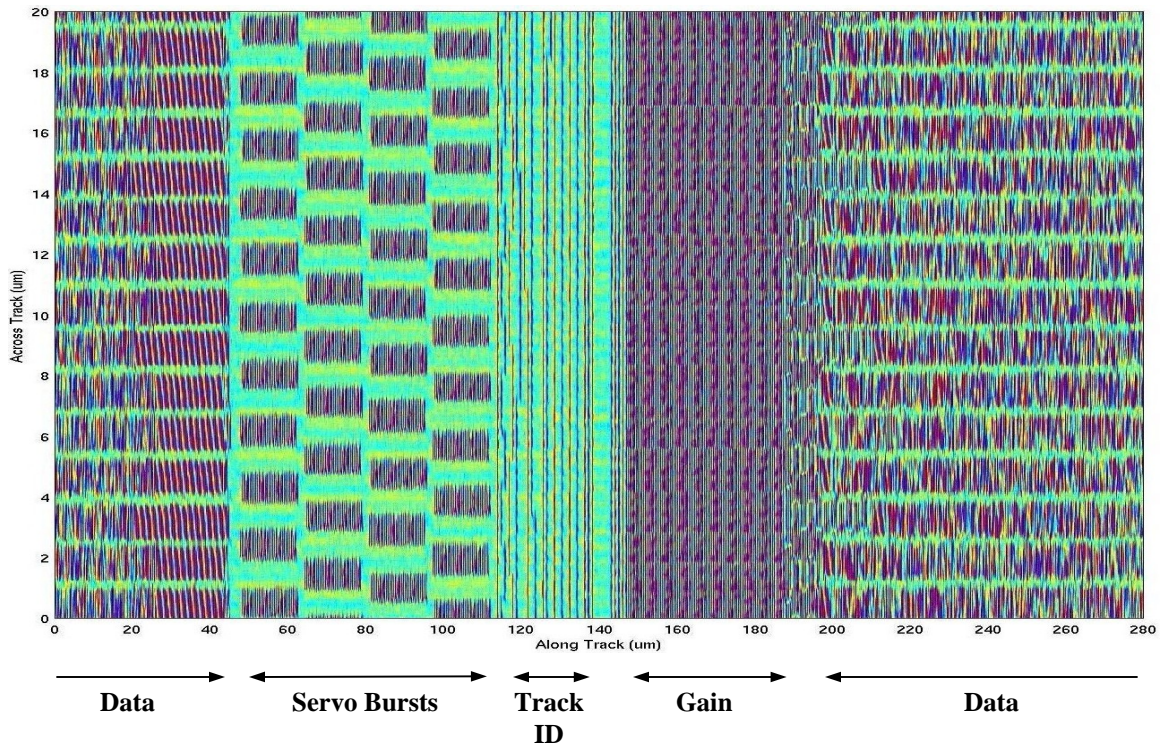
Figure 1.3: Spin-stand image of a commercial hard disk.

rows of waveforms together, the raw image of the target area is created. A numerical algorithm has been developed to offset any trigger-induced image shift. Figure 1.3 shows the magnetic microscopy of the servo data area, which includes the servo bursts, track-id, gain, and part of the user-data region [39].

The spin-stand based magnetic microscopy technique is a versatile tool. It has been applied to realize the transverse components of magnetization [36], characterize thermal relaxation of magnetization patterns [37] and study the effect of side erasure in perpendicular media [42]. Due to the dynamic mechanism of this technique, it is capable of imaging a large area of hard disk media with a high imaging rate, which is comparable to the data reading rate of an actual HDD. This unique feature allows for high-speed massive imaging of hard disk data [39], which can be used for the purpose of hard disk data recovery.

7

1.3 The need for drive-independent data recovery

While the majority of digitally-created information is stored in HDD-based storage devices, data loss due to logical or physical failures of HDDs has becomes a growing issue. Logical failures are usually a result of file system corruption, which can occur due to a virus attack or accidental deletion of some registry files. Data loss due to logical failures can be recovered with some off-the-shelf data recovery programs and the knowledge about the structure of the file system. In contrast, physical failures can result from a wide variety of causes and the recovery procedure is much more challenging. Common physical causes of data loss include power loss, power surge, overheating, electrostatic discharge and any kind of physical damage to the HDD components or medium. Figure 1.4 shows a photo of a HDD manufactured by Seagate with the cover opened. One can see that a HDD is mainly composed of the disk platters, spindle motor, read/write heads, read/write preamplifier, voice coil actuator assembly and printed circuit
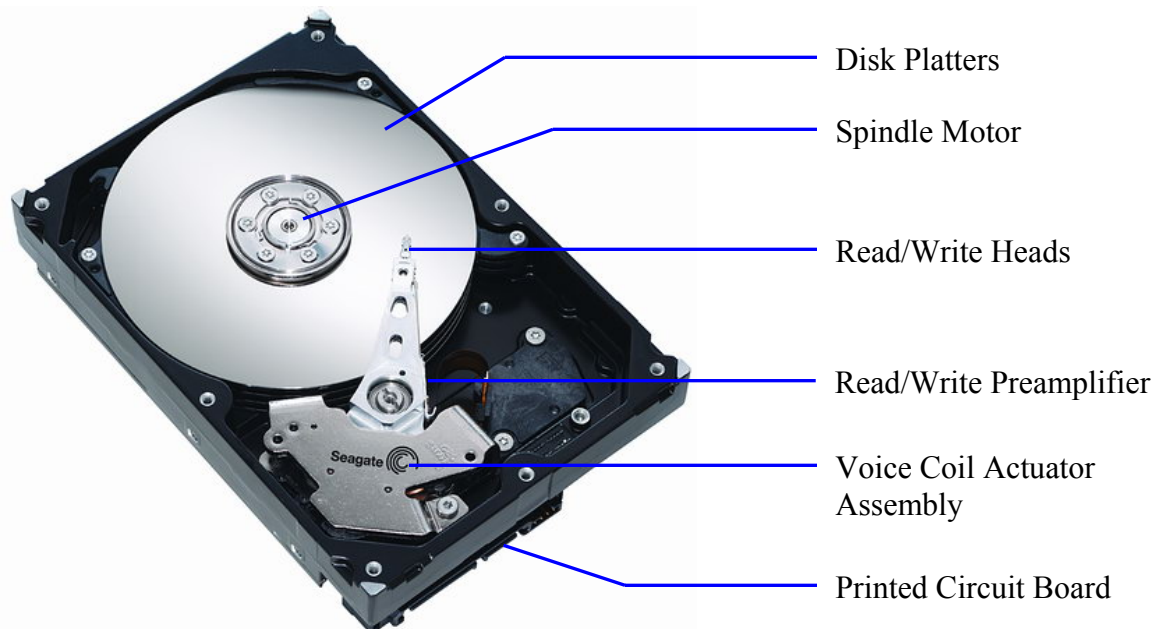
Figure 1.4: Annotated illustration of a modern HDD, showing major components.

board (PCB). Malfunction in any of these components can result in the failure of a HDD. The traditional method of recovering data from a HDD that suffered a physical failure is to replace the damaged part with a functional one from a new HDD of the same model (donor drive) in order to get the HDD functioning again. Techniques such as PCB swapping, head stacks transplant and re-mounting the disk platters onto the spindle of a donor HDD can all be described as part replacement.

The techniques of part replacement were once quite useful in some cases of physical failures. However, there are still many cases in which the data cannot be recovered with the traditional techniques. For example, if the physical damage happens to the medium itself, the data in the damaged region or even all of the data on the disk will become inaccessible. The damage to the medium is usually due to head crashing onto the disk, thus causing the medium to be scratched. Replacing the damaged heads cannot solve the problem because the new heads will crash again when they pass the scratched tracks.
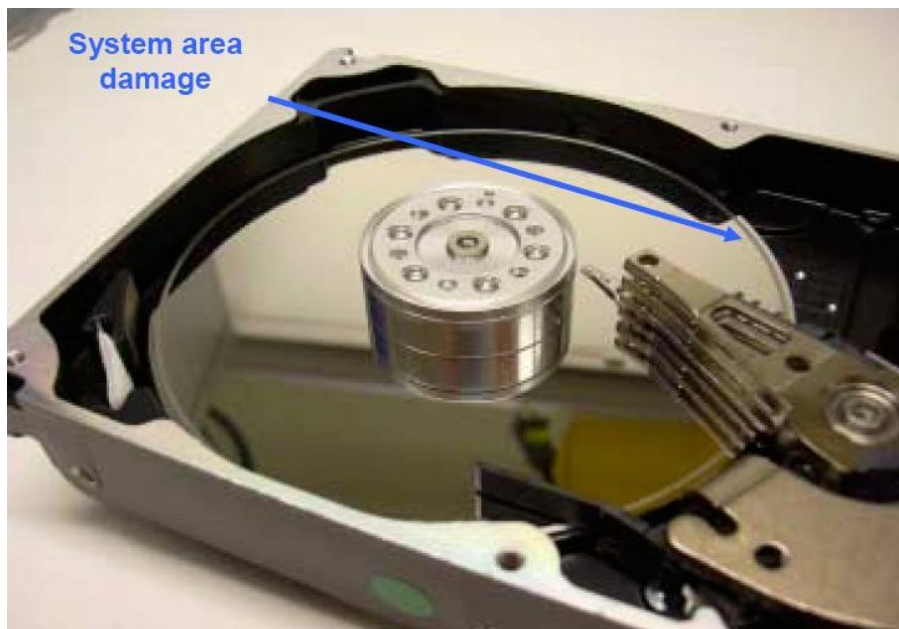
Figure 1.5: Illustration of system area damage due to head crash (from ActionFront).

If there is a scratch at the outer diameter that destroys the system area where the system information of the HDD is stored, the drive can no longer be booted although all the user data is still on the disks (see Fig. 1.5 [43]). Therefore, damage to part of the medium can cause all of the data on the disk to be lost.

Additionally, the superparamagnetic effect can also physically damage the magnetization in the medium, hence resulting in bad sectors and causing data loss. Figure 1.6 shows the readback signal and the spin-stand microscopy of a hard disk with bad sectors. As seen in the top plot of Fig. 1.6, the strength of the readback signal of a bad sector is smaller than that of a normal sector. From the spin-stand image in the bottom plot of Fig. 1.6, one can observe that many of the magnetization bits in the middle track
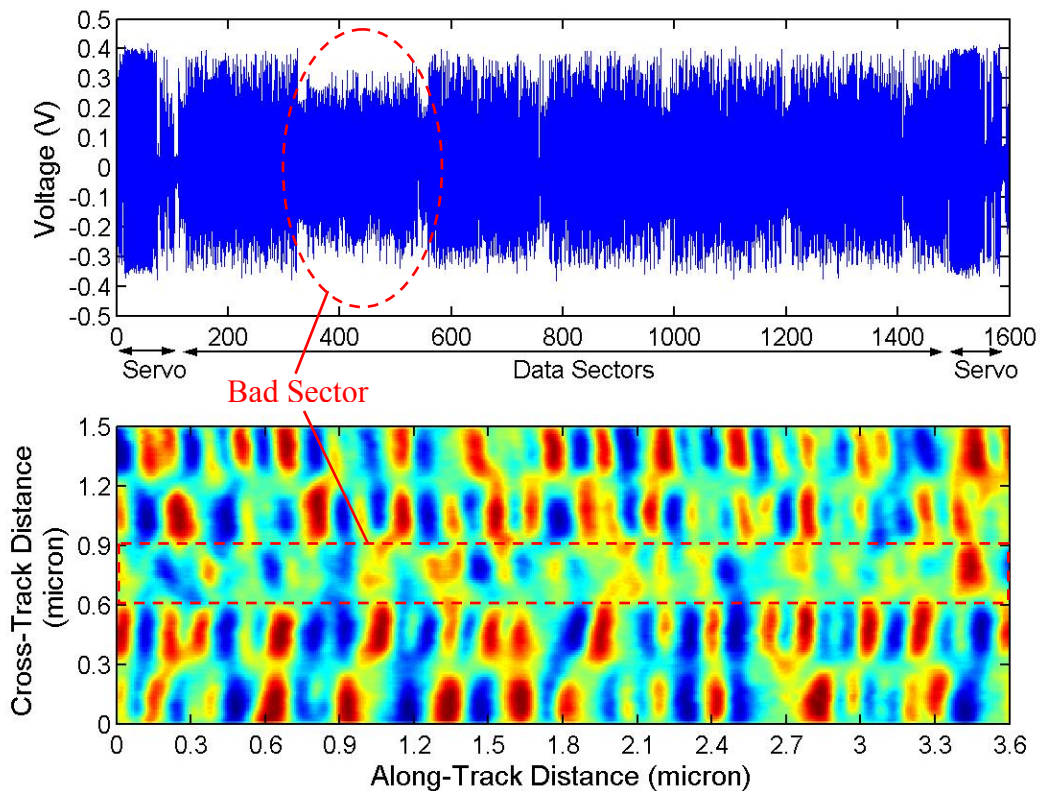
Figure 1.6: Demonstration of a bad sector.

10

are corrupted by superparamagnetism while the magnetization bits in the other four tracks still remain healthy. As a result of the weak signal strength, the data in the bad sector becomes unreadable even if all the components of the HDD are functioning.

Moreover, it has been more and more challenging to perform part replacement on today's HDDs with deep sub-micron track widths. The reason is that it is difficult, if not impossible, to find another geometrically identical mechanical part and precisely install it according to the original orientation. A few microns of difference in dimension and alignment can prevent the new heads or spindle motor donated by a good drive from functioning properly in the failed drive. Even the PCB cannot be replaced by another one of exactly the same model because most of today's HDDs have their own specific parameters, part of which are usually stored in the flash ROM of the PCB. It is clear that there is a need for more advanced data recovery technology to recover hard disk data, which is unrecoverable with the traditional part replacement techniques.

In order to surpass the limitations of part replacement techniques, it is desirable to develop a new data recovery technique that is able to recover the user data without using any hardware from the original drive except the medium itself. Data recovery techniques with this kind of property are defined as drive-independent data recovery. The spin-stand data recovery [44] is the most qualified candidate to perform this task since a spin-stand is purposely designed to simulate an actual HDD. As long as the data is still on the medium, it can be recovered by opening the failed drive, taking out the disk platters, mounting them on the spindle of a spin-stand and using the read head of the spin-stand to access the data. Even the user data in bad sectors can be partially recovered by going through a few appropriate signal processing procedures.

An alternative approach to drive-independent data recovery, called the SignalTrace technology, was also proposed in [45], which can be regarded as the extension of part replacement techniques. Basically, they developed their own electronics to replace the original PCB. With the programming capability of the customized PCB, parts from donor drives can be used to replace the damaged components of the failed drive if all the necessary parameters are set up or tuned properly. Although this approach might be more cost-effective, it is still subject to the restriction of part replacement. First of all, spare parts that are compatible to the original drive must be available for part replacement to be successful. While most failed drives are a few years old, it is not necessarily true that one can always find spare parts for the failed HDD that has been out of production for several years. Furthermore, this approach is not effective when the spindle motor is burned out or the spindle bearings have seized. In those cases, the disk platters must be taken out and mounted on a new spindle motor. When the disk platters are transplanted onto another spindle motor, it usually introduces eccentricity of more than 50 microns, which is far beyond the capability of the servo positioning system of a HDD to compensate. In order to accomplish track following with the existing servo patterns on the medium, the disk platter must be mechanically centered with respect to the rotational center of the new spindle motor so that the amount of repeatable runout (RRO) is within the range of servo positioning. This procedure involves the technique of track centering, which will be presented in Chapter 2. The track-centering technique can be readily applied on the spin-stand. On the contrary, it will be extremely difficult to perform track centering on a HDD. Accordingly, the spin-stand data recovery is more promising to recover the lost data in the worst situation of HDD failure.

1.4 The need for an automatic data acquisition system

We have seen that a spin-stand is a potent tool both for magnetic microscopy and HDD data recovery. However, in order to efficiently obtain the spin-stand images of a hard disk or recover the user data from a failed HDD on a spin-stand, there is a need to develop an automatic data acquisition system so that the processes of these two tasks can be automated. This system will function as an interface between the operator and the spin-stand. By entering the proper parameters into this interface, one can readily acquire the image or the user data of a certain specific region on the hard disk. For example, given the physical address (track ID and sector ID), the system will command the spin-stand to move its read element to the desired location, acquire the readback signal and then return the image or the user data of that sector.

There are a number of technological challenges that must be surmounted in order to build such an automatic data acquisition system. First of all, when a hard disk is removed from its native drive and mounted on a spin-stand, the prewritten tracks on the disk will be eccentric with respect to the reading center of the spin-stand. The repeatable runout (RRO) resulting from this eccentricity can be as large as tens of microns and the read head may cross hundreds of tracks in one revolution of reading. However, piezoelectric actuators presently used in existing spin-stands cannot support such large amplitude of runout. One of the solutions to this issue is to design a customized spin-stand that is capable of varying the radial position of the head substantially to accommodate the magnitude of eccentricity [46]. In a sense, this approach is more straight-forward. On the other hand, it will be very helpful to develop a universal technique for dealing with the issue of eccentricity, which can be applied to every existing spin-stand. This technique

13

must be able to greatly reduce the RRO before the hard disk spins up on a spin-stand so that the remnant RRO is within the range of the head positioning actuators.

Second, it is desirable that the micropositioning system has a high bandwidth response to maintain proper track following of the prewritten data tracks with high frequency irregularities. The micropositioning system of a spin-stand commonly includes a piezoelectric actuator to control the movement of the head and a linear sensor to indicate the position of the head. Due to the slow response of this positioning mechanism and the large mass of the positioning system, the piezoelectric actuator used in a spin-stand cannot compensate for such high frequency variations of the data tracks. Thus, there is a need for a low-mass and high-bandwidth positioning device that can be integrated into an existing spin-stand to considerably improve its positioning capacity. There is also a need to develop an algorithm to generate the control signal to such a positioning device so that the head can precisely follow the irregular data tracks.

Third, in order to acquire the on-track readback signal in real time, not only the large distance of RRO has to be removed but also the small distance of nonrepeatable runout (NRRO) must be compensated. The NRRO of a spin-stand is mainly due to thermal drift effect, which may cause the head to drift toward an adjacent data track. A closed-loop track-following system must be constructed to compensate for the NRRO. This system must be capable of utilizing the existing servo patterns on the disk to generate the position error signal (PES) and compute the control signal for servo control. Furthermore, this system should also allow for real-time track following at a normal spindle rotation speed, such as 7200 RPM for a typical 3.5-inch hard disk, so that the data acquisition rate can be comparable to an actual HDD.

Fourth, a programmable read channel must be developed to interpret the information in the raw readback signals for data recovery purpose. This read channel should provide two functions: data detection and data decoding. The raw readback signals first go through a detection process in order to be converted to actual binary bits. The detected bits then go through several layers of decoding processes for obtaining the decoded bits. This read channel should also be able to make use of the error correction data appended at the end of each data sector to correct any possible error. Since different HDD manufacturers employ different encoding schemes in different drive models, this read channel must offer a number of various options of decoding schemes to allow for performing data recovery on a wide variety of models of HDDs.

Fifth, a typical modern HDD possesses hundreds of millions of data sectors for storing the user data. Each data file occupies multiple data sectors among these hundreds of millions of data sectors. These data sectors may reside on different tracks and surfaces. It is essential to be able to locate all the data sectors where each data file is stored. In order to accomplish this task, we have to study the hard disk geometry and the file systems commonly used by the most popular operating systems. The relation between physical addresses of the data sectors and the logical addresses recognized by the operating system must be established. With the mapping of physical to logical address, the knowledge of the file system and the read channel, we will be able to reach the desired data sectors and obtain the decoded binary data in these sectors. The decoded sectors then need to be assembled in the correct sequences to arrive at complete files. All of these operations must be programmed so that the process of the spin-stand data recovery can be efficiently carried out.

1.5 Main results

We have developed and tested the automatic data acquisition system for spin-stand imaging and drive-independent data recovery. All of the five challenges mentioned in the previous section have been successfully overcome. A track-centering algorithm has been derived to achieve zero eccentricity. This algorithm can be readily implemented on every existing spin-stand without any customized tool or equipment. With this algorithm, we are able to perform whole-track spin-stand imaging of prewritten hard disk data tracks [47]. We also modified the head cartridge of the spin-stand to accommodate external piezoelectric actuators as the micro-positioning device for the track-following purpose. Two different controlling schemes have been investigated to enable accurate track following. The first scheme utilizes the whole-track spin-stand images to extract the desired trajectory and constructs an open-loop track-following system [48]. The second scheme makes use of the existing servo patterns on the disk to generate a feedback signal and form a closed-loop control system. The track-following system based on the first scheme can handle a larger amount of track irregularity but cannot deal with NRRO. On the other hand, the track-following system based on the second scheme compensates both RRO and NRRO but has a smaller range of distance for track following due to the nature of servo positioning. With the track-centering algorithm and the track-following systems, we have been able to efficiently image prewritten data tracks with extremely high track density. With the automatic data acquisition system, experiments on spin-stand data recovery have also been demonstrated to prove the practicality of recovering HDD data on a spin-stand [44]. Figure 1.7 is a picture of the Guzik 1701-MP spin-stand [49] with which all the experiments in this dissertation were performed.
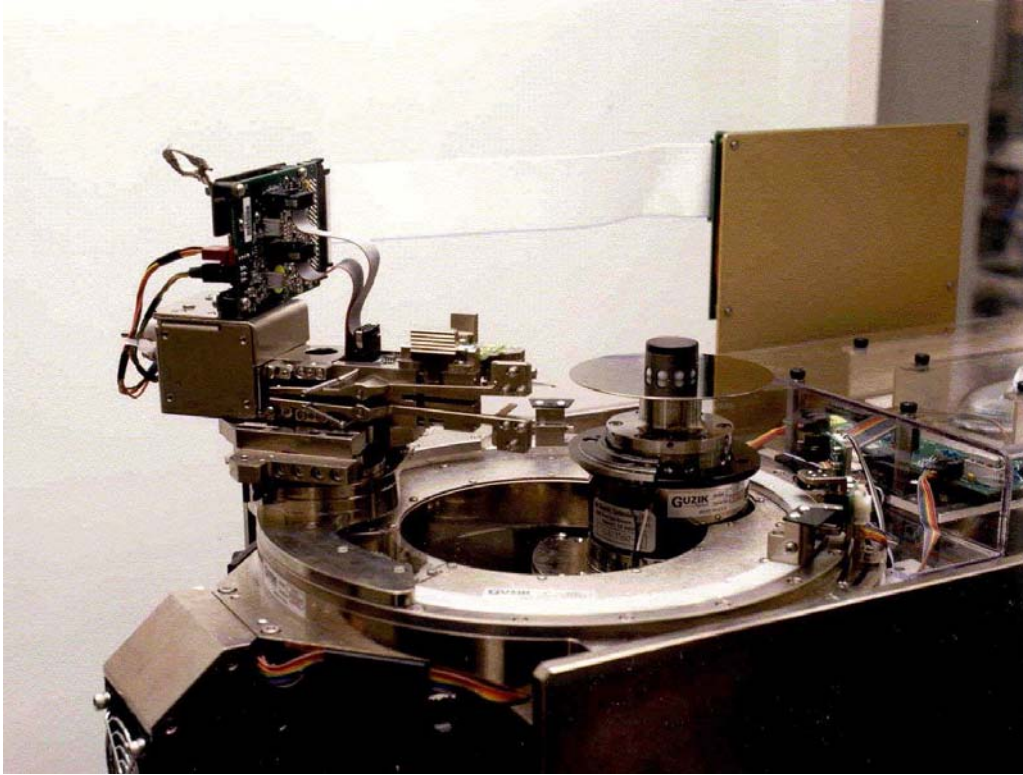
Figure 1.7: Guzik 1701-MP spin-stand.

1.6 Dissertation outline

In Chapter 2, the issue of eccentricity is thoroughly discussed. It is shown that the curves of the data tracks are sinusoidally modulated due to the existence of eccentricity. The track-centering algorithm for removing the eccentricity is developed and presented in detail. We then apply the technique of track centering to achieve zero eccentricity and obtain the demodulated whole-track images of two commercial hard disks with different track densities.

An open-loop track-following technique is proposed in Chapter 3. This technique makes use of piezoelectric actuators to dynamically control the radial displacement of the read head and utilizes the whole-track spin-stand images to extract the desired trajectory.

Controlling algorithms based on the Preisach model of hysteresis are devised to compensate for the hysteretic effects of the piezoelectric actuators. Techniques for extracting the trajectories of irregular data tracks and special methods of selecting the initial phase of these tracks and locking the phase thereafter are also developed. Experiment results of following prewritten data tracks with track pitch of as small as 0.28 μm are presented.

Chapter 4 focuses on making use of the existing servo patterns on the disk for servo control. Two different types of servo schemes are discussed in detail. Algorithms of generating position error signal for both of the two servo schemes are investigated in depth. A servo positioning system operated by a personal computer is constructed to enable closed-loop feedback control of the piezo-driven head. This PC-based servo positioning system is tested with a commercial hard disk whose average track pitch is 1.22 μm.

In Chapter 5, the PC-based servo positioning system is implemented for the purpose of real-time track following. The trajectory of the irregular data tracks is acquired by interpreting the servo data of each servo sector in one revolution of reading. It is shown that the hysteresis of the piezoelectric actuators can be compensated by a few iterations of the servo control loop without actually measuring the hysteresis response of the piezoelectric actuators. The accuracy of the track-following technique based on servo feedback is demonstrated by performing track following on prewritten data tracks with an average track pitch of 0.21 μm.

Chapter 6 presents the spin-stand images of commercial hard disks with areal densities of as high as 131.5 Gbits/in^2. Pronounced distortions due to the effect of

intersymbol interference are observed in the images of the user data regions. The spin-stand imaging technique is also further extended to image hard disk data written on perpendicular media.

Chapter 7 describes in detail the procedures of recovering HDD data on a spin-stand. The hard disk geometry is thoroughly studied. The FAT file system is analyzed. Several layers of HDD data encoding processes are also investigated. Experiments on spin-stand based drive independent data recovery are demonstrated and the results are presented.

Finally, the conclusions and the future directions are presented in Chapter 8.

Chapter 2

Track-Centering Technique

As explained in Chapter 1, the hard disk tracks become eccentric when the hard disk is removed from its native drive and mounted on a spin-stand. The spin-stand based magnetic microscopy technique has been used to image small portions of hard disk sectors [39]. However, in order to acquire the whole-track image of the data tracks, there is a need to have an algorithm that can be used to efficiently center the hard disk so that the center of the hard disk tracks coincides with the rotational center of the spin-stand spindle. These whole-track images are useful for diagnostics of hard disk data and are also important for data recovery purposes.

2.1 The issue of eccentricity

When the target area to be imaged is extended to the entire circumferential track, the

image will be distorted due to track eccentricity. In the presence of eccentricity, instead of obtaining straight lines of data tracks, the trajectories of the tracks will be sinusoidally modulated in the cross-track direction. Eccentricity results from the geometrical difference between the center of the data tracks and the rotational center of the spin-stand spindle. To facilitate the subsequent discussion, several terms are defined as follows. The geometrical center (GC) is the center of the physical disk. The writing center (WC) is the center of the data tracks that have been written on the hard disk. The reading center (RC) is defined as the rotational center of the spin-stand spindle. It should be noted that the GC is different from the WC, and they usually do not coincide with each other. In other words, the distance between the RC and the WC indicates the amount of eccentricity. A geometrical drawing of an off-centered disk on a spin-stand is shown in Fig. 2.1.
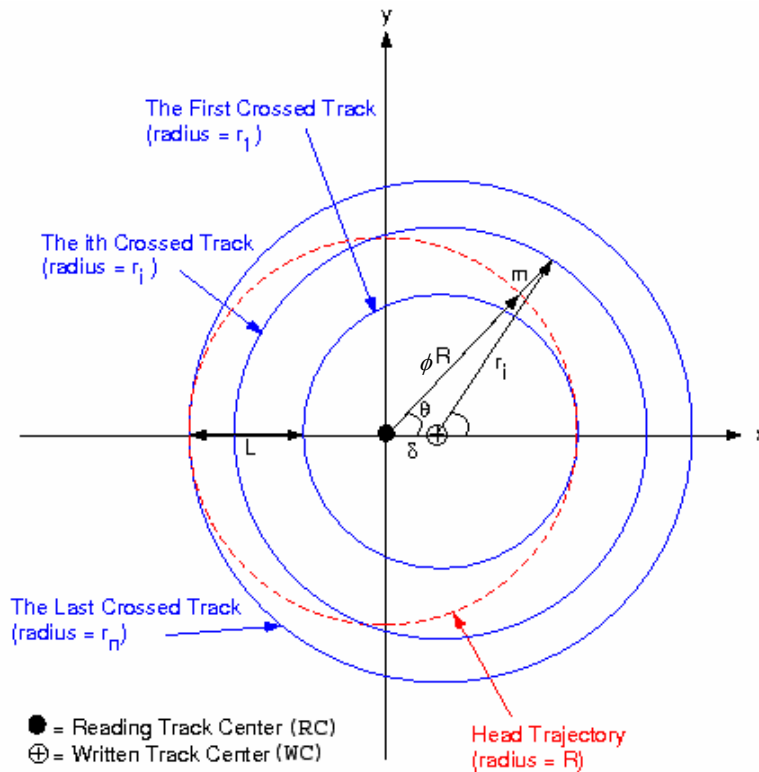
Figure 2.1: The geometry of an off-centered disk.

In Fig. 2.1, The RC is chosen to be the origin of the x-y coordinate system and the WC is on the X axis. In this figure, δ is the distance between the RC and the WC; R is the radius of the circular trajectory of the read head; r_1 is the radius of the first track being crossed; r_i is the radius of the ith track being crossed; r_n is the radius of the nth track being crossed (i.e., the last crossed track); L is the difference between r_1 and r_n. The total number of tracks being crossed is equal to the product of L and the track density (TD). It is easy to observe that L is twice the length of δ. Thus, L can be expressed as:

$$L = r_n - r_1 = 2\delta. \tag{2.1}$$

The total number of tracks being crossed can also be expressed as:

$$n = L \cdot \text{TD} = 2\delta \cdot \text{TD}. \tag{2.2}$$

From Eq. (2.2), it is apparent that the total number of tracks being crossed is only the function of the two parameters, δ and TD, and is independent of the radius of the read head trajectory.

In Fig. 2.1, m is equal to the radial difference between the ith track being crossed and the read head trajectory in the reference of the read center. Assuming that the read head trajectory and the trajectories of the data tracks are all perfectly circular and taking into account that δ is much less than r_i, it can be easily shown that $m(\theta)$ is simply a sinusoidal function with an amplitude of δ. The proof is stated as follows:

$$(R + m)^2 = \delta^2 + r_i^2 + 2r_i\delta\cos\phi. \tag{2.3}$$

Since $\delta \ll r_i$, ϕ is approximately equal to θ. Therefore, Eq. (2.3) can also be written as:

$$R + m \approx \sqrt{r_i^2 + 2r_i\delta\cos\theta} = r_i\left(1 + \frac{2\delta}{r_i}\cos\theta\right)^{\frac{1}{2}}. \tag{2.4}$$

By only keeping the first two terms of Taylor expansions of the second multiplier of the most right-hand side of Eq. (2.4) and rearranging, $m(\theta)$ has the following expression:

$$m(\theta) \approx r_i - R + \delta \cos \theta . \qquad (2.5)$$

In other words, the trajectories of the data tracks in the whole-track image will be modulated as a function of a sinusoid in the cross-track direction with a peak-to-peak amplitude of 2δ.

2.2 The track-centering algorithm

The goal of track centering is to micro-position the disk so that the WC of the disk coincides with the RC of the spin-stand. This is different from "disk-centering" where the goal is to match the GC with the RC. In order to micro-position the disk, a coarse positioning and a fine positioning process are involved. The coarse positioning is accomplished by using a dial-gauge whose resolution is 50 micro inches (about 1.27 μm). The fine positioning is achieved by systematically adjusting the pressure of the set screws that mount the disk onto the spindle. By studying the horizontal component of the pressure exerted by these set screws on the disk, the movement of the disk can be controlled well below 1 μm.

The central issue of track-centering is to know the direction and the distance to move the disk. The geometric relation between the RC and WC of an off-centered disk on a spin-stand is shown in Fig. 2.2, where the RC is chosen to be the origin of the x-y coordinate system. The initial coordinate of the WC is (x_w, y_w), and the distance between the RC and the WC is δ_0. If the coordinate of the WC is known, the difference between the RC and the WC can be reduced to zero by displacing the disk toward the negative
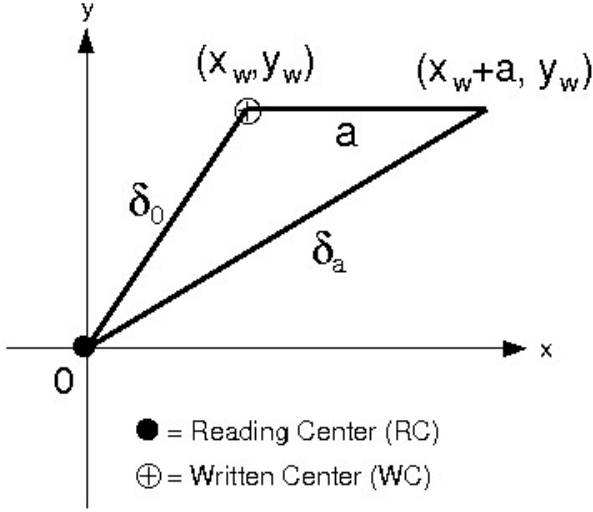
Figure 2.2: The geometry explaining the movement of an off-centered disk.

x-direction with a distance of x_w and then displacing it toward the negative y-direction with a distance of y_w. In order to find out the initial coordinate of the WC (x_w, y_w), we will first move the disk toward the positive x-direction with a distance of a, resulting in a new coordinate of WC at (x_w+a, y_w). Now, the new distance between the RC and the WC becomes δ_a. From Fig. 2.2, we have the following relations:

$$\delta_0 = \sqrt{x_w^2 + y_w^2}. \tag{2.6}$$

$$\delta_a = \sqrt{(x_w + a)^2 + y_w^2}. \tag{2.7}$$

By solving Eq. (2.6) and Eq. (2.7) for (x_w, y_w), we obtain:

$$x_w = \frac{\delta_a^2 - \delta_0^2 - a^2}{2a}; \quad y_w = \pm \frac{\sqrt{4a^2\delta_0^2 - \left(\delta_a^2 - \delta_0^2 - a^2\right)^2}}{2a}. \tag{2.8}$$

Since δ_0 and δ_a can be calculated from the whole-track images and a is also known, x_w and y_w can be determined by using Eq. (2.8). If y_w is positive, the gap between the RC and the WC can be made zero by moving the disk toward the negative x-direction with a

distance of $x_w + a$ and then moving it toward the negative y-direction with a distance of y_w. However, if the eccentricity still remains, it means that y_w is actually negative. In this situation, we can achieve zero eccentricity by simply moving the disk toward the positive y-direction with a distance of $2y_w$.

2.3 Experiment and results

By applying the spin-stand imaging and the track-centering techniques, we have been able to acquire the whole-track images of two hard disks from commercial hard disk drives whose average track pitches are 1.22 μm and 0.43 μm, respectively. Figure 2.3, 2.4 and 2.5 shows the images of the hard disk with track pitch of 1.22 μm, and Fig. 2.6 and
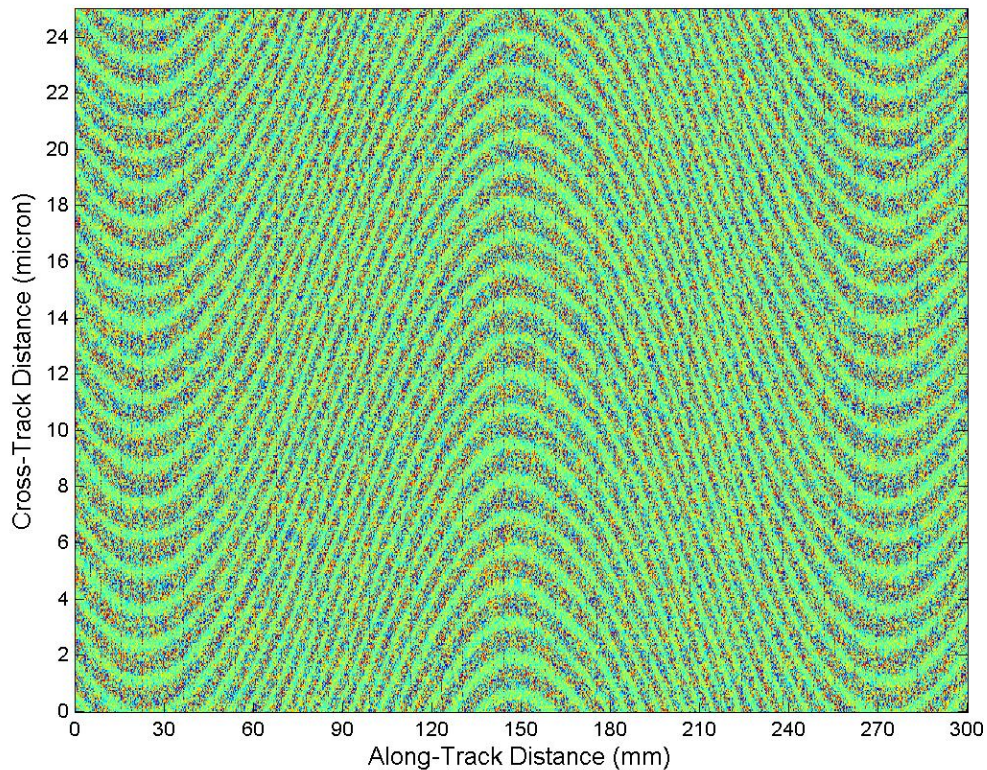
Figure 2.3: Spin-stand image of whole-track hard disk data before track centering.

2.7 shows the images of the other hard disk with track pitch of 0.43 μm. All the images of hard disks were captured by using a Guzik 1701 MP spin-stand.

In Fig. 2.3, 2.4 and 2.5, one full track spans from around 25 mm to 275 mm in the along-track direction. The range of the target area in the cross-track direction is 25 μm. As shown in Fig. 2.3, the curves of the data tracks are sinusoidally modulated in the cross-track direction before track-centering was applied. The peak-to-peak amplitude of those curves, which is equal to 2δ, is calculated from the image to be about 22 μm. In other words, the distance between the RC and WC is about 11 μm. There are 17 tracks being crossed while the read head scans in the along-track direction. Figure 2.4 shows the image of the same disk after the tracks have been properly centered.
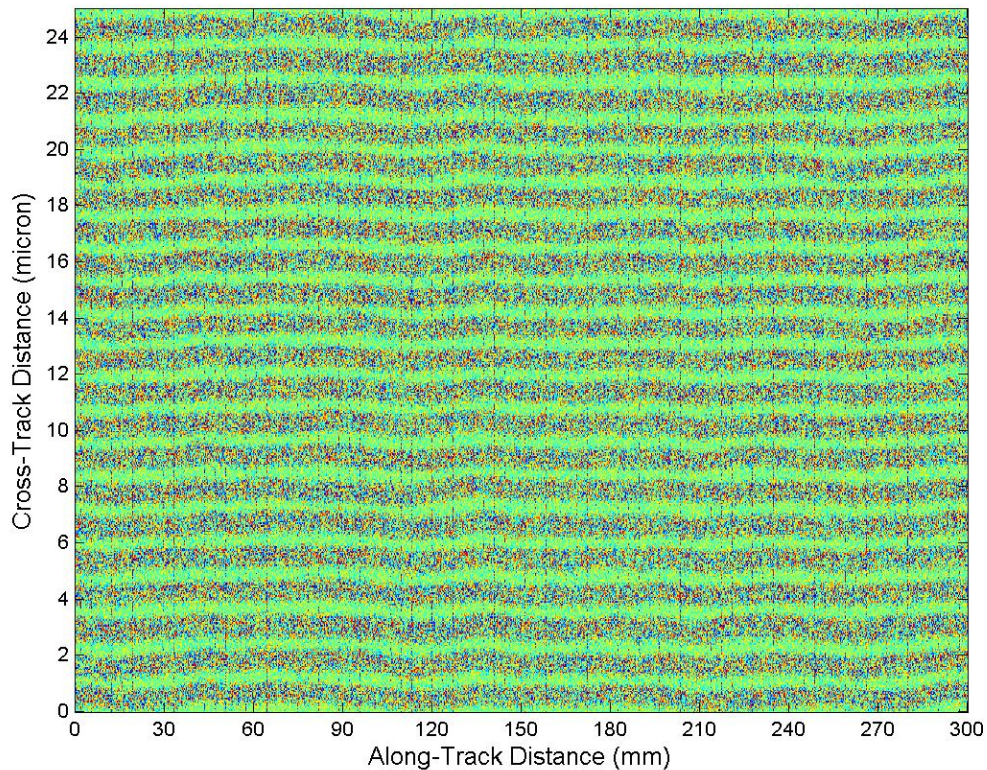
Figure 2.4: Spin-stand image of whole-track hard disk data after track centering.
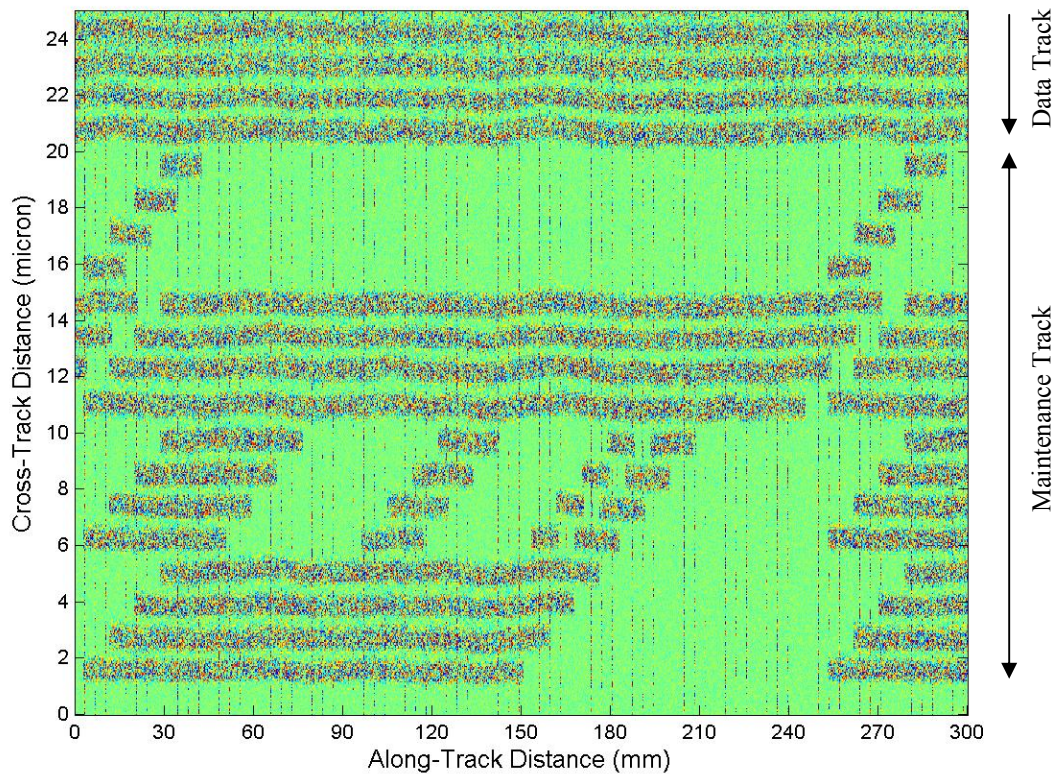
Figure 2.5: Spin -stand image of whole-track hard disk data showing system area.

It should be noted that there is still some variation in the cross-track direction because the written tracks are not perfectly circular. However, compared to the track pitch of this hard disk, the amount of the residual modulation is small enough to allow the analysis of the hard disk data and the servo writing. Different data regions along the tracks can be readily extracted from these whole-track images. With the appropriate read channel, user data can be recovered from the waveforms of the user data sectors.

Figure 2.5 shows the system area of the same hard disk where the firmware information (such as channel and controller parameters) is stored. In the figure, there are 20 tracks, including 16 maintenance tracks and 4 user data tracks. No data exists below the maintenance tracks.
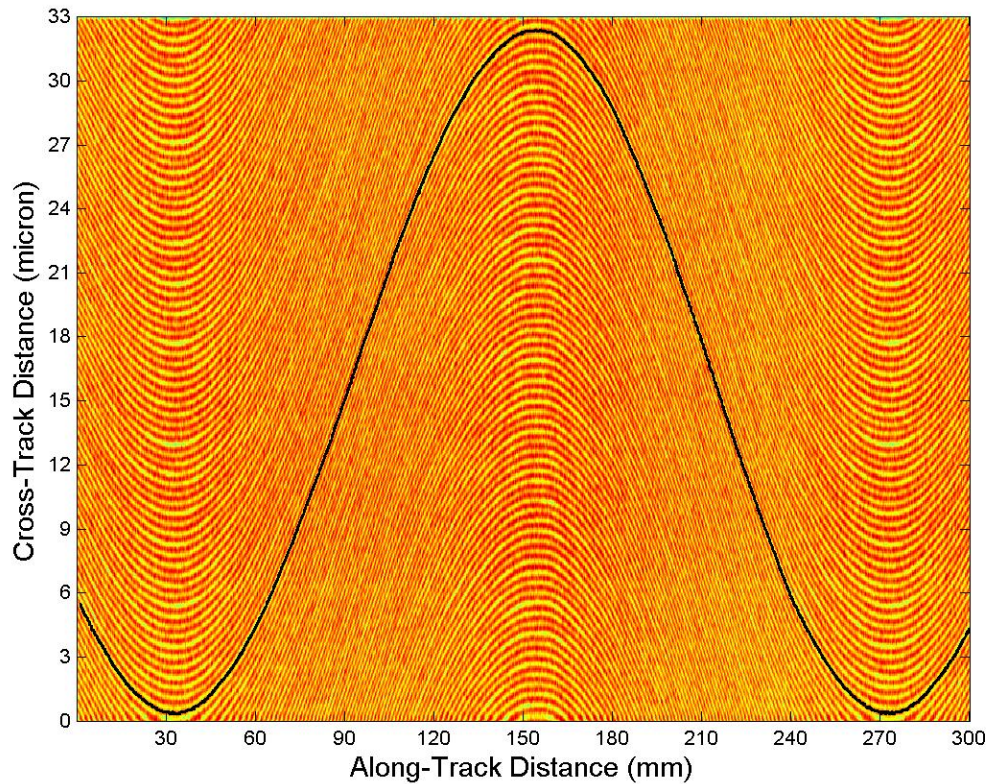
Figure 2.6: Spin-stand image of whole-track hard disk data before track centering.

While Fig. 2.3, 2.4 and 2.5 presents the raw images of the hard disk, the images in Fig 2.6 and 2.7 were processed in order to enhance the contrast of the image. Figure 2.6 shows the whole-track images before track-centering was applied. One of the data tracks is highlighted with a black curve. The peak-to-peak amplitude of the modulated track is calculated from the image to be about 32 μm. There are 77 tracks being crossed while the read head scanned in the along-track direction. Figure 2.7 shows the whole-track image of the disk after the tracks have been properly centered. The amount of residual modulation is as large as the track pitch of this hard disk. Therefore, the irregularity of the data tracks becomes very obvious in this image. It is apparent that the read head was not able to stay on one data track while it scanned in the along-track direction.

Accordingly, having only the track-centering algorithm might not be adequate for compensating the RRO while the track pitch becomes very small.
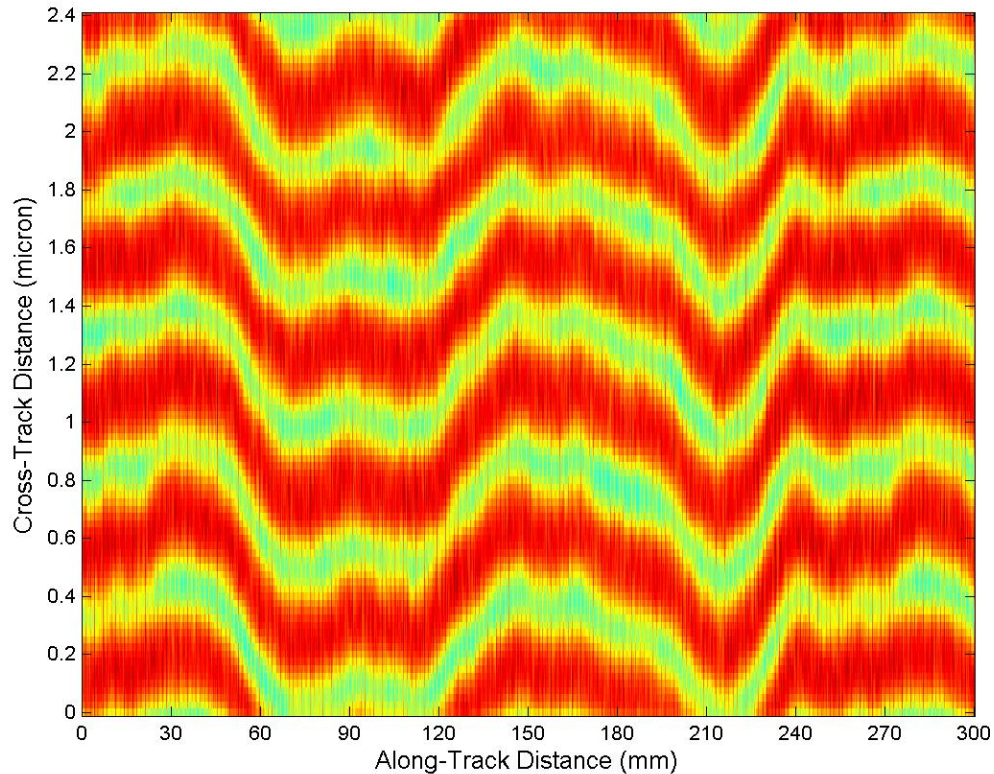
Figure 2.7: Spin-stand image of whole-track hard disk data after track centering.

2.4 Summary

The track-centering algorithm can be used to efficiently and dramatically reduce the repeatable runout due to eccentricity. However, for modern hard disks with track pitch narrower than one micron, another technique is needed to further compensate the RRO due to track irregularity so that the read head can stay on one track and will not cross adjacent tracks. The technique of dynamic track-following has been developed and is presented in the next chapter.

Chapter 3

Dynamic Track-Following Technique

The approach to deal with eccentricity in the previous chapter is to mechanically move the disk so that the center of the data tracks coincides with the rotational center of the spin-stand spindle. The read head is basically static while it scans in the along-track direction. In this chapter, a dynamic approach is presented. The read head is driven by a small piezoelectric transducer (PZT), which is attached to a modified head cartridge on the spin-stand. The displacement of the head in the cross-track direction can be controlled by applying a voltage signal to the PZT. With a proper controlling signal to the PZT, the read head is able to dynamically follow the sinusoidally modulated data tracks. In order to use a PZT for dynamic track following, three issues need to be addressed. First, the trajectories of the modulated data tracks need to be extracted. Second, since input voltage versus displacement characteristics of PZT exhibits hysteresis, the required input signal

to the PZT should be different from the otherwise applied signal had there been no hysteretic effects. Therefore, an algorithm has to be developed to generate modified input signals to the PZT that account for hysteresis. Third, the input signal to the PZT is required to be injected at the appropriate initial phase and the phase needs to be locked thereafter.

3.1 Algorithm for extracting the trajectory of the data tracks

Although the trajectory of the data tracks is theoretically close to sinusoidal, it is actually not an ideal sinusoid. In order to accurately follow the tracks, the actual trajectory has to be extracted rather than implicitly treated as a sinusoid. The algorithm for extraction of the actual track trajectory is illustrated in Fig. 3.1.

The first step is to obtain the raw image of the entire hard disk tracks through spin-stand imaging [Fig. 3.1(a)]. It is evident that the read head senses a stronger signal at the center of the data tracks than at the off-track regions. To ensure that the signal amplitude of the on-track data is made significantly stronger than that of the off-track region, the track image is enhanced by a two-dimensional averaging filter with a constant averaging kernel. Furthermore, a one-dimensional low-pass filter is applied to smooth the image in the along-track direction. The enhanced track image is shown in Fig. 3.1(b). An algorithm based on "region growing" was developed to locate the points with the maximum signal value within the track region in the radial direction. As explained by Gonzalez [50], "Region growing is a procedure that groups pixels or subregions into
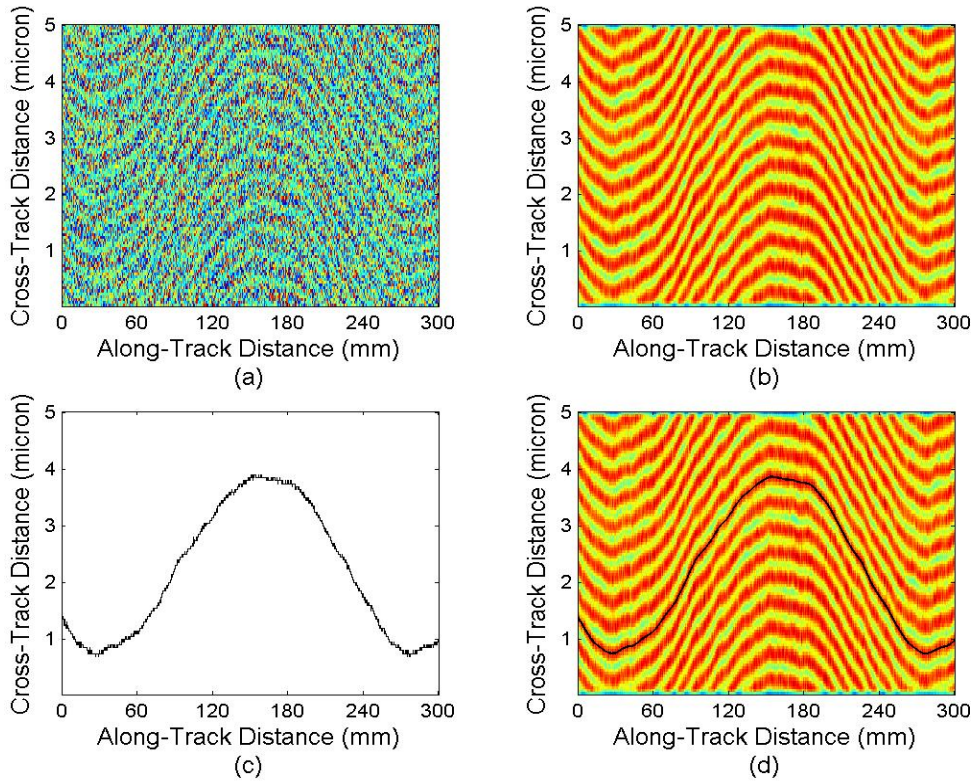
Figure 3.1: Algorithm for extraction of track trajectory.

larger regions based on predefined criteria. The basic approach is to start with a set of

seed points and from these grows regions by appending to each seed those neighboring

pixels that have properties similar to the seed." In other words, a point on one track is

chosen as the starting point (seed), and from that point the whole trajectory is "grown".

Assuming that a point X_0 at the center of one track is chosen, the next point can be found

by evaluating the signal magnitude of the $2q+1$ points, $X_0 + Vi$, where Vi can be written

as follows:

$$V_i = [p, q_i], q_i = -q, -q+1, \ldots, q. \tag{3.1}$$

The parameters, p and q, are positive integers, where p is the stepsize in the along-track

direction and $2q$ is equal to the width of the data track. At each step, the next point with

local maximum signal value is located by using the current point as the reference point. By recording all of the points being passed, the raw trajectory of the data track is extracted, as shown in Fig. 3.1(c).

The raw trajectory is then smoothened by employing another one-dimensional low-pass filter. As shown in Fig. 3.1(d), the extracted trajectory is overplotted on the enhanced image of the hard disk tracks. The accuracy of the trajectory can be improved by extracting the trajectories of ten or more adjacent data tracks and taking an average. The goal of the dynamic track-following is to make the trajectory the read head traverses coincide with the extracted trajectory of the data tracks.

3.2 The dynamics of the piezo-based positioning system

In order to control the displacement of the read head in the cross-track direction, the head cartridge of the spin-stand was modified so that a small PZT can be put next to the head assembly, where the read head is attached. Figure 3.2 depicts the design of the modified head cartridge.
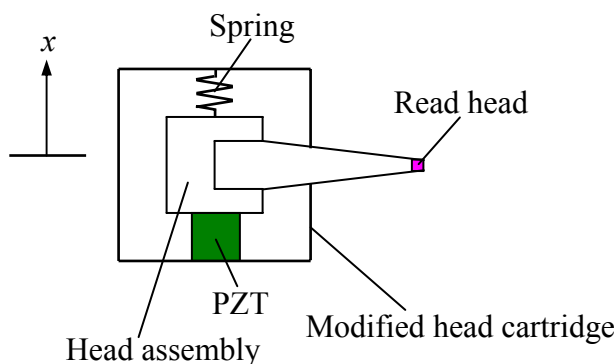
Figure 3.2: Design of the modified head cartridge.

When a positive voltage signal is applied to the PZT, the length of the PZT will increase in the x direction, which is parallel to the cross-track direction. It is clear that the head assembly will be displaced in the positive x direction according to the increased amount of the PZT length. After the voltage signal to the PZT is turned off, the PZT will return to its original size and the head assembly will be pushed back to its original position by the spring. Since the read head is attached to the head assembly rigidly, it has the same motion as the head assembly. As the PZT is subjected to a harmonic voltage signal, the read head will also have a harmonic motion in the cross-track direction.

If a harmonic force $F(t) = F_0 \sin \omega t$ acts on the head assembly, the equation of motion is given by

$$m \ddot{x} + kx \pm \mu N = F(t) = F_0 \sin \omega t , \tag{3.2}$$

where m is the mass of the head assembly, k is the spring constant, μ is the coefficient of friction, and N is the normal force. The sign of the friction force ($\mu N = \mu mg$) is positive (negative) when the head assembly moves in the positive (negative) x direction. The steady-state response is given by

$$x_p(t) = X \sin (\omega t - \phi) \tag{3.3}$$

where the solutions of the amplitude X and the phase angle ϕ can be found in Ref. [51] as shown in Eq. (3.4) and (3.5). Equation (3.4) suggests that friction serves to limit the amplitude of forced vibration for $\omega/\omega_n \neq 1$. However, at resonance ($\omega/\omega_n = 1$), the amplitude becomes infinite. Equation (3.5) indicates that the phase angle is a function of μN (friction force) and F_0 (amplitude of the force acting on the head assembly) and is independent of ω and ω_n.

$$X = \frac{F_0}{k} \left[\frac{1 - \left(\frac{4\mu N}{\pi F_0} \right)^2}{\left(1 - \frac{\omega^2}{\omega^2_n} \right)^2} \right]^{1/2} \quad , \quad \omega_n = \sqrt{\frac{k}{m}} \tag{3.4}$$

$$\phi = \tan^{-1} \left[\frac{\frac{4\mu N}{\pi F_0}}{\left\{ 1 - \left(\frac{4\mu N}{\pi F_0} \right)^2 \right\}^{1/2}} \right]. \tag{3.5}$$

3.3 Measurement of the hysteresis loop

Since the force acting on the head assembly cannot be measured directly, the input to the system is the voltage signal to the PZT rather than the force between the PZT and the head assembly. The response of the system is observed with the following procedures. First, a blank disk is put on the spin-stand and a track is written on the disk while the PZT is subjected to a voltage signal $V(t) = V_0 \sin \omega t$. Second, this track written by the spin-stand is imaged as shown in Fig. 3.3(a). The image is enhanced so that the on-track region is red in color, off-track region is green and other regions are all blue. Finally, the trajectory of this track is extracted by the trajectory extraction algorithm, which has been presented above. The trajectory, which is overplotted on the image in Fig. 3.3(a), indicates the motion of the read head in the cross-track direction.

The hysteresis loop is obtained by plotting the displacement of the read head versus the input voltage signal to the PZT, as shown in Fig. 3.3(b). It should be noted that the hysteretic effect depicted by Fig. 3.3(b) is not only due to the PZT itself, but also entangling with the dynamics of the system studied in the previous section. In other

words, some of the hysteretic effect is due to the phase angle ϕ in Eq. (3.3). However, it is difficult to obtain the exact phase angle ϕ from experiment since a sophisticated laser interferometer might be needed to measure the dynamic motion of the PZT directly.
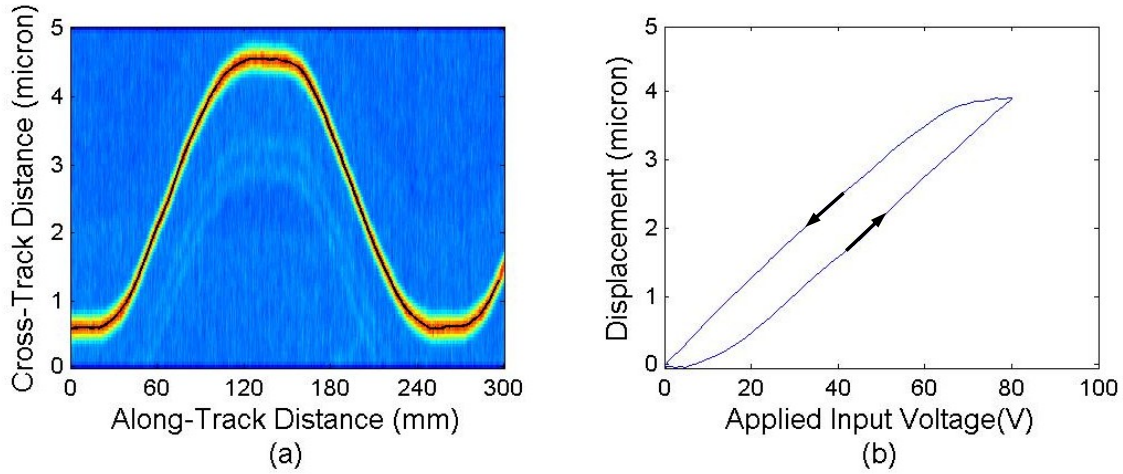
Figure 3.3: Measurement of the hysteresis loop.

3.4 Algorithm for controlling a piezoelectric transducer

The two prevalent ways for controlling the PZT are the voltage control method and the current control method. The voltage control method is stable and has a high degree and ease of controllability. However, the hysteretic effects between the applied voltage and the PZT's displacement are quite pronounced. On the other hand, the current control method can achieve a nearly linear relation between the current through the PZT and the corresponding displacement. Nevertheless, there is still some residual hysteresis which may not be negligible. In addition, the amplitude of the current applied to the PZT is only a few milliampere and such a small current requires additional and more elaborate equipment for control realization. For these reasons, the voltage control method has been used in our work.

By switching the vertical and horizontal axis of Fig. 3.3(b), a relation of the voltage signal applied to the PZT versus the displacement of the read head is obtained and shown in Fig. 3.4(a).
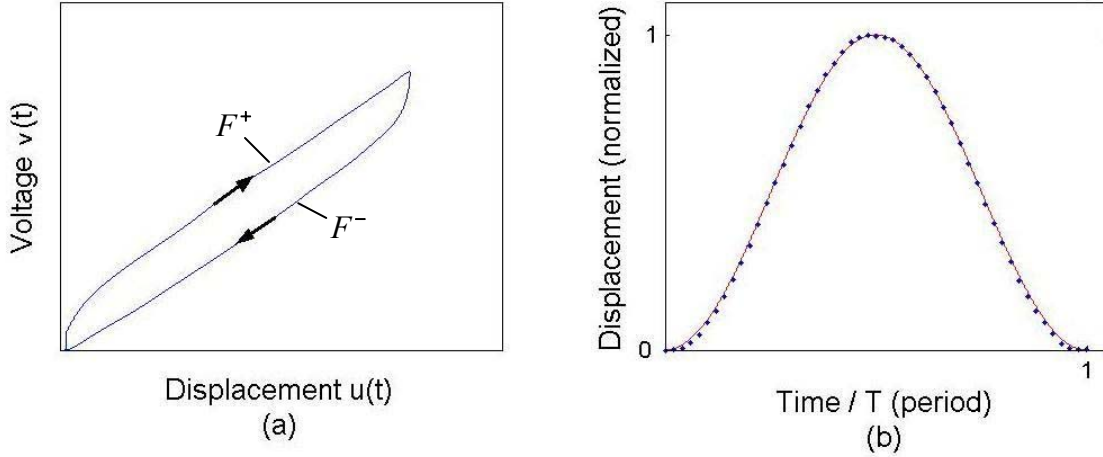
Figure 3.4: (a) Hysteresis loop. (b) Function of ideal sinusoid (solid line) and the trajectory of the PZT-driven head (dots).

The hysteretic effect has been represented by the Preisach model [52]-[53], which can be written as follows:

$$v(t) = \iint \mu(\alpha,\beta) \hat{\gamma}_{\alpha\beta} u(t) d\alpha d\beta, \qquad (3.6)$$

where $v(t)$ is the voltage applied to the PZT, $\mu(\alpha,\beta)$ is the weight function that can be fully characterized by using "first-order reversal curves," $\hat{\gamma}_{\alpha\beta}$ are rectangular loop operators with α and β as "up" and "down" switching thresholds, respectively, and $u(t)$ is the input (desired) displacement. In the particular case when a track trajectory consists of two monotonic sections, the equation for controlling the voltage signal can be simplified and represented as

$$v(t) = F^{\pm}[u(t)], \qquad (3.7)$$

where $v(t) = F^+[u(t)]$ when the read head displacement corresponds to the ascending branch and $v(t) = F^-[u(t)]$ when the read head displacement follows the descending branch of the hysteresis loop [Fig. 3.4(a)]. The input signal to the PZT can be readily obtained through Eq. (3.7). For example, if the trajectory to follow is a sinusoidal function, $u(t)$ can be expressed as

$$u(t) = \delta[\sin(\omega t - 0.5\pi) + 1], \text{ where } 0 \le \omega t < 2\pi \tag{3.8}$$

The applied signal to the PZT that will achieve a sinusoidal motion is given by

$$v(t) = F^+\{\delta[\sin(\omega t - 0.5\pi) + 1]\} \text{ when } 0 \le \omega t < \pi \tag{3.9}$$

and

$$v(t) = F^-\{\delta[\sin(\omega t - 0.5\pi) + 1]\} \text{ when } \pi \le \omega t < 2\pi. \tag{3.10}$$

The accuracy of the voltage control of the PZT and its immunity to hysteretic effects are demonstrated in Fig. 3.4(b). The solid line is a function of ideal sinusoid. The dots represent the trajectory of the properly controlled PZT-driven head. The difference between the desired trajectory (solid line) and the actual trajectory (dots) is less than ± 50nm.

3.5 Setup of dynamic track-following and phase-locking system

The setup of the dynamic track-following system consists mainly of a spin-stand (Guzik 1701MP) and its read-write analyzer (RWA). The rest of the track-following system consists of a high sampling rate digitizer card (Acqiris DP210) for signal capturing, a personal computer (PC) for performing extraction of track trajectories and

for implementing the algorithm of hysteresis compensation, a waveform generator for generating the desired input signal to the PZT, and a signal amplifier for amplifying the PZT input signal. The spin-stand head cartridge that houses the GMR head has been modified to make it compatible with a PZT as the micropositioning device. Figure 3.5 shows the block diagram of the experimental setup.
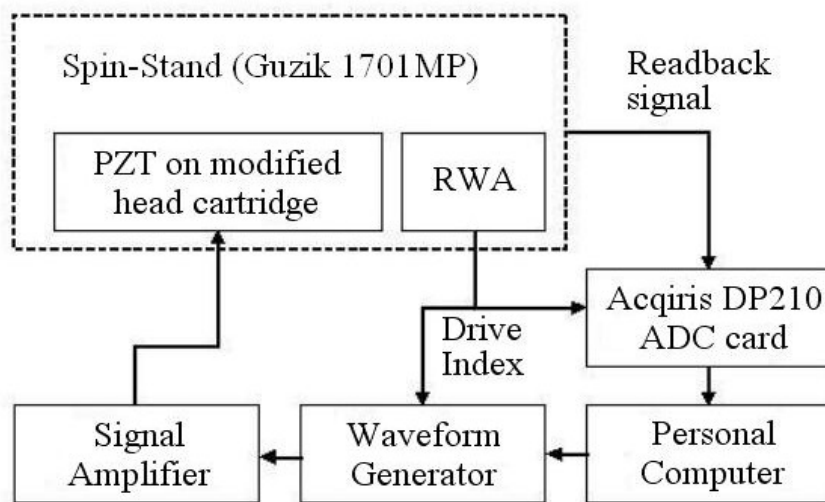
Figure 3.5: Block diagram of track-following setup.

Before the signal from the output of the waveform generator is sent to the amplifier, a phase-locking system is activated to locate the initial phase of the input signal to the PZT and lock the phase thereafter. As shown in Fig. 3.5, both the waveform generator and the digitizer card are triggered by the same drive index of the spin-stand spindle, which is generated for every complete spindle revolution. From the captured track image, the initial phase is determined as the time offset between the first data point of the image and the data point corresponding to the first trough. Although the phase is already locked by the triggering, this phase is adjustable by introducing a time delay between the drive index and the outputting timing of the waveform generator. By using the phase-locking

39

system, the driving signal of the PZT and the off-centered trajectory are kept in phase. This driving signal is then amplified and sent to the PZT, which is attached to the modified head cartridge of the spin-stand.

3.6 Experiments and results

In the experiments, the imaged hard disk drives have average track pitches of 0.43 μm and 0.28 μm, respectively. A GMR head with a read width of 0.15 μm was used as the reading element. A commercially available piezoelectric stack transducer (NEC model #AE0203D08) with a length of 10 mm was used for the purpose of dynamic track-following. The recommended driving voltage to this PZT is between zero and 100 volts, which corresponds to a displacement range of approximately 5 μm. After the hard disk was removed from its native drive and mounted on the spin-stand, the hard disk was preliminarily centered by using the track-centering technique so that the repeatable runout was less than 5 μm.

The top and bottom plots of Fig. 3.6 show the whole-track images of a hard disk, whose track pitch is 0.43 μm, without and with dynamic track following, respectively. In the top plot of Fig. 3.6, it can be seen that seven hard disk tracks were being crossed before the dynamic track-following technique was applied. The peak-to-peak amplitude of those curves is calculated from the image to be about 3 μm. The bottom plot of Fig. 3.6 shows the image of the same region after the tracks have been dynamically followed by using the described track-following technique. The amplitude of remnant variations is found from the figure to be about 50 nm. Compared to Fig. 2.7 (the experimental result of applying only the track-centering technique on the same hard disk), the remnant runout
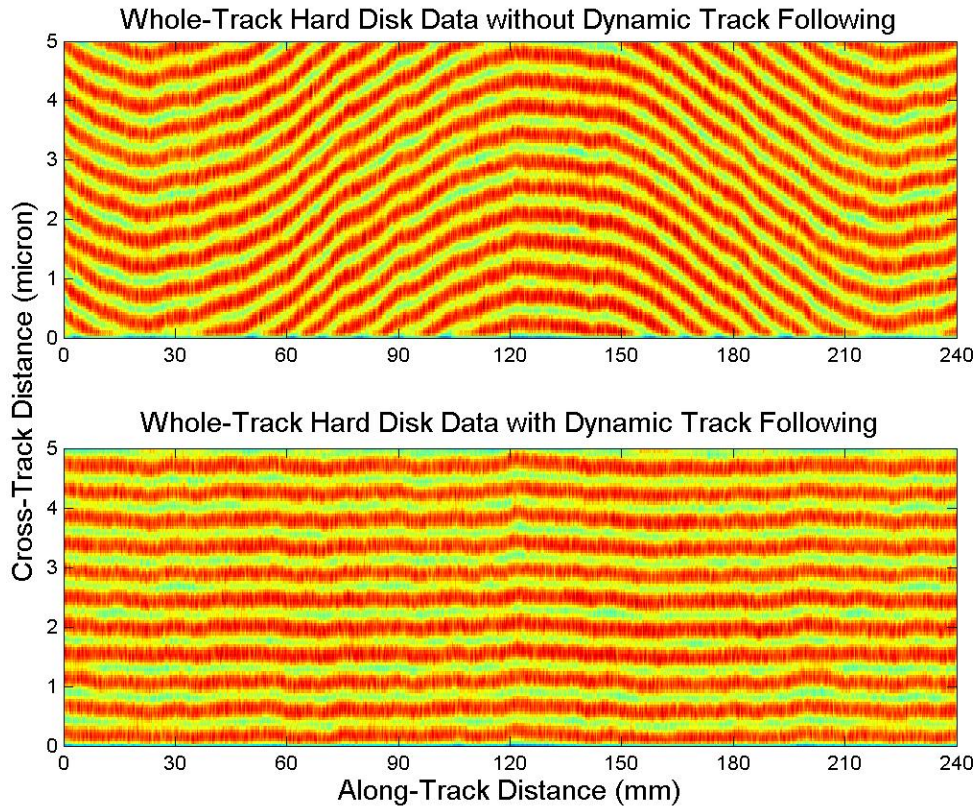
Figure 3.6: Whole-track hard disk data without and with dynamic track following.

has become much smaller in the bottom plot of Fig. 3.6. Here, the read head was able to

stay on one data track while it scanned in the along-track direction.

Figure 3.7 shows the whole-track images of a hard disk with track pitch of 0.28 μm.

As illustrated in the top plot of Fig. 3.7, the read head crossed thirteen tracks due to

eccentricity. The peak-to-peak amplitude of those curves is calculated from the image to

be about 4 μm. The bottom plot of Fig. 3.7 shows the whole-track image of the

dynamically followed data tracks. The amplitude of remnant variations is still about 50

nm, which corresponds to almost 20 percent of the track pitch. This amount of remnant

runout might be adequate for obtaining spin-stand images, but it is still not good enough

for the purpose of data recovery.
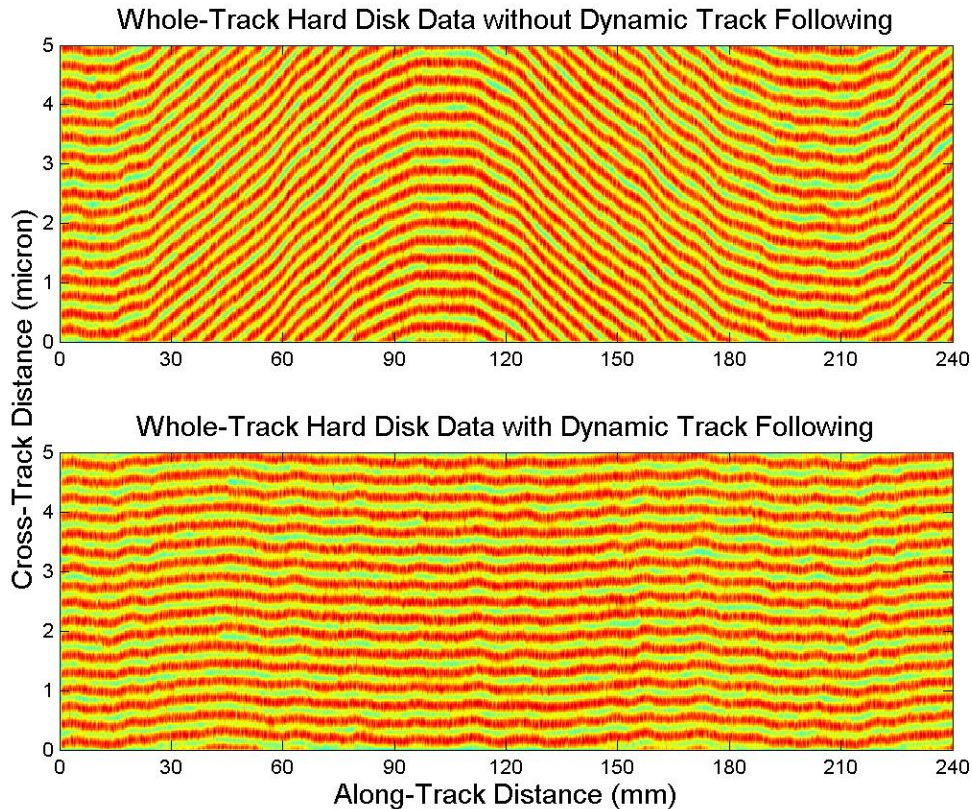
Figure 3.7: Whole-track hard disk data without and with dynamic track following.

3.7 Summary

With the dynamic track-following technique, the repeatable runout is substantially reduced. The read head is now able to dynamically follow a particular track in its entirety without crossing any adjacent tracks. However, in order to further reduce the amplitude of the remnant variation to less than one-tenth of the write track width, it is mandatory that the current open-loop approach of track following be converted into a closed-loop control system, making use of position error signal (PES) that is calculated from the signals generated by the existing servo patterns as a feedback. In chapter 4, the algorithm

for PES signals generation is studied and the experimental results of a PC-based servo control system are demonstrated.

Chapter 4

Servo Positioning System

In order to determine the position of read head, HDD manufactures write servo information on hard disks. The most popular form of servo is the so-called embedded servo, where servo information is interleaved with the data sectors across the entire surface of a hard disk. This servo information, including track identification (ID) and servo bursts, provides the feedback for the servo positioning system of a HDD, which controls the movement of the read/write head with respect to a particular data track. In order to accurately follow the prewritten tracks of a hard disk on a spin-stand, it is desirable to develop a servo positioning system for a spin-stand. Recently, much effort has been made to achieve precise tracking by implementing an external servo system on a spin-stand [54]-[56]. However, the servo feedback signal in their setup is from an external optical sensor. Meanwhile, a servo positioning system based on feedback signal

from the servo bursts written by the spin-stand itself has also been developed [57]-[59], which only allows for following data tracks written after a hard disk is mounted on the spin-stand. In this chapter, we propose a novel mechanism for acquiring the feedback signal from the existing servo bursts prewritten on the hard disk to follow the prewritten data tracks on a spin-stand, but we will first explain the principles of HDD servo systems.

4.1 Position error signal

Servo bursts are written in a special sequence on the disk to form a spatial pattern, encoding displacement of read head from the center of a data track. The servo pattern carrying information about off-track displacement can be decoded to generate the position error signal (PES) [60]. An ideal PES is linearly proportional to the displacement from the center of a data track. Therefore, it is essential to obtain the PES as the feedback for servo positioning systems. In this section, we will study two different types of servo schemes for PES generation.

4.1.1 The 4-burst servo scheme

Figure 4.1 illustrates a servo scheme which is commonly used in modern hard disk drives [61]. It consists of four bursts of single frequency patterns written sequentially in the along-track direction and placed offset with respect to each other in the cross-track direction. The PES is determined by the amplitude difference between servo bursts. If the read head is flying exactly at the center of the track, the amplitudes of burst A and burst B are equal. When the head drifts away from the track center, the amplitude of one burst
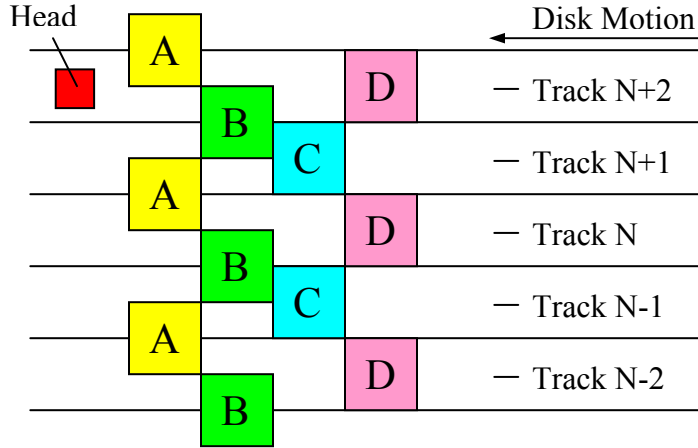
Figure 4.1: Layout of 4-burst servo pattern.

increases as compared to that of the other burst. The difference in amplitude between burst A and burst B is known as in-phase PES, and the difference in amplitude between burst C and burst D is known as quadrature PES. The in-phase and quadrature PES are usually expressed as

$$PES_{ip} = \frac{\overline{A} - \overline{B}}{\overline{A} + \overline{B}} \ \text{ and } \ PES_{qu} = \frac{\overline{C} - \overline{D}}{\overline{C} + \overline{D}} \ , \tag{4.1}$$

where $\overline{A}, \overline{B}, \overline{C}$ and $\overline{D}$ are the amplitudes of each burst.

When the position of the head is close to the center of the track, in-phase PES is linearly proportional to the difference between the head position and the center of the track. However, since the read width of the head is usually narrower than the track width, in-phase PES saturates when the head drifts to the off-track region. Likewise, quadrature PES becomes nonlinear when the read head is near the center of the track. Figure 4.2 shows the relation of magnitudes of in-phase PES and quadrature PES versus the distance in the cross-track direction. It can be seen that the saturation phenomena occur at the edges of the tracks for in-phase PES and at the center of the tracks for the quadrature PES.

46
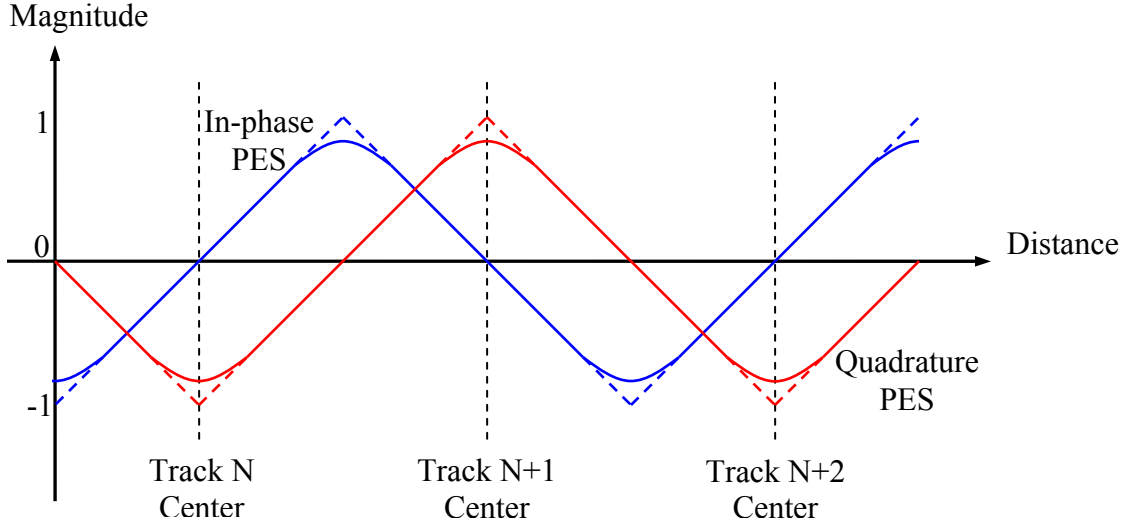
Figure 4.2: Simulated In-phase and quadrature position error signals.

The problem of nonlinearity is overcome by combining the linear region of quadrature PES with that of in-phase PES. It can be seen that the absolute value of in-phase PES is less than that of quadrature PES when the read head is closer to the center of the track than to the edge. Therefore, in-phase PES is used for the position error signal whenever the absolute value of in-phase PES is less than that of quadrature PES. Similarly, quadrature PES is used for the position error signal whenever the absolute value of in-phase PES is larger than that of quadrature PES. In addition, the sign of the position error signal indicates at which side of the track (above the center or below the center) the read head is. The equation for calculating linear PES can be written as follows:

$$
\begin{aligned}
PES &= PES_{ip} & \text{when} \quad & \left|PES_{ip}\right| < \left|PES_{qu}\right| \text{ and } PES_{qu} < 0 \\
PES &= -PES_{ip} & \text{when} \quad & \left|PES_{ip}\right| < \left|PES_{qu}\right| \text{ and } PES_{qu} > 0 \\
PES &= -PES_{qu} - 1 & \text{when} \quad & \left|PES_{ip}\right| \geq \left|PES_{qu}\right|, \ PES_{ip} < 0 \text{ and } PES_{qu} < 0 \\
PES &= -PES_{qu} + 1 & \text{when} \quad & \left|PES_{ip}\right| \geq \left|PES_{qu}\right|, \ PES_{ip} < 0 \text{ and } PES_{qu} \geq 0 \\
PES &= PES_{qu} + 1 & \text{when} \quad & \left|PES_{ip}\right| \geq \left|PES_{qu}\right|, \ PES_{ip} > 0 \text{ and } PES_{qu} < 0 \\
PES &= PES_{qu} - 1 & \text{when} \quad & \left|PES_{ip}\right| \geq \left|PES_{qu}\right|, \ PES_{ip} > 0 \text{ and } PES_{qu} \geq 0
\end{aligned}
\tag{4.2}
$$

47

An ideal PES according Eq. (4.2) is shown in Fig. 4.3. It can be seen that the magnitude of PES is proportional to the distance between the read head and the center of the track. PES is positive when the read head is above the center of the track and is negative when the read head is below the center of the track.
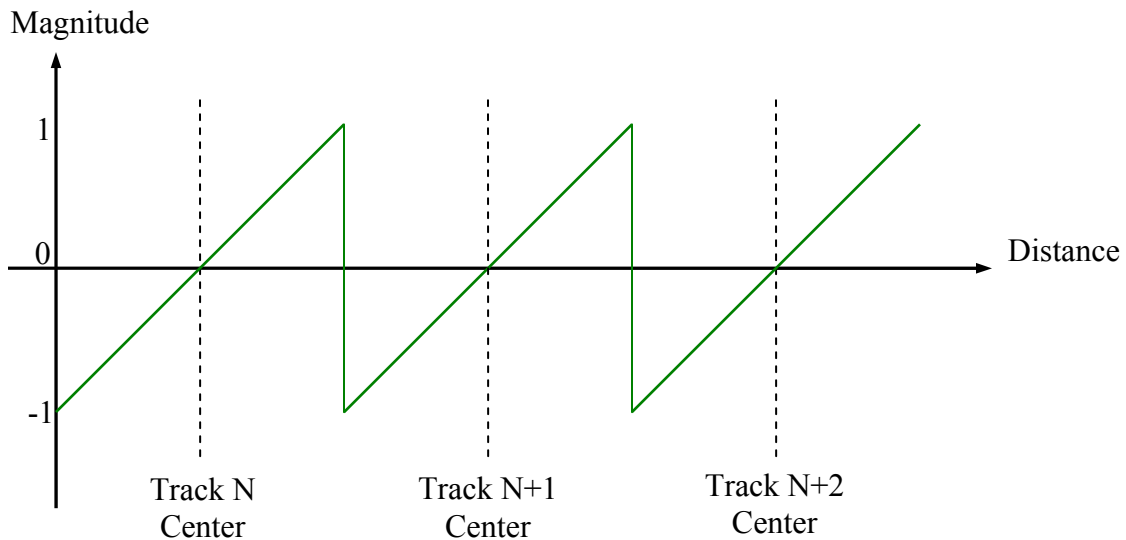
Figure 4.3: Ideal position error signal.

4.1.2 The 2-burst servo scheme

The conventional 4-burst servo scheme has been used in HDDs for more than a decade. However, desperate needs for higher storage capacity have urged HDD designers to continually seek to improve the yield of disk space. Although servo information is crucial for the operation of a HDD, the area of the disk recording surface occupied by the servo bursts cannot be used to store user data. Accordingly, reducing the amount of the area of the disk recording surface occupied by the servo bursts would, in turn, result in more space for storing user data. Recently, a novel servo scheme, comprising only two

servo bursts written in the along-track direction, has been proposed in [62]. In this section, we will study the layout and principles of the 2-burst servo scheme.

Figure 4.4 shows the layout of the 2-burst servo scheme. It can be seen that there are only two servo bursts instead of four servo bursts in the along-track direction. The normal burst field, marked with "N", corresponds to burst A and burst B in the conventional 4-burst servo scheme and the quadrature burst field, marked with "Q", are equivalent to burst C and burst D. The improved servo scheme combines two circumferentially adjacent servo bursts into one single burst by modifying two features of the original scheme. First, the conventional servo scheme has a gap as wide as the track pitch between each two radially adjacent bursts. Now, this gap becomes only a quarter of the track pitch while the width of the bursts is three quarters of the track pitch. Second, a phase difference of 180 degrees is introduced between each two radially adjacent bursts. In other words, the polarity of burst N_1 is opposite to that of burst N_2. Likewise, the polarity of burst Q_1 is also opposite to that of burst Q_2.
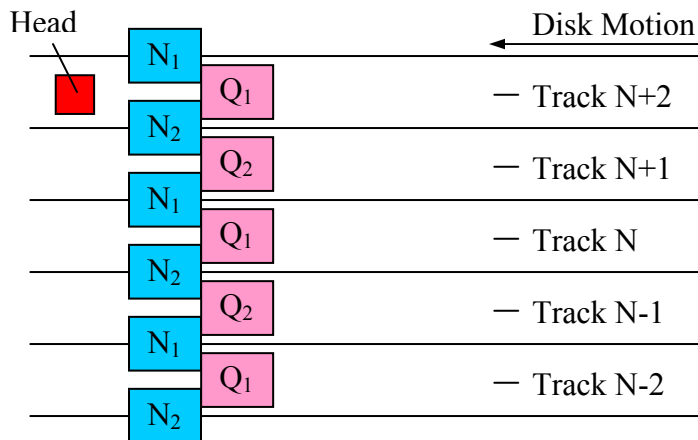
Figure 4.4: Layout of 2-burst servo pattern.

When the read head is flying exactly at the center of the track, cancellation will occur in the normal burst field as the polarities of burst N_1 and burst N_2 are opposite. Therefore, the magnitude of the PES signal generated by the normal burst field (N signal) near track center is small or zero. When the read head drifts away from the track center and gradually moves toward either side of the track, the amplitude of N signal will be larger and larger and will be at its maximum as the read head is exactly at the edges of the tracks. The sign of the signal can be positive or negative, depending on the polarity of the burst toward which the read head drifts. In contrast, Q signal reaches its maximum at the center of each track and becomes small or zero at the edges of the tracks. As a result, N signal can represent the signal generated by burst A and burst B, and Q signal is equal to the signal generated by burst C and burst D in the conventional 4-burst servo scheme.

The in-phase and quadrature PES can be obtained by the following equation:

$$PES_{ip} = \frac{N}{n_0} \text{ and } PES_{qu} = \frac{Q}{n_0} \qquad (4.3)$$

where N and Q are the magnitudes of N signal and Q signal and n_0 is the normalized factor. Although Eq. (4.3) is much simpler than Eq. (4.1), the results of these two equations are the same. In addition, the relation of in-phase PES and quadrature PES magnitudes versus the radial distance in the 2-burst servo scheme is the same as that of the 4-burst servo scheme and thus can also be illustrated by Fig. 4.2. Therefore, the linear PES for 2-burst servo scheme can also be obtained by using Eq. (4.2) and illustrated by Fig. 4.3. It is shown that the same PES is generated for feedback control while the area of the disk recording surface occupied by the servo bursts in the 2-burst servo scheme is only half of that in the 4-burst servo scheme.

4.2 PES generation algorithm

4.2.1 PES generation algorithm for the 4-burst servo scheme

Figure 4.5 shows the waveform of the readback signal from the servo data region of a hard disk using 4-burst servo scheme, which includes the gain, track ID, servo bursts and part of the user data. The PES generation algorithm is composed of three parts, the triggering scheme, the burst magnitude measurement and the PES calculation. The triggering scheme is used to locate the exact position of the four servo bursts. It utilizes the gain as the trigger pattern and obtains a reference point with respect to the servo bursts. The starting and ending point of each of the four servo bursts can be found by knowing the distance from the reference point to the beginning of the first burst and the length of each burst, which are measured by counting the number of sampled points from
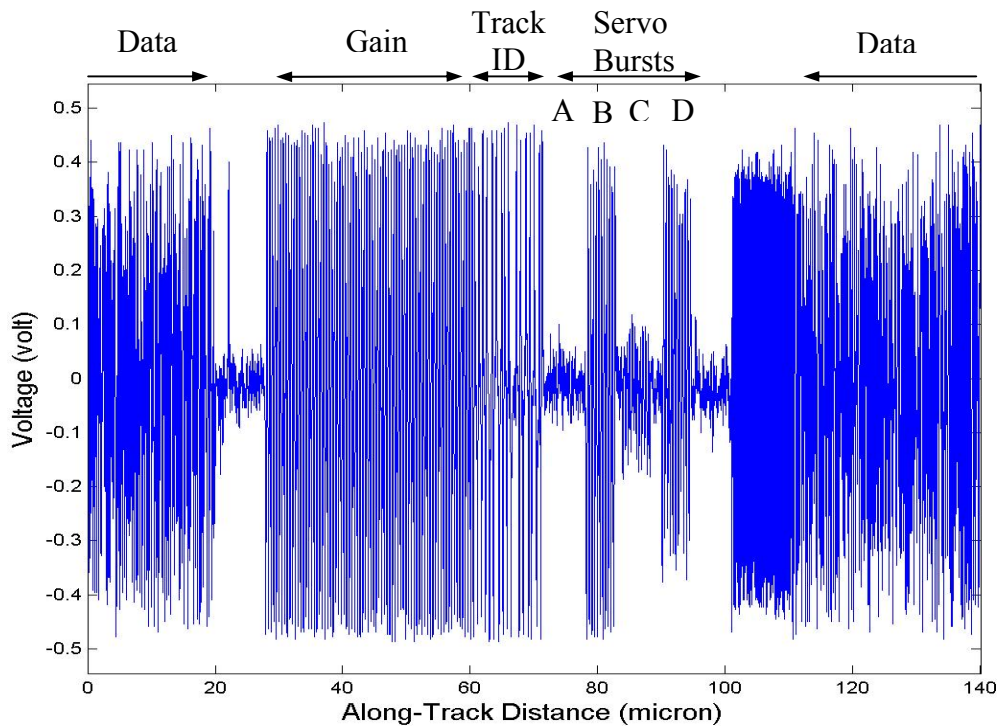
Figure 4.5: Waveform of the readback signal from the servo data region.

Fig. 4.5. The amplitudes of the four servo bursts are obtained by summing the absolute values of all of the sampled points in each burst. Since the sampling rate of the digitizer card can be set high enough to have at least ten samples for each pulse, the summing of sample values is approximately equal to the result of integration. With the amplitudes of the four servo bursts, the PES can be calculated by using Eq. (4.1) and Eq. (4.2).

The algorithm is programmed in C++ and the PES is generated on-the-fly. The relation between PES magnitude and cross-track distance can be obtained by microstepping the head in the cross-track direction. The top plot of Fig. 4.6 shows the in-phase and quadrature PES, and the bottom plot illustrates the linear PES. The experimental data is acquired from a commercial hard disk with track pitch of 2.15 μm.
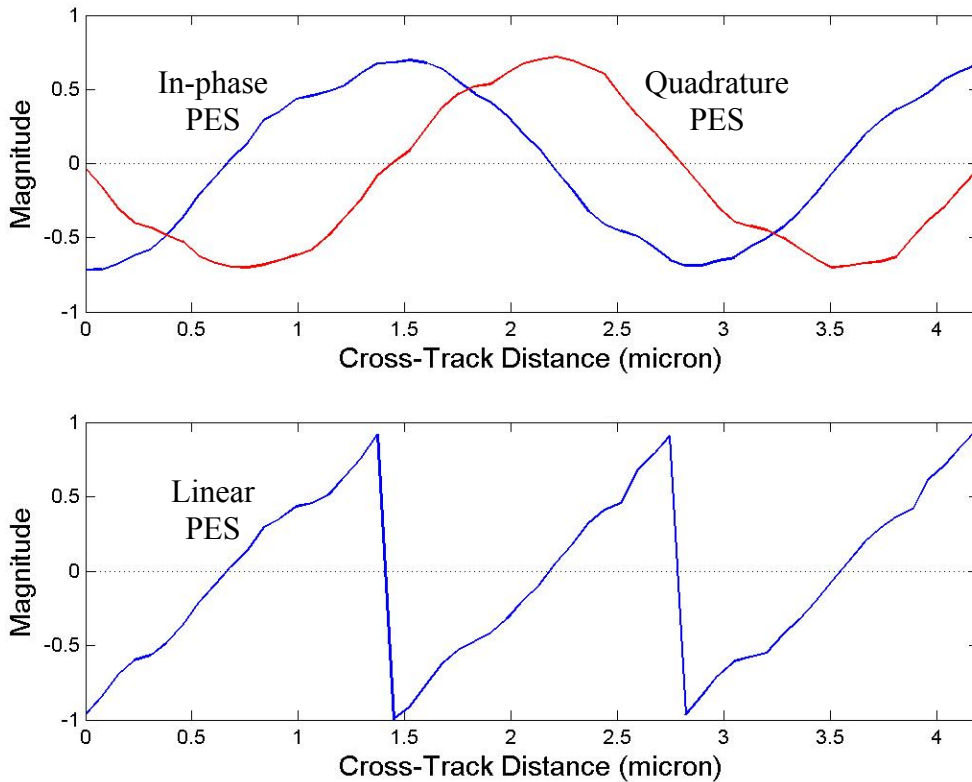
Figure 4.6: Real in-phase PES, quadrature PES and linear PES.

4.2.2 PES generation algorithm for the 2-burst servo scheme

Figure 4.7 shows the waveform of the readback signal from the servo data region of a hard disk using 2-burst servo scheme, where the bottom plot zooms in at the servo burst region. This readback signal is acquired while the read head is at the track center. It can be seen that the signal strength of burst N reaches its minimum and that of burst Q is at its maximum. Here, triggering is achieved by the same triggering scheme as in the 4-burst servo scheme. However, the magnitudes of N signal and Q signal are measured by using the signal values of specific sampled points in the servo bursts instead of by the principle of integration. The triggering scheme gives a reference point with respect to the servo bursts. The distance between the reference point and the first chosen point of the normal burst is constant and so is the distance between the reference point and the first
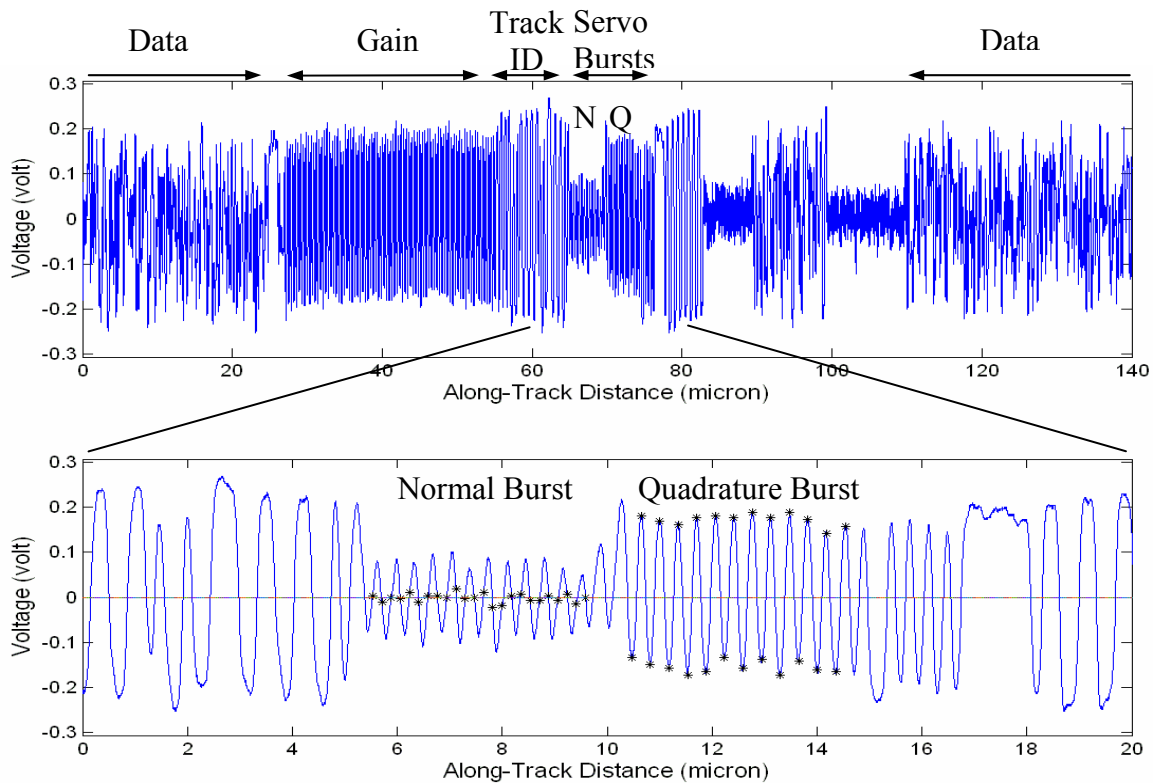
Figure 4.7: Waveform of the readback signal from the servo data region.

chosen point of the quadrature burst. Starting from the first chosen points, we will pick up a number of sampled points from each of the two bursts with a constant offset. These distances and offset are predetermined in terms of number of samples and programmed in the PES generation algorithm. As seen in the bottom plot of Fig. 4.7, we select 24 sampled points, which are marked with stars, from each of the bursts. It should be noted that these chosen points happen to be near the waist of the signal waveform while the burst reaches its minimum and occur at the peaks of the signal waveform while the burst arrives at its maximum. By taking the average signal value of these points (the sign of every other point must be reversed), we obtain the magnitudes of N signal and Q signal. Then the PES, shown in Fig. 4.8, can be calculated by using Eq. (4.2) and Eq. (4.3).
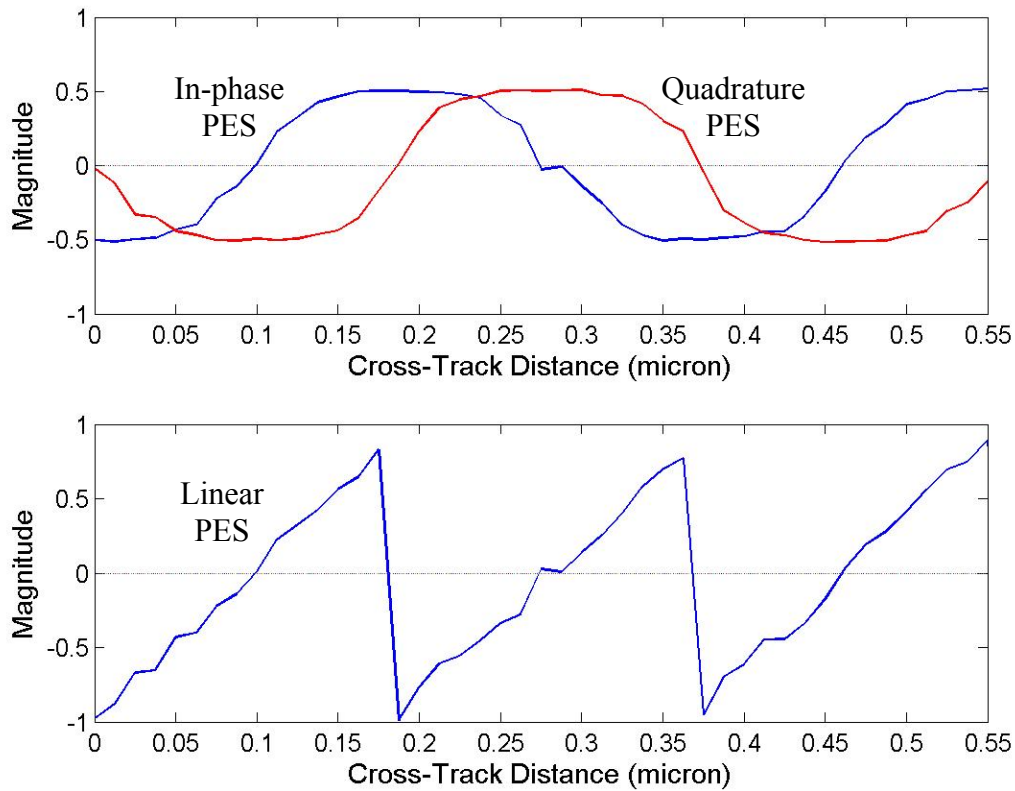
Figure 4.8: Real in-phase PES, quadrature PES and linear PES.

4.3 Setup of the servo positioning system

The experiment setup of servo positioning system is basically very similar to that of the track following system. The only difference is that the waveform generator in Fig. 3.5 is replaced by a multi-function card (NI PCI-6070E) as shown in Fig. 4.9. The PES generation algorithm is performed by personal computer (PC). After the servo data is processed by the PC, a voltage signal proportional to the magnitude of the PES is generated by the multi-function card. This voltage signal is then amplified by the signal amplifier and sent to the PZT as the servo control signal. Although the PES signals are linearly proportional to the distance between the read head and the track center, several iterations might be needed to correct the position of the read head due to the hysteretic effect of the PZT. Since the servo data in one particular servo sector can only be read once per spindle revolution, the time taken in one overall control loop is equal to the period of one spindle revolution.
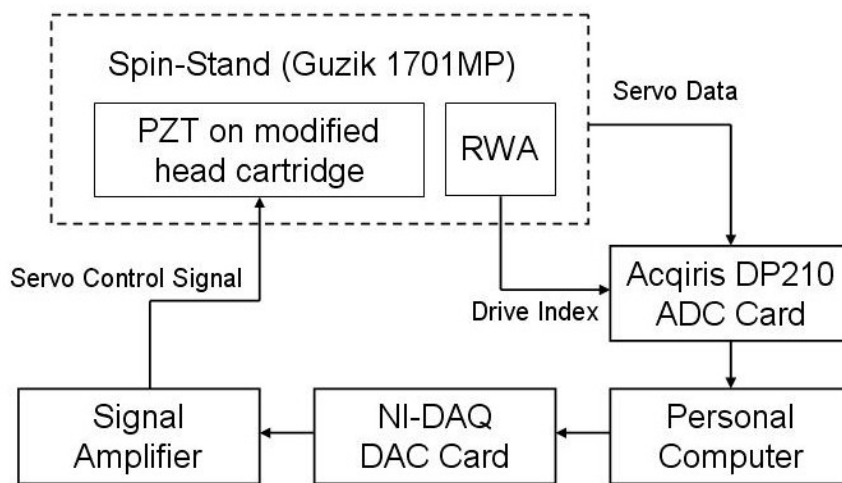
Figure 4.9: Block diagram of servo positioning system setup.

4.4 Mechanism of the servo positioning system

Figure 4.10 illustrates the mechanism of the servo positioning system. The plant is the system to be controlled. The block, A/D, represents the analog-to-digital converter. The true PES $\hat{y}(t)$ is converted to the measured PES $y(k)$ through A/D. $r(k)$ is the reference position. The tracking error $e(k)$ is equal to the difference between $r(k)$ and $y(k)$. The error signal is sent to the integral controller, and the controller computes the integral of this error signal with the following equations.

$$\begin{aligned} u(k) &= K_I a(k) \\ a(k) &= a(k-1) + e(k) \end{aligned}$$, where K_I is the integral gain. (4.4)

The signal $u(k)$ represents samples of the input signal to the plant. The block, D/A and hold, represents the digital-to-analog converter and hold circuit, which holds each sample of $u(k)$ for T seconds to produce an analog controlling signal $\hat{u}(t)$ to the plant. If the spindle of the spin-stand rotates at 5400 revolutions per minute (RPM), T is equal 0.011111 since each revolution takes 11.111 milliseconds. The integral gain K_I depends on the track pitch of the hard disk and the size of the PZT. K_I has to be chosen properly so that the read head will be moved to the center of the track as soon as possible.
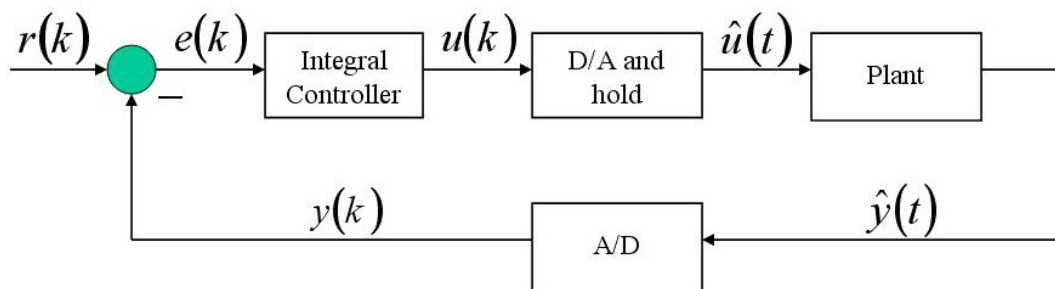
Figure 4.10: Block diagram of the servomechanism.

4.5 Experiments and results

The servo positioning system has been tested with a disk from a commercial hard drive whose average track pitch is 1.22 μm. A GMR head with a read width of 0.39 μm was used as the reading element. A PZT with a length of 5 mm was used for the servo control purpose. The integral gain K_I was set to be 1.0. Figure 4.11 shows the position error signal at one particular sector of a track in time domain. The top plot of Fig. 4.11 indicates that the read head was off-track by 50 to 70 percent of the track width without servo control. The read head moved to the center of the track (within 10 percent of the track width) within four iterations of servo control loop and stably remained at the track center as observed in the bottom plot of Fig. 4.11.
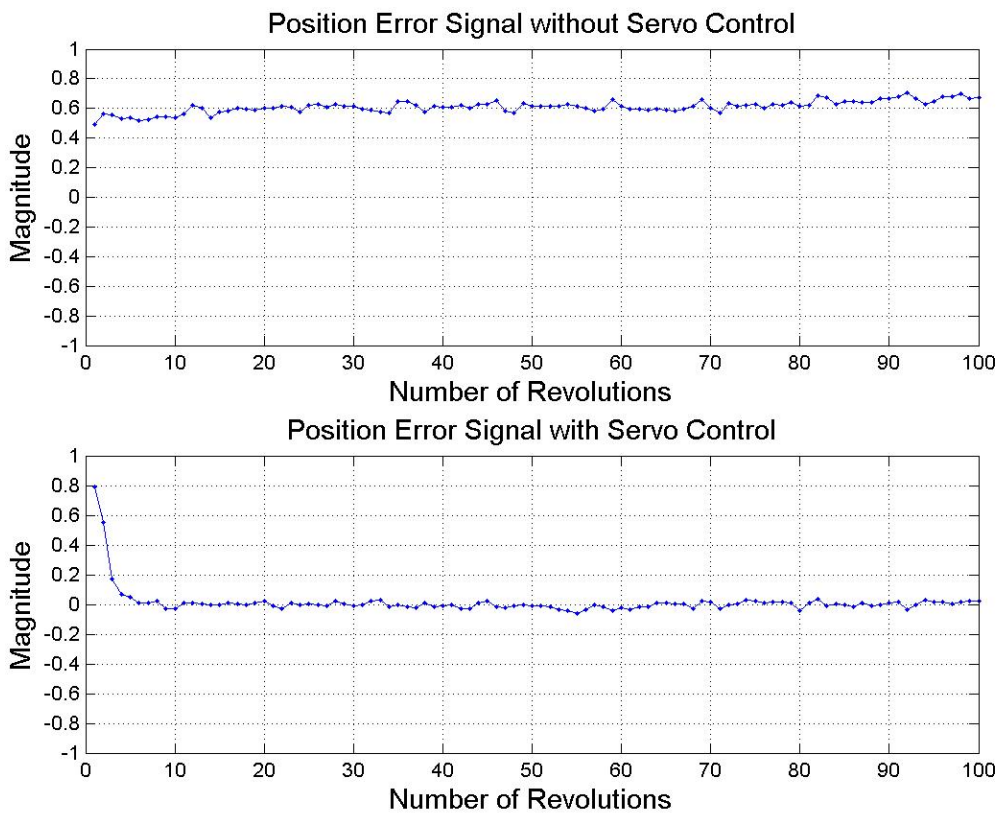
Figure 4.11: Position error signal with and without servo control.

57

4.6 Summary

We have studied the PES generation algorithms both for the 4-burst and 2-burst servo schemes. A servo positioning system based on the feedback from the existing servo patterns on a hard disk has also been developed for a spin-stand. The PES generation algorithms can also be applied to extract the trajectories of data tracks, which is a crucial part of the dynamic track-following technique proposed in Chapter 3. By using the servo information as the control feedback, the track-following system based on the open-loop approach in Chapter 3 can be converted into a closed-loop system. In the next chapter, we propose a novel track-following technique based on servo feedback, which enables real-time track following on a spin-stand with runout less than one-tenth of the track width.

Chapter 5

Track-Following Technique

Based on Servo Feedback

In order to compensate for the runout due to eccentricity, a track-centering algorithm and an open-loop approach of track-following technique have been proposed in Chapter 2 and 3 respectively. However, the ultimate goal is to follow the modulated tracks within one-tenth of the track width. Therefore, it is mandatory to develop a closed-loop control system for real-time track following on a spin-stand. In this chapter, a novel track-following system based on servo feedback is demonstrated.

The feedback for head positioning system is the position error signal (PES) which is calculated from the servo signals generated by the servo patterns. The calculation of the PES is done by a PC. The method of performing control and data acquisition tasks with

INTEL based PCs under Windows NT has been proposed in [63]. PC-based control systems under Windows NT provide the advantages of low cost and high compatibility for different interface devices. Normally, such systems are used in low-end or non-real-time control applications. W. E. Wong etc. first implemented the PC-based control system to upgrade the positioning capacity of an existing spin-stand [57]. However, the update rate of feedback signals has become an issue. They have been struggling for a few years to improve the calculating efficiency of the PES generation algorithm. By the end of 2005, they had successfully accomplished a 15-kHz update rate of feedback control by using a 3 GHz CPU PC [59]. Nevertheless, this update rate is still not fast enough without slowing down the spindle rotational speed. For example, the update rate for a hard disk made in year of 2006, having 270 servo sectors per track, has to be higher than 32.4 kHz if the spindle speed was originally at 7200 RPM in its native drive. Moreover, the response time of the PZT-based head positioning system also must be taken into account. The current design in section 3.2 can only achieve a response time of about 200 microseconds. Even if the update rate is able to be further improved and the dynamic system is re-designed so that the response time is substantially reduced, the nonlinearity of the PZT due to hysteresis still needs to be dealt with.

The technique proposed in this chapter adopts a similar set-up as reported in [57]. The novelty here is that the improved PC-based servo positioning system can achieve real-time track following without slowing down the spindle speed or upgrading CPU speed to improve processing capacity. A special algorithm has been developed to overcome the three issues mentioned above and enables real-time track following of the eccentric data tracks with runout of less than one-tenth of the track pitch.

5.1 Algorithm for real-time track following

In a hard disk drive, one of the main tasks of the head servomechanism is to compensate the nonrepeatable runout (NRRO) due to disk vibration, spindle vibration and spindle bearing runout. In order to keep the head on track constantly, it is mandatory to calibrate the position of the head many times in one spindle rotation. The more servo sectors per track, the more frequently the position of the read head can be calibrated in one revolution. This is one of the reasons why the hard disk drives manufacturers have been increasing the number of servo sectors to improve the positioning capacity. The head positioning system in a hard disk drive has a high servo bandwidth mainly because the PES signals are calculated by the on-board chips and the heads are controlled by voice coil actuators which are operated by using electromagnetic force. However, a PC-based servo control system using a PZT as the positioning device does not provide such a high servo bandwidth. Fortunately, the NRRO of a spin-stand with a high-cost and well-designed spindle motor is much smaller than that of a hard disk drive. The main source of the NRRO of a spin-stand is the thermal drift effect, which makes the head drift in the radial direction by the changes in the temperature of the head assembly. Since the temperature usually changes slowly and contiguously, it allows us to go with another approach of using the existing servo patterns for track following to compensate the NRRO due to the thermal drift effect.

This novel approach is based on the idea of dynamic track-following technique proposed in Chapter 3. Originally, the trajectories of the modulated tracks are acquired from the whole-track spin-stand images, which take hundreds of spindle revolutions to construct. In order to construct a close-loop control system, the existing servo patterns are

used to indicate the relative position between the read head and the data tracks. As a result, the trajectory of the modulated tracks can be acquired in one single spindle revolution. In each iteration of the servo control loop, the control signal to the PZT is updated according to the current trajectory of the data tracks. The PZT nonlinearity can be compensated by a few iterations of the control loop without actually measuring the hysteresis loop. The algorithm for real-time track following is basically composed of two parts. The first part is the algorithm for trajectory extraction and the second part is the iterative compensation for the PZT hysteresis.

5.1.1 Algorithm for acquiring the trajectory of the data track by using the existing servo patterns

The readback signals from the read head are acquired by a data acquisition card installed on the PC. In every revolution of data reading, the readback signals of the entire data track are sampled and stored in the memory of the data acquisition card. Instead of transferring the whole array of the sampled waveform to the system memory, only the segments containing the servo information are accessed. Modern hard disks usually have 200 to 300 servo sectors per track. In the beginning of each servo sector is the servo data, which is composed of track ID and the servo bursts. The track ID, encoded in gray code, indicates the track number of the track. The signals generated by servo bursts can be used to produce the PES signal, which is linearly proportional to the displacement of the read head from the center of the track. By having the track number and PES signal at each servo sector, the trajectory of the data track can be obtained.

Figure 5.1 shows a small portion of the data tracks whose trajectories are modulated due to eccentricity. The disk is assumed to be static, and the read head flies circularly with respect to its read center if no feedback control signal is applied to the PZT. As shown in the figure, the read head passes through three servo data regions as it flies along the dashed line. One track is crossed as the read head goes from the second servo data region to the third one.
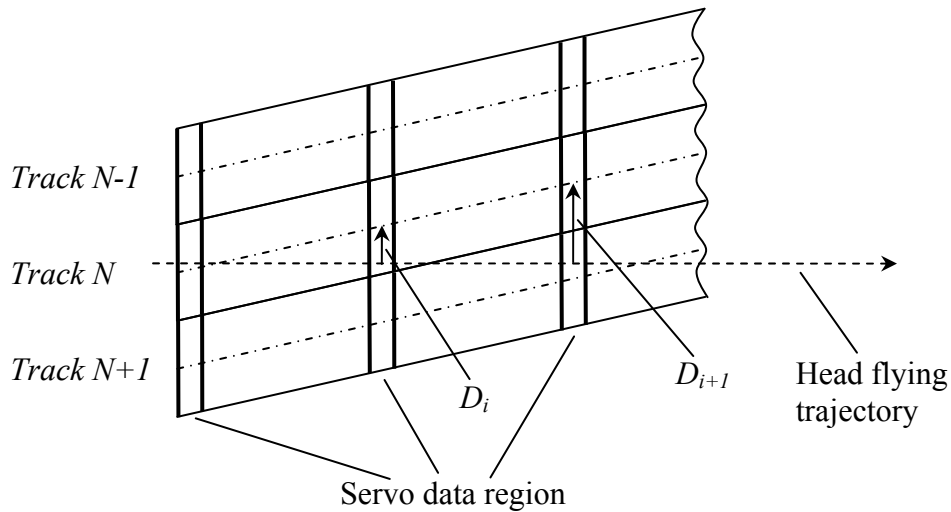
Figure 5.1: A portion of the modulated tracks due to eccentricity.

The displacement from the position of the read head to the center of track N at each servo data region is linearly proportional to D_i, which can be calculated by using the following equation:

$$D_i = P_i + (T_i - T_{i-1}) , \text{i} = 1, 2 \ldots \text{m} \tag{5.1}$$

where P_i and T_i are the PES signal and the track number respectively at the ith servo sector, and m is the total number of servo sectors in the entire track. The trajectory of track N is linearly proportional to the array of D_i where i = 1, 2 … m.

5.1.2 Iterative compensation for the PZT hysteresis

In section 3.3, the PZT hysteresis is compensated by using a measured hysteresis loop. However, the shape of the hysteresis loop might vary while the operating temperature changes. It is expensive to go through all the procedures for measuring a new hysteresis loop as the old one is no longer accurate due to the changing of the temperature. Instead of actually measuring the hysteresis loops, an approach based on iterative compensation for the PZT hysteresis has been developed.

Figure 5.2 illustrates the scheme of the feedback control system which iteratively compensates for the PZT hysteresis. In this scheme, $y(t)$ represents the actual displacement between the position of the read head and the centerline of the track during the entire spindle revolution, and $r(t)$ indicates the reference position which corresponds to the centerline of the track. The displacement sensor measures $y(t)$ by using the servo information existing on the disk. According to this measurement at each iteration, a PC is used to calculate the trajectory of the modulated tracks by using equation (5.1). The integral controller computes the controlling signal to the PZT by using the following equations:

$$u_k(t) = K_I \sum_{i=0}^{k} e_i(t)$$
$$e_i(t) = \frac{y_i(t)}{P} - r_i(t)$$
, where K_I is the integral gain and P is the track pitch. (5.2)

The integral gain K_I is chosen to be equal to P multiplied by α, where α is equal to the inverse of the ratio of the maximum displacement of $y_0(t)$ to the PZT driving voltage corresponding to this maximum and $y_0(t)$ is the original displacement without any input to the PZT. The tracking error $e_i(t)$ is expressed as a percentage of the track pitch while
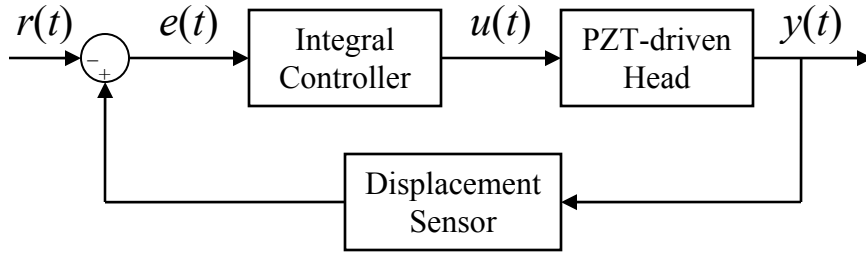
Figure 5.2: Scheme of the feedback control system.

$y_i(t)$ is in units of microns. The reference position $r_i(t)$ is also normalized with respect to the track pitch. Since the PES signal at the centerline of the track is equal to zero, $r_i(t)$ is always zero. Therefore, equation (5.2) can also be written as follows:

$$u_k(t) = K_I \sum_{i=0}^{k} \frac{y_i(t)}{P} = \alpha \sum_{i=0}^{k} y_i(t).$$ (5.3)

α can also be considered as inverse of the average slope of the hysteresis loop. If the relation between the applied voltage and the displacement response of the PZT is absolutely linear (zero hysteresis), the slope at any point of the hysteresis loop will always be inverse of α.

At the 0_{th} iteration ($k = 0$), the control signal to the PZT can be found by using equation (5.3) and expressed as follows:

$$u_0(t) = \alpha \times y_0(t).$$ (5.4)

Assuming that the thermal drift effect can be neglected and the runout $y_k(t)$ is measured accurately, $y_1(t)$ is the remnant runout due to only the PZT hysteresis while the control signal $u_0(t)$ has been applied to the PZT. In other words, $y_1(t)$ will become zero if there are no hysteretic effects. It can be shown that the runout $y_k(t)$ converges to zero as k goes to infinity under the condition that the amount of hysteresis is small.

65

5.1.3 Proof for the convergence of the iterative algorithm

Figure 5.3 (a) shows the displacement response of a typical piezoelectric actuator with respect to the applied voltage. The operating voltage is between 0 and *Vm* volts. Function $F(V)$ represents the hysteresis loop, and function $F_0(V)$ depicts a linear curve with slope of $\tan(\theta)$, which also can be considered as the average slope of the hysteresis loop. By using the value α defined in the previous section, $\tan(\theta)$ can be expressed as:

$$\tan(\theta) = \frac{1}{\alpha}. \tag{5.5}$$

The loop plotted in Fig. 5.3 (b) shows the deviation of $F(V)$ from $F_0(V)$. The function $\phi(V)$ can be expressed as:

$$\phi(V) = F(V) - F_0(V). \tag{5.6}$$

According to the definition of the function $F_0(V)$ and from equation (5.5), we have the following relation:

$$F_0(V) = V \tan(\theta) = \frac{V}{\alpha}. \tag{5.7}$$
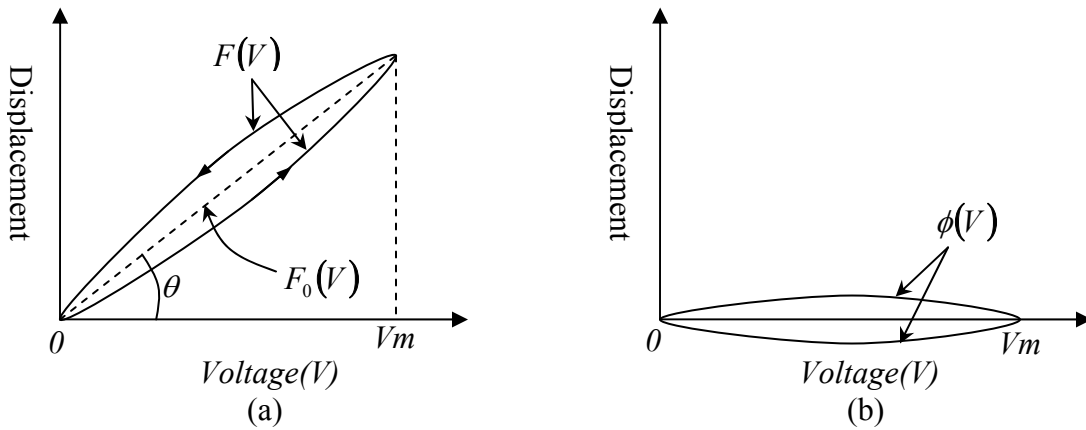
Figure 5.3: Hysteresis loops of a typical PZT.

According to equation (5.3), $u_k(t)$ can be expressed as:

$$u_k(t) = \alpha \sum_{i=0}^{k} y_i(t).$$ (5.8)

The runout in the k_{th} iteration can be found by subtracting the current displacement response of the PZT from the original runout. Therefore, we have the following equality:

$$y_k(t) = y_0(t) - F(u_{k-1}(t)).$$ (5.9)

Substituting (5.8) into (5.9) yields

$$y_k(t) = y_0(t) - F\left(\alpha \sum_{i=0}^{k-1} y_i(t)\right).$$ (5.10)

Equation (5.6) can also be written as:

$$F(V) = F_0(V) + \phi(V).$$ (5.11)

From equation (5.7) and (5.11), the second term on the right of equation (5.10) can also be expressed as:

$$F\left(\alpha \sum_{i=0}^{k-1} y_i(t)\right) = \sum_{i=0}^{k-1} y_i(t) + \phi\left(\alpha \sum_{i=0}^{k-1} y_i(t)\right).$$ (5.12)

Substituting (5.12) into (5.10) results in

$$\sum_{i=1}^{k} y_i(t) = -\phi\left(\alpha \sum_{i=0}^{k-1} y_i(t)\right).$$ (5.13)

Replacing k in equation (5.13) by $k+1$ gives

$$\sum_{i=1}^{k+1} y_i(t) = -\phi\left(\alpha \sum_{i=0}^{k} y_i(t)\right).$$ (5.14)

By subtracting (5.13) from (5.14), we arrive at the following equality:

$$y_{k+1}(t) = \phi\left(\alpha \sum_{i=0}^{k-1} y_i(t)\right) - \phi\left(\alpha \sum_{i=0}^{k} y_i(t)\right).$$ (5.15)

Next, we define q as follows:

$$q = \alpha \max_{0<V<Vm} \left| \frac{d\phi}{dV} \right|.$$ (5.16)

It can be shown that if q is less than 0.5 in magnitude and $y_0(t)$ has only one maximum (which is the case in the application of this dissertation), the following formula can be derived (consult Appendix A for details):

$$|y_{k+1}(t)| \le \left(\alpha \max_{0<V<Vm} \left| \frac{d\phi}{dV} \right| \right) \times |y_k(t)|.$$ (5.17)

Since q is assumed to be less than 0.5, we have the following derivation from (5.17):

$$|y_{k+1}(t)| \le q|y_k(t)|$$ (5.18)

$$|y_{k+1}(t)| \le q^2|y_{k-1}(t)|$$ (5.19)

$$|y_{k+1}(t)| \le q^{k+1}|y_0(t)|$$ (5.20)

$$|y_{k+1}(t)| \to 0 \text{ as } k \to \infty.$$ (5.21)

In other words, the runout will converge to zero if the following condition is satisfied:

$$\alpha \max_{0<V<Vm} \left| \frac{d\phi}{dV} \right| = \frac{\max\limits_{0<V<Vm} \left| \frac{d\phi}{dV} \right|}{\tan(\theta)} < 0.5 ,$$ (5.22)

which means that the derivative of the deviation from $F_0(V)$ due to hysteresis effects has to be always smaller than half of the average slope $\tan(\theta)$ as shown in Fig. 5.3 (a). A typical PZT, such as NEC model #AE0203D08, usually meets the requirement of equation (5.22).

5.2 Experiments and results

The set-up of the track-following system demonstrated in this chapter is exactly the same as that of section 3.5. The same phase-locking system is used to compensate the delay due to the response time of the PZT-based head positioning system. Although the set-up is the same, the open-loop approach of track following there has been converted into a closed-loop system by implementing the algorithm proposed in section 5.1.

In the experiments, the commercial hard disk that is removed from its native drive and mounted on the spin-stand has an average track pitch of 0.21 μm. The GMR head used here has a read width of 0.11 μm. The same PZT (NEC model #AE0203D08) is utilized for the purpose of head positioning. After the hard disk is mechanically centered by using the track-centering algorithm, the amplitude of runout due to eccentricity is about 1.52 μm. By using equation (2.2), one can readily find that there are more than 14 tracks being crossed without any control signal applied to the PZT. As shown in Fig. 5.4, the RRO due to eccentricity and the NRRO mainly resulting from thermal drift are compensated by using the track-following technique proposed in this chapter. It can be seen that the first five iterations are for compensating PZT hysteresis and subsequently the read head is able to stay on track stably. There are 270 servo sectors in the entire track. Figure 5.5 shows the residual radial deviations from the center of the data track at each of the servo sector. It can be seen that the residual radial deviations are mostly within ± 10 nm, which corresponds to one-tenth of the track pitch. Compared to the open-loop approach demonstrated in chapter 2, the accuracy of the close-loop track following presented here is improved by more than 70 %. The average deviation of the 270 servo sectors is observed to be about 3.8 nm.
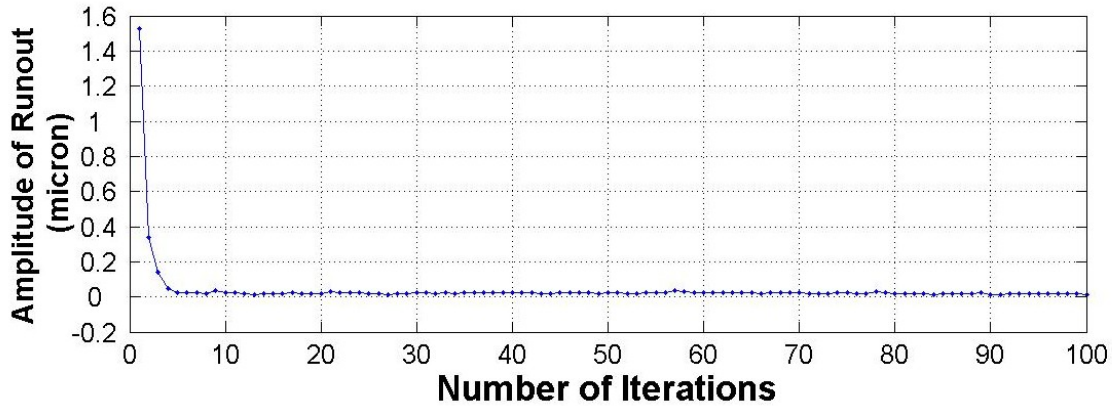
Figure 5.4: Amplitude of runout versus number of iterations of the servo loop.
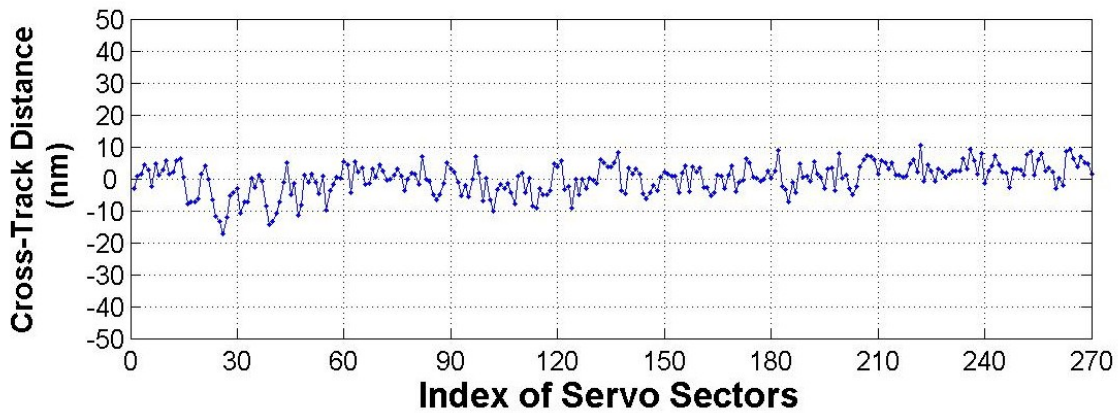
Figure 5.5: Radial deviations from the center of the data track at each of the servo sector.

5.3 Summary

The closed-loop track-following system has been constructed by using the existing servo patterns as the control feedback. The accuracy of track following has been substantially improved as compared to that of the open-loop approach. Since the control signal for each servo sector in the entire track is updated at the same time (in the same iteration) instead of being updated one by one, this track-following technique does not require a very high updating rate of the feedback control signal. Therefore, we do not

need to slow down the spindle speed or eagerly upgrade CPU speed to improve processing capacity. As a result, spin-stand microscopy can be performed at a normal spindle speed. At the same time, we still keep the advantages of low cost and high compatibility provided by the PC-based control systems under Windows NT.

Chapter 6

Spin-Stand Microscopy of

Hard Disk Data

Spin-stand microscopy of hard disk data written on longitudinal media has been studied and many experiment results have been reported [34]-[41]. However, the areal densities of the hard disks used in those results were relatively low (below 35 Gbits/in^2) if compared to that of the modern hard drives whose areal densities are approaching 100 Gbits/in^2. It will be interesting to see the microscopy of hard disks whose areal density has almost reached the predicted superparamagnetic limit of longitudinal recording technology [64]. Besides, since year 2005, perpendicular recording technology has been implemented in hard disk drives and there have been a few products of this technology shipped to the market. Spin-stand microscopy of perpendicularly recorded magnetization

72

patterns on commercial hard disks is also of great interest because it will reveal a lot of information about the state-of-the-art magnetic recording technology, which has been developed and implemented by the industry. In this chapter, spin-stand microscopy of hard disk data written on longitudinal media with ultra-high areal density (close to 100 Gbits/in^2) is studied, and the spin-stand imaging technique is further extended to image hard disk data written on perpendicular media.

6.1 Magnetic recording technology in hard disk drives

There are possibly three modes of magnetic recording. One is longitudinal recording, in which the magnetization is parallel to the disk plane. The second mode is perpendicular recording, in which the magnetization is normal to the disk plane. The third mode is transverse recording, in which the magnetization bit is recorded along the cross-track direction [65]. Longitudinal recording has been the standard method of recording data on hard disks for more than 50 years since the first commercial hard drive was introduced in 1956 by IBM [1]. However, as the conventional magnetic recording technology is finally facing its fundamental limit due to thermal instabilities in the longitudinal media, the strong interest in perpendicular recording as the prime alternative is coming back. The most competitive virtue of this technology is the fact that, while being technically the closest alternative to longitudinal recording, it is able to allow much higher areal density than what can be achieved by longitudinal recording [66]. Transverse recording is not being actively pursued because of various technical constraints. In this section, the principles of longitudinal and perpendicular recording will be briefly reviewed and discussed.

6.1.1 Longitudinal recording

Figure 6.1 shows the schematic diagram of longitudinal recording mode. The preferred direction of the medium magnetization (easy axis) is parallel to the disk plane. A ring-type of inductive write head is used in longitudinal recording. By the fringing field emanating from the air gap of the write element, the magnetization bits are recorded along the track in either the positive or negative direction. If two adjacent bits are oriented in the opposite direction, a strong demagnetizing field will be formed between them. As the grain size in the medium becomes very tiny, the demagnetizing field in the bit transitions can reverse the magnetization of the bits due to thermal fluctuation, which would cause data loss. This phenomenon is the so-called superparamagnetic effect. While the longitudinal recording has reached the areal density limit imposed by the superparamagnetic effect, the hard drive market has moved to the perpendicular recording since Toshiba Corporation announced the world's first commercial hard drives based on perpendicular recording in December, 2004.
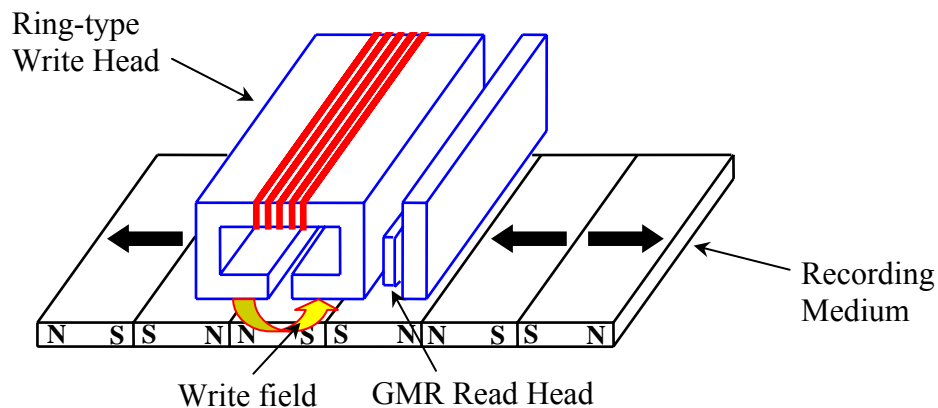
Figure 6.1: A schematic diagram of conventional longitudinal recording scheme.

6.1.2 Perpendicular recording

One of the main advantages of perpendicular recording over longitudinal recording is that it provides a more stable scheme for recording the magnetization bits as illustrated in Fig. 6.2. It is easy to observe that, in longitudinal recording mode, two adjacent bits with opposite orientations repel in a similar way as two bar magnets with poles of the same polarity facing each other. It will be more stable if the two bar magnets are rotated by 90 degree such that their poles do not directly face each other. Meanwhile, the recording density in the along-track direction can also be increased [65].
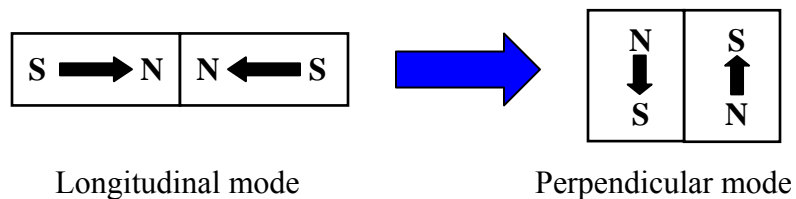
Figure 6.2: A comparative schematic diagram of longitudinal and perpendicular modes.

Figure 6.3 shows the schematic diagram of perpendicular recording mode. The easy axis is perpendicular to the disk plane, and the bits are aligned vertically. A monopole head and a soft underlayer (SUL) are used in the perpendicular recording. In the write process, a strong magnetic field is generated in the gap between the write pole (P1) and SUL. The recording layer that stores the data is directly in this gap where the field is most intense. The SUL, which conducts magnetic flux very readily, guides the magnetic flux back to the return pole (P2). In such geometry, the upper limit of the write field is twice the highest field achievable by using the longitudinal recording mode. As a result, a significantly larger write field can be produced and therefore a higher coercivity medium can be used in the perpendicular recording. A higher coercivity medium provides better

thermal stability, and accordingly the superparamagnetic limit is pushed further back. With the advantages mentioned above and a moderate improvement in signal processing, perpendicular recording is predicted to allow for areal density of 1 Tb/in^2 [67].
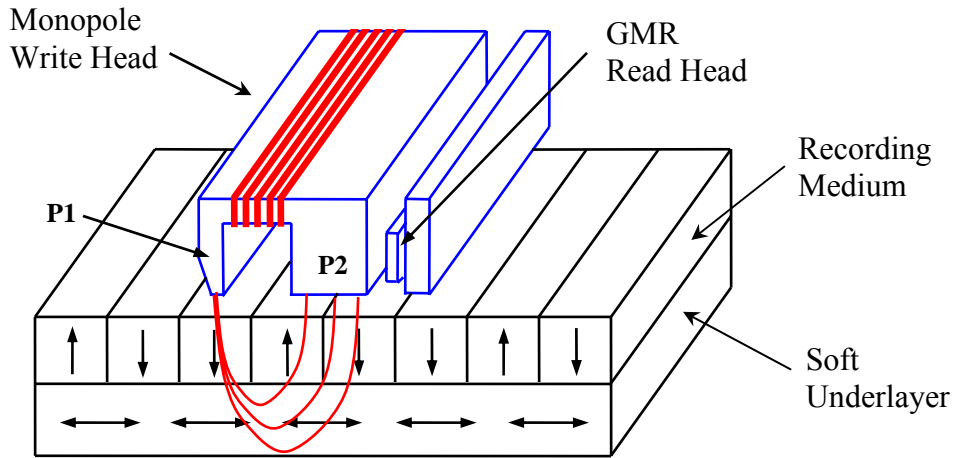
Figure 6.3: A schematic diagram of the perpendicular recording scheme.

6.2 Experiments

By applying the track centering algorithm proposed in Chapter 2 and the track-following technique demonstrated in Chapter 3, 4 and 5, we have been able to image hard disks taken from commercial hard drives with ultra-high areal density. In the experiments, we have four different models of hard disks, including two with longitudinal recording media and the other two with perpendicular recording media. The parameters of the four hard disks are shown in Table 6.1.

The areal density of Disk A is the smallest in Table 6.1 while that of Disk B is already approaching the superparamagnetic limit of longitudinal recording (100 Gbits/in^2). By comparing the parameters of disk B and C, one can observe that the

Disk	Size	Year	Areal Density	Recording Density	Track Density	Recording Method
A	3.5"	2003	54.8 Gbits/in^2	615 Kbits/in	89 Ktracks/in	Longitudinal
B	3.5"	2005	92.1 Gbits/in^2	767 Kbits/in	120 Ktracks/in	
C	3.5"	2006	114.4 Gbits/in^2	781 Kbits/in	145 Ktracks/in	Perpendicular
D	2.5"	2006	131.5 Gbits/in^2	902 Kbits/in	146 Ktracks/in	

Table 6.1: Parameters of hard disks used in the experiments.

recording density in the along-track direction is only increased by less than 2 percent, but the track density is increased by about 20 percent while the recording method was switched from longitudinal mode to perpendicular mode. Disk D is taken from a 2.5-inch notebook hard drive whose recording density in the along-track direction is about 15 percent more than that of disk C. It can be seen that the densities both in the along-track and the cross-track directions have been significantly improved and the barrier of 100 Gbits/in^2 has been conquered by using the perpendicular recording mode

In order to obtain high-resolution images of the ultra-high density hard disks, a high-speed digitizer card (Acqiris DC222) is used to sample the readback signal. The Acqiris DC222 has a bandwidth of 3 GHz and a sampling rate of 8 GS/s. We also upgraded the memory of the digitizer card so that it is capable of storing 128 million points in one single scan. With such a large sampling capacity, we have been able to image hard disks with ultra-high areal density in high resolution. All the images of hard disks were still captured by using a Guzik 1701 MP spin-stand. GMR heads with read width of 0.11 and 0.13 μm were used.

6.3 Hard disk images

Images of hard disks A and B are shown in the top and bottom plot of Fig. 6.4, respectively. The two plots have the same range in the cross-track direction. It can be seen that the image in the bottom plot contains more data tracks than the image in the top plot because the track density of disk B is higher than that of disk A. However, the width of the servo bursts of disk A in the cross-track direction is a little bit smaller than that of disk B. One can observe that the width of the servo bursts of disk A in the cross-track direction is about two-thirds of the track pitch of disk A while that of disk B is as wide as the track pitch of disk B. The images shown in Fig. 6.4 also reveal that the conventional 4-burst servo scheme is still implemented in the modern hard disks based on longitudinal
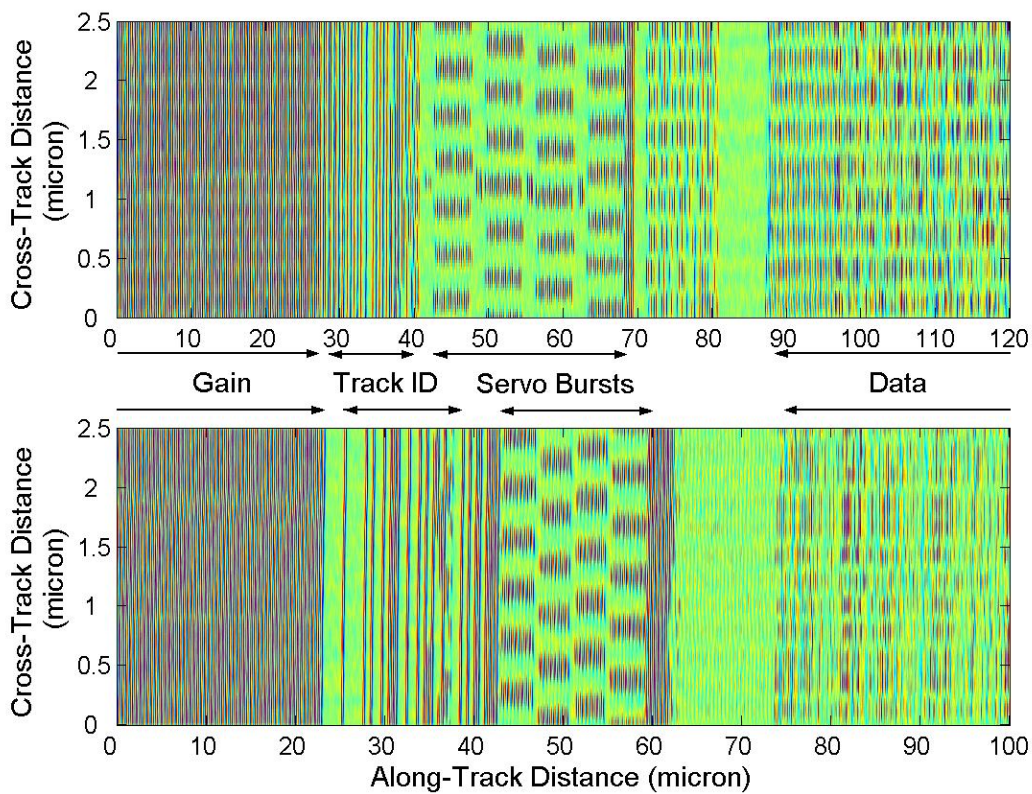
Figure 6.4: Spin-stand microscopy of disk A (top plot) and disk B (bottom plot).

78
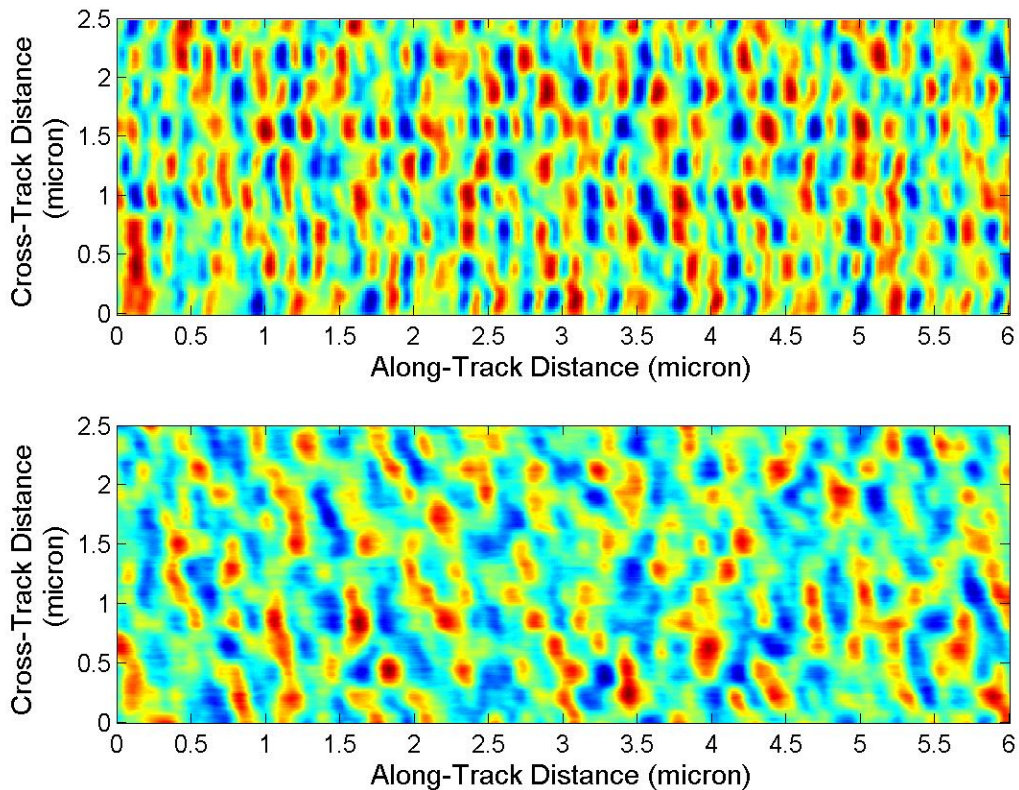
Figure 6.5: User data of disk A (top plot) and disk B (bottom plot).

recording. A 6-burst servo scheme was introduced to improve the positioning accuracy while the areal density was at about 30 Gbits/in^2. However, a 6-burst servo scheme takes more disk area for the servo bursts. This may be the reason that the hard disk manufacturers abandoned the 6-burst servo scheme and went back to the 4-burst servo scheme, which takes less disk area for the servo bursts and provides more disk area for recording user data.

Figure 6.5 presents the user data region of disk A (top plot) and disk B (bottom plot). It is well-known that the effect of intersymbol interference (ISI), which results from the linear superposition of adjacent readback pulses, can cause the decrease of signal amplitude when transitions with opposite polarities are written very closely. In the

images, red and blue color represents positive and negative magnetized regions, respectively. Green color represents the regions which are demagnetized or the magnetization is corrupted by ISI. It can be seen that the distortions caused by ISI is significantly more pronounced in the bottom image than in the top image because the areal density of Disk B is much higher than that of Disk A. The distortions in the images can be removed by the ISI removal technique, which has been proposed in [68].

Figure 6.6 shows the images of hard disk C (top plot) and hard disk D (bottom plot). One can observe that a novel 2-burst servo scheme is implemented in disk C while disk D still uses the conventional 4-burst servo scheme. It can be seen that the 2-burst servo scheme takes only half of the disk area needed for the conventional 4-burst servo scheme
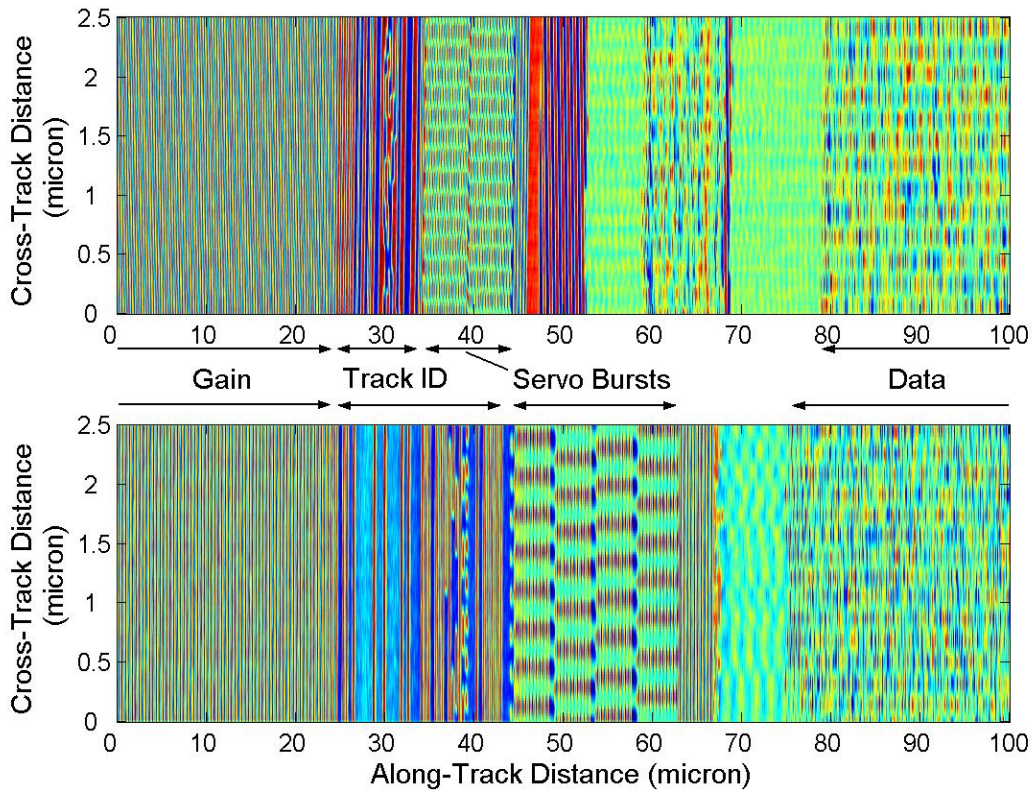
Figure 6.6: Spin-stand microscopy of disk C (top plot) and disk D (bottom plot).
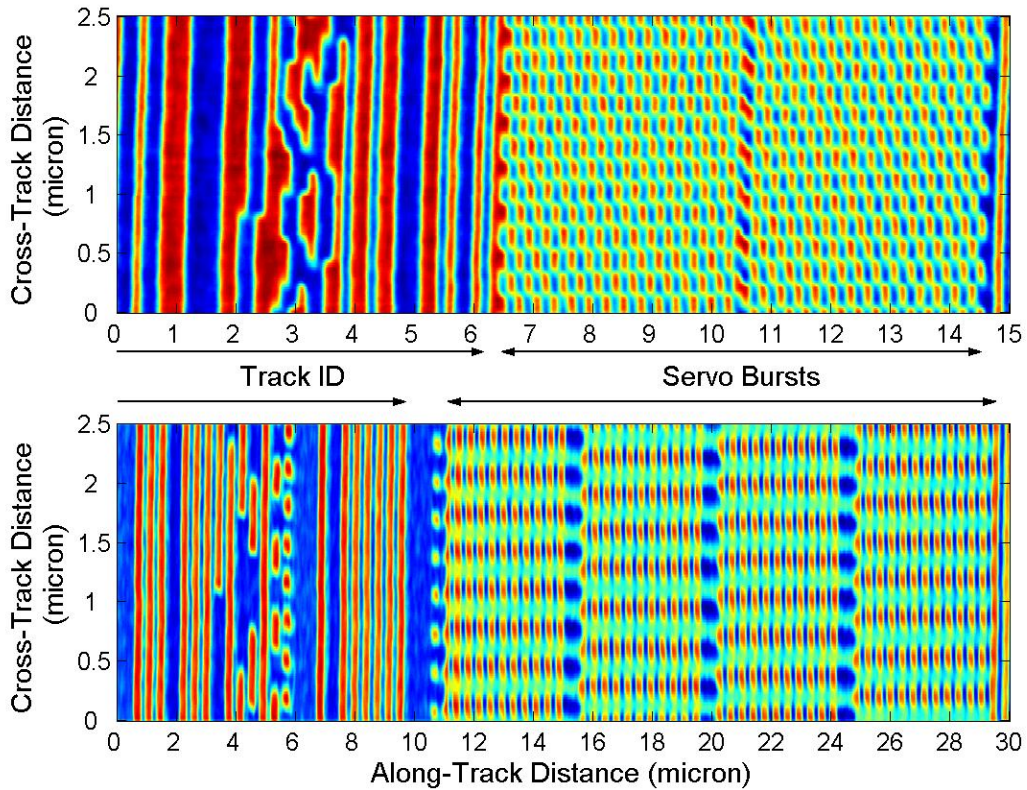
Figure 6.7: Track-id and servo bursts of disk C (top plot) and disk D (bottom plot).

to write the servo bursts. Figure 6.7 shows the zoomed servo region of disk C (top plot) and disk D (bottom plot). The details of the track-id written in Gray code and the servo bursts are clearly shown in these images. In the conventional 4-burst servo scheme, there is no phase difference between two radially adjacent servo bursts as shown in the bottom image of Fig. 6.7. On the contrary, there exist 180 degrees of phase difference between two radially adjacent servo bursts in the 2-burst servo scheme as shown in the top image of Fig. 6.7. Additionally, the gap between two radially adjacent servo bursts in the 2-burst servo scheme is much smaller than that in the conventional 4-burst servo scheme. These are the two crucial features that enable position error signal generation by using only two servo bursts.

Figure 6.8 presents the user data region of disk D whose areal density is more than 130 Gbits/in^2. Although the areal density of disk D is about 40 percent more than that of disk B, it appears that the ISI effect in disk D is smaller than that in disk B if compared to the bottom image of Fig. 6.5. This might be due to the presence of the SUL in disk D. The readback signal strength of perpendicular media with SUL is larger than that of longitudinal media. As a result, the image in Fig. 6.8 shows better color contrast than the bottom image of Fig. 6.5.
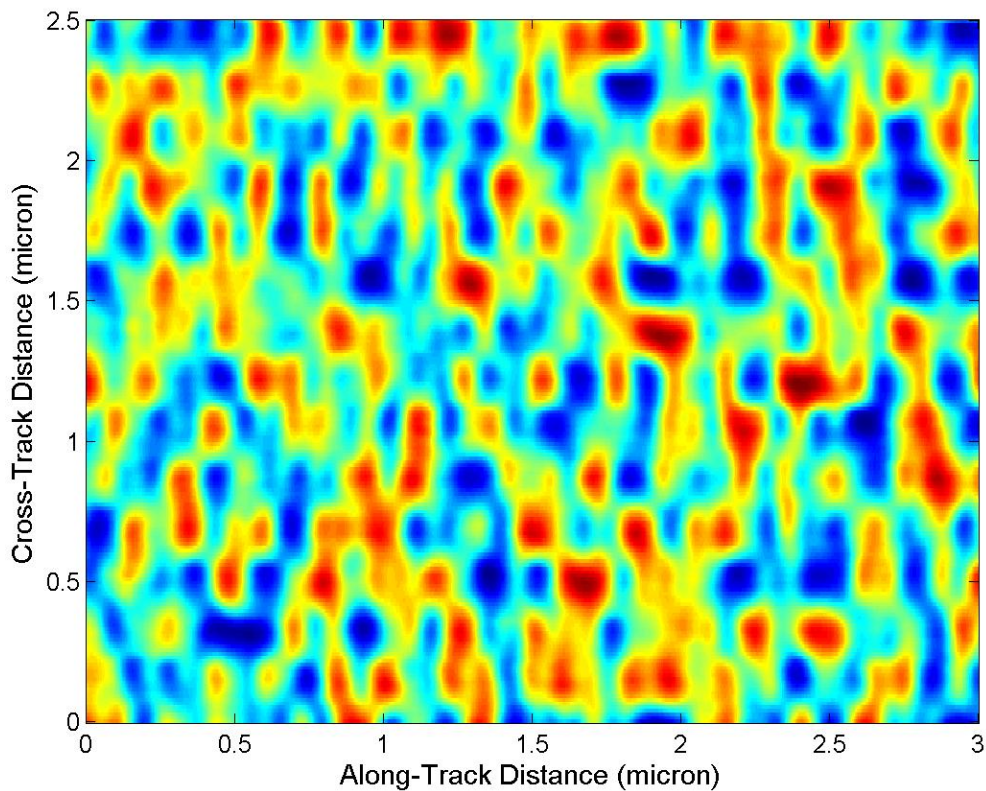
Figure 6.8: User data of hard disk D.

6.4 Summary

With the help of the track-centering algorithm and track-following technique, we have been able to obtain the magnetic microscopy images from any specific region of a commercial hard disk by using a spin-stand. Images of servo-data and user-data regions have been shown in high resolution. The spin-stand microscopy of the servo-data region is extremely useful for diagnostic purposes and analysis of the novel servo schemes. The images of the user-data region can also be helpful for data recovery purposes. In the next chapter, the spin-stand microscopy technique is applied to recover user data written on commercial hard disks. We will see that the spin-stand-based data recovery technique is an extraordinarily powerful and revolutionary tool for recovering hard disk data that was considered to be unrecoverable with the conventional part-replacement technique.

Chapter 7

Drive Independent Recovery of Hard Disk Data

In drive independent data recovery with a spin-stand, we do not rely on any of the components from the original drive, except for the disk platters which actually hold the user data. Theoretically, the lost data can be recovered as long as it is still on the disk platters (the medium that stores the data is not severely contaminated or damaged). The idea is to remove the disk platters from the failed drive, mount them on the spindle of a spin-stand and use the read element of the spin-stand to access the data. The main issues of the spin-stand data recovery technique are eccentricity, track irregularity and nonrepeatable runout due to thermal drift, which prevent the read element of a spin-stand from properly following the data track. In the previous chapters, we have seen that the

issue of runout is compensated by the proposed algorithms and techniques. Now, we are able to readily and efficiently access any of the data sectors of a hard disk on a spin-stand. At this point, the developed techniques seem to bring us close to the desired destination of getting the data. However, this is not the end of the story.

In a modern 3.5-inch HDD, there are more than one hundred million data sectors on each surface of each disk platter. One can imagine that each data sector on a hard disk is like a file folder in one of the drawers of a huge file cabinet. There might be more than one thousand file folders (data sectors) in each drawer (data track) and hundreds of thousand of drawers (data tracks) in the whole file cabinet (hard disk). Each file folder (data sector) contains the same amount of data (512 bytes or 4096 bits). In order to retrieve data files from such a huge storage facility, only having the access to each of the drawers and file folders is not adequate. One must know exactly where the desired data files are stored instead of checking each of the file folders one by one. In other words, one must realize how the storage space in the facility is organized so that one can easily obtain the wanted data files.

Similarly, in spin-stand data recovery, we must have the knowledge about how hard disk designers organize the storage space on a hard disk. However, it is apparent that to record data on a hard disk is much more complicated than to simply put data into a file folder in a file cabinet. In order to achieve the goal of recovering hard disk data on a spin-stand, we must have a good understanding of various aspects of hard disk technology. In this chapter, we will first study the modern hard disk technology. Then, we will discuss the procedures of the spin-stand data recovery. Finally, the demonstration of spin-stand based drive independent data recovery will be presented.

7.1 Hard disk technology

In this section, we will study the technology for storing data on a magnetic hard disk. The three major aspects of hard disk technology that we must explore are hard disk geometry, file systems and hard disk data encoding. Hard disk geometry refers to the internal architecture of a hard disk. Disk file systems provide a method for storing and organizing data files and make it easy for users to find and access them. Data encoding ensures that the data is written and read correctly.

7.1.1 Hard disk geometry

A HDD may contain multiple hard disk platters in the disk pack. Both sides of each platter are coated with magnetic material. Information stored in a HDD is recorded as magnetic patterns in tracks, which are concentric circles on the surfaces of each platter. The tracks are numbered from zero starting at the outermost diameter of the platter. The track number increases as the radius decreases and reaches its limit at the innermost diameter. All the tracks having the same track number (at the same diameter) on each surface of each platter are considered as being of the same cylinder. A HDD uses two read/write heads to record and read data on each platter, one for the top surface and the other for the bottom surface, and each head is numbered starting from zero. The sequence of the head number is usually indexed from the bottom head of the lowest platter to the top head of the highest platter. Each of the concentric tracks is divided into smaller units, called servo sectors. The number of servo sectors is the same across all tracks and across all surfaces of the disk platters. Again, the servo sectors are numbered starting from zero.

Figure 7.1 illustrates the hard disk geometry of a typical HDD. A conceptual drawing of a disk pack, a layered grouping of hard disk platters, is shown in Fig. 7.1 (a). Figure 7.1 (b) is a graphical illustration of the layout of the disk organization. It can be seen from Fig. 7.1 (a) that the disk pack is made up of three hard disk platters. Therefore, each cylinder is composed of a set of six tracks, one per platter surface. There are 16 tracks on each platter surface and 32 servo sectors in each track as shown in Fig. 7.1 (b). The addressing of individual servo sector is done by referring to its position in terms of cylinders, heads and sectors (CHS). For example, in the disk pack shown in Fig. 7.1, the cylinders are numbered from 0 to 15, the heads are numbered from 0 to 5 and the servo sectors are numbered from 0 to 31. The 25th servo sector of track number 10 on the bottom surface of the lowest platter corresponds to the CHS address of cylinder 10, head 0 and sector 25 (the heads are numbered from the bottom to the top).

(a)   (b)
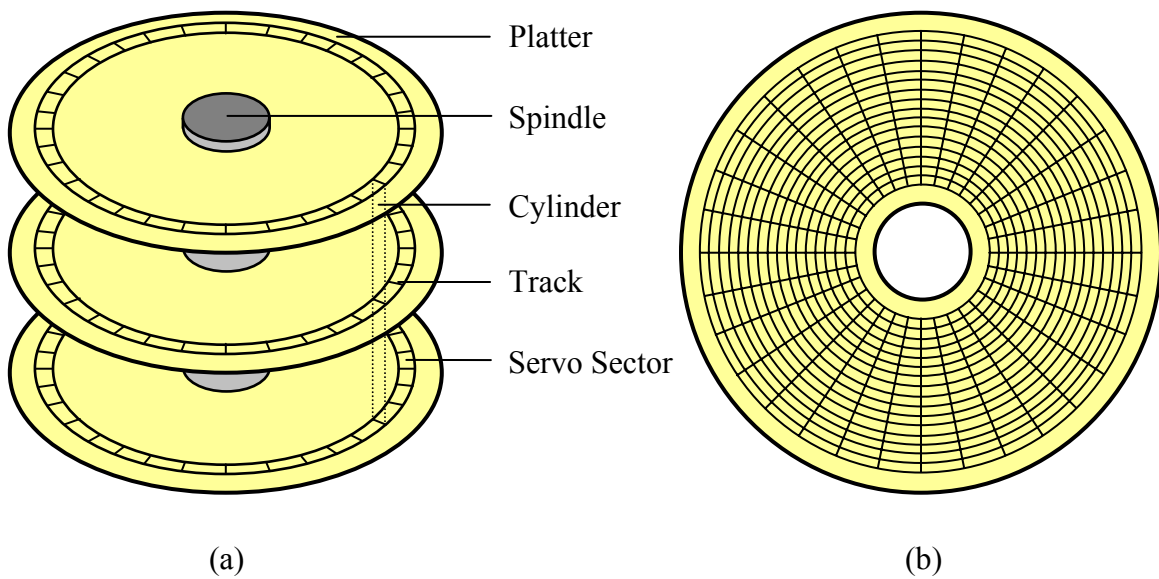
Figure 7.1: (a) Side view of a disk pack. (b) Top view of a disk platter in the disk pack.

The sector servo technology is implemented for the servo positioning as discussed in Chapter 4. The servo information is written at the beginning of each servo sector. The user data is stored in the unit of data sectors. In the earliest design of disk organization, there was only one data sector in each servo sector. The user data was recorded at a constant data rate across all the tracks from the inner diameter (ID) to the outer diameter (OD). Accordingly, each track contains the same number of bits of user data and the same number of data sectors. Each data sector contains 4096 bits (512 bytes) of user data and typically tens of bytes of appended information for error correction. However, to make the number of data sectors the same for all the tracks would greatly underutilize the tracks at the OD. In theory, the tracks at the OD could hold many more data sectors than those at the ID because the circumference of the tracks at the OD is much larger than that at the ID. To improve the utilization of disk space, modern HDDs employ a technology referred to as *zoned bit recording* (ZBR) [69]. With this technology, tracks are grouped into zones based on their radial distances from the center of the disk platter. Each zone is assigned a number of data sectors per track. The radially outward zones contain more data sectors per track than the radially inner zones. The data recording rates and data transfer rates of the radially outward zones are also higher than those of the radially inner zones. Furthermore, in order to take full advantage of the ZBR technology, HDD developers invented a way to split data sectors across a servo sector, instead of insisting on having an integer number of data sectors in each servo sector. Nowadays, a modern HDD usually possesses several hundred data sectors per track at the ID and more than one thousand data sectors per track at the OD while the number of servo sectors (usually about 200 to 300) is the same for all of the tracks on the disk.

The addressing of servo sectors and the addressing of data sectors were the same in the earliest design, but they are different in a newer HDD with ZBR. Since the user data is stored in the unit of data sectors rather than servo sectors, the term "sectors" in HDD documentation usually refers to data sectors and the CHS addressing indicates the addressing of data sectors instead of servo sectors. HDDs with ZBR have different parameters for physical addressing (physical location on the disk) in different zones. In order to address all of the data sectors on the disk in three simple numbers (cylinders, heads and sectors), the method of logical addressing was introduced many years ago. Table 7.1 represents an example showing the difference between physical and logical addressing for an 8.4 GB HDD [70]. The translation between the physical and logical addressing is performed by the hard disk controller. The CHS addressing was once very useful while the disk capacity was still quite small. However, the LBA (logical block addressing) mode is now more popular. LBA introduces a totally new way of addressing data sectors. Instead of referring to a cylinder, head and sector number, each data sector on the disk is assigned a unique sector number (from zero all the way to the maximum number of data sectors minus one). Today, the LBA mode is used in all modern HDDs.

Specification	Physical Addressing	Logical Addressing
Cylinders	7,825	16,278
Heads	8	16
Sectors per Track	195-312	63
Total Sectors	16,408,224	16,408,224

Table 7.1: Sector address translation in CHS mode.

An Operating System (OS) deals with the data sectors of a HDD by using logical addressing and knows nothing about the physical locations of them on the hard disks. Although HDDs of different models might have different mapping of physical to logical addressing, an OS only sees different sizes of hard disk volumes and the sectors in a volume look consecutive to an OS. A hard disk volume can be logically partitioned into smaller volumes, which are independent to one another. Figure 7.2 shows an example of partitioning a hard disk volume into three smaller volumes [71].
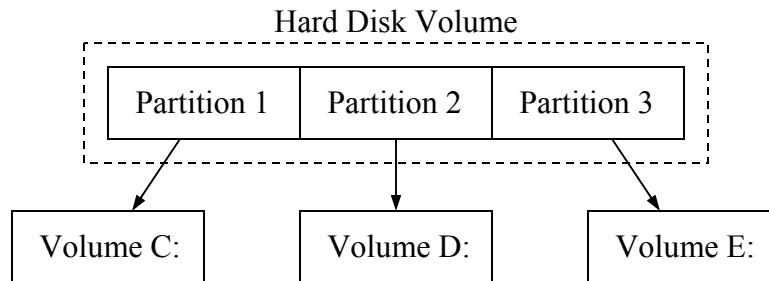
Hard Disk Volume

Figure 7.2: Example of a hard disk volume being partitioned into three smaller volumes.

The most commonly used partition system is the DOS-style partition. Microsoft calls disks using this type of partition system *Master Boot Record* (MBR) disks. A disk that is organized using DOS partitioning has a MBR in the first sector of the disk volume. The MBR contains boot code, partition table and a signature value. The boot code gives the instructions for the computer to process the partition table and locate the OS. The partition table has four entries, each of which can describe a DOS partition with starting CHS address, ending CHS address, starting LBA address, number of sectors in partition, type (file system) of partition and flags. The flag field is used to identify which partition is the bootable one. When the computer is booting, it first processes the partition table in the MBR and then accesses the partition where the OS is located [72].

7.1.2 File system analysis

Disk file systems provide a mechanism for users to store and organize data in a hierarchy of files and directories. In order for an OS to be able to use a partition of the disk volume for storing programs and data, structures of the file system that can be recognized by the OS must be written into that partition. In general, different OSes use different file systems, and different file systems have different structures. Examples of disk file systems include FAT, NTFS, HFS, HFS+, ext2, ext3, ISO 9660 and UDF.

FAT and NTFS were developed by Microsoft. FAT was originally designed for Microsoft DOS and was the primary file system of Windows 9x. NTFS has replaced FAT in newer versions of Windows OSes such as Windows 2000, Windows XP, Windows Server 2003 and Windows Vista. However, because of its simplicity of the design and the compatibility to all existing OSes for personal computers (PCs), the FAT has become an ideal format for floppy disks and solid-state memory cards. HFS and HFS+ are file systems developed by Apple Computer for computers running Mac OS. HFS+ is an improved version of HFS, supporting much larger files. The ext2 and ext3 are file systems commonly used by the Linux OS. ISO 9660 defines a file system for CD-ROM media. UDF is practically the successor of ISO 9660. The first version of UDF is utilized by DVD-Video discs. Today, UDF is widely used for writable and rewritable optical media [73].

Since the FAT file system is supported by all Windows and most Linux OSes, it is frequently encountered in HDD data recovery. The structure of FAT file system and the mechanism of locating a file in the FAT file system are described in Appendix B.1.

7.1.3 Hard disk data encoding

Prior to writing information onto a hard disk, the information must be encoded. The process of information encoding in HDD recording channel can be characterized in two steps. The first step is *error correction encoding*. The error correction code (ECC) introduces additional bits of information, which are used to correct errors encountered during accessing the recorded information. The ECC encoding is followed by *channel encoding*. This step is required in order to avoid long segments of uniform magnetization on the medium. The readback signal from the uniformly magnetized medium contains no transitions, which creates numerous problems during bit detection.

Figure 7.3 illustrates the data writing and reading processes in a typical HDD recording channel. During the process of writing information into a data sector on the disk, the appropriate ECC bits are generated and appended at the end of the stream of input user data bits. The input user data bits along with the ECC bits are then converted into "channel bits" by the channel encoder. Finally, the channel bits are written onto the disk in the form of changing magnetization patterns. When the recorded information is read from the disk, the channel bits are detected by a detector and then converted back to the decoded user data by the channel decoder and the ECC decoder [74].
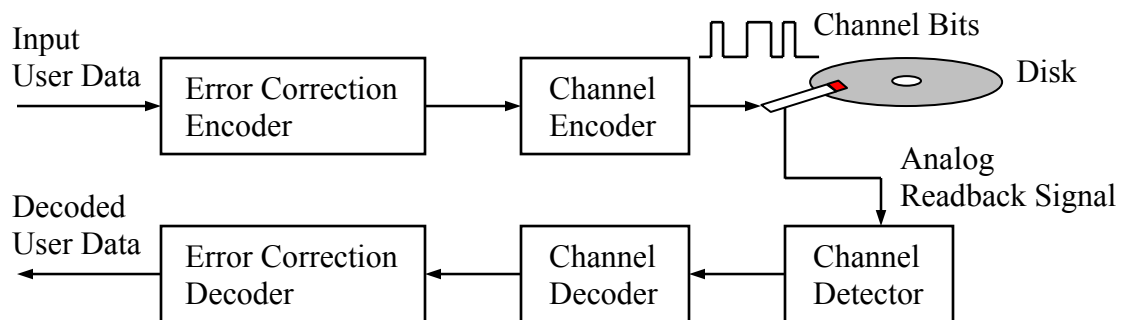
Figure 7.3: Typical HDD recording channel.

In the recording channel of a modern HDD, a data scrambler is usually inserted between the ECC encoder and the channel encoder. A data scrambler pseudo-randomly flips various data bits from 0 to 1 or 1 to 0. Long strings of 1's and 0's or repetitive patterns can be broken up through the randomization caused by a data scrambler. During the writing process of a HDD including a scrambler, the ECC encoded data bits are scrambled with the data scrambler, and then the scrambled data bits are run-length-limited (RLL) encoded by the channel encoder. During the readback process, the RLL decoded bits must be exactly unscrambled in order to return the original ECC encoded data bits. Details about error correction encoding, channel encoding and the encoding scheme of a data scrambler are presented in Appendix B.2.

7.2 Procedures of spin-stand-based drive independent data recovery

In spin-stand-based drive independent data recovery, a spin-stand is used to replace the hardware that is needed for accessing the data written on failed hard disk platters. In other words, a spin-stand provides a universal interface for users to access the data written on hard disk platters from HDDs of any model and any brand. However, a spin-stand does not offer any information about the disk geometry of a particular HDD. In order to realize how the hard disks are physically organized, we have to obtain the disk parameters such as number of tracks per disk surface and number of data sectors per track in each zone. These parameters are not always available in the product manual of a HDD, but they can be found by directly examining the hard disk on a spin-stand.

We must also have the mapping of physical to logical address. The information concerning this mapping is stored in the controller chip of the HDD, but it cannot be easily accessed. A simple approach is to use a donor drive of the same model with the failed drive and record information in each data sector with its own LBA address through a PC. When the user data of a particular data sector on the hard disk taken from the donor drive is recovered on a spin-stand, it gives the logical address of that data sector.

Furthermore, a spin-stand only gives the raw readback signals of the written data. In order to recover the user data itself, these analog readback signals must be processed through a series of procedures, which are shown in Fig. 7.4 [44]. This process consists of five phases: data acquisition, data detection, data decoding, data reconstruction, and data recognition. The first phase, the data acquisition, deals with the issue of disk runout due to several different reasons. The output of the first phase is the on-track readback signals of the data. The readback signals are always distorted by intersymbol interference because of the high areal density. In Phase 2, a programmable PRML channel is used to detect the actual locations of the magnetization transitions. After data detection, we have the encoded binary bit streams of the data. The third phase is to obtain the decoded bit stream from the encoded binary bit streams. The data decoding process includes RLL decoding, descrambling, and ECC decoding. The fourth phase is the reconstruction of the different decoded data sectors into complete files. This involves knowledge of file systems under which the data is organized and geometry of the hard disks on which the data is physically written. The fifth phase is the availability of software programs to recognize the decoded files. Additional work on decryption is needed if the data is encrypted.

It is apparent that the process of recovering hard disk data on a spin-stand is not simple. The five phases shown in Fig. 7.4 must be successfully implemented in sequence before the user data can be recovered. This mission cannot be accomplished by any individual but can only be carried out by a team. The contribution of this dissertation is mainly on Phase 1, the data acquisition. By endeavoring together with other teammates, the five phases in spin-stand data recovery have been worked out. In the next section, we will demonstrate examples of recovering hard disk data by using the proposed spin-stand-based drive independent data recovery technology.
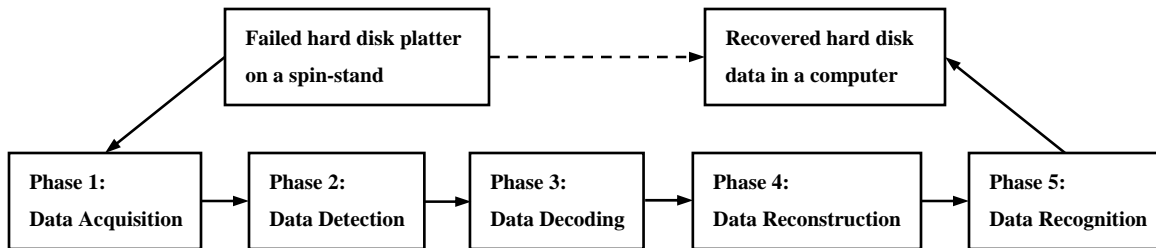
Figure 7.4: Procedures for spin-stand data recovery technology.

7.3 Experiments and results

In the experiments, we tested the spin-stand data recovery technology on a commercial HDD produced in 1997 with a disk capacity of 2.57 gigabytes. The areal density of this HDD is about 0.91 gigabits per square inch. There are 6237 tracks on each platter surface and 48 servo sectors in each track. The number of data sectors per track ranges from 132 to 240 in different zones. This HDD implements an 8/9 (0,4/4) RLL code. This scheme maps 8 user data bits into 9 channel bits. It should be noted that the second "4" requires the maximum number of consecutive "0"s between two "1"s in the odd and even interleaved channel to be 4.

In order to verify that the data decoding channels are programmed correctly, we first wrote a simple pattern throughout the whole surface of the disk platter. We chose "all 1's" to be the user data and wrote it on the hard disk through a PC with a disk editor program. The disk platter was then removed from its native drive and mounted on the spindle of the spin-stand. Through the procedures of data acquisition and data detection, we obtained the input bits to the RLL decoder as shown in the top plot of Fig. 7.5. The middle plot of Fig. 7.5 shows the output bits from the RLL decoder. After passing the RLL decoded data through the descrambler, the user data, which is all 1's, is shown in the bottom plot of Fig. 7.5. This experiment reveals that we have successfully reverse-engineered the different layers of encoding.

Next, we moved forward to the experiments of recovering real computer files. JPEG image files were specially written to the hard disk. We prepared two different JPEG image files. One of them is a gray scale image, which consists of 12 data sectors. The other one is a color image with a size of 120 kilobytes (240 data sectors). Through the procedures in Fig. 7.4, we were able to recover the JPEG images. The upper portion of Fig. 7.6 illustrates the recovered gray image sector by sector. The two images shown in the lower portion of Fig. 7.6 are for comparison between the original image written to the hard disk and the image recovered via spin-stand data recovery. There is no difference between them, which means that this 6-kilobyte JPEG image is completely recovered without any error.

The color image is actually a photograph of a little plant on the ground. Figure 7.7 shows the recovered JPEG images before error correction (top plot) and after error correction (bottom plot). It can be seen that there were three bits of errors (indicated by

the red circles) before using ECC for error correction. Those errors caused offsets and color change to the pixels in the image. The bit error rate is on the order of 10^{-6}, which is equal to the typical error rate of a common HDD before error correction. After error correction, we obtained the JPEG image identical to the original one that was written to the hard disk as shown in the bottom plot of Fig. 7.7.
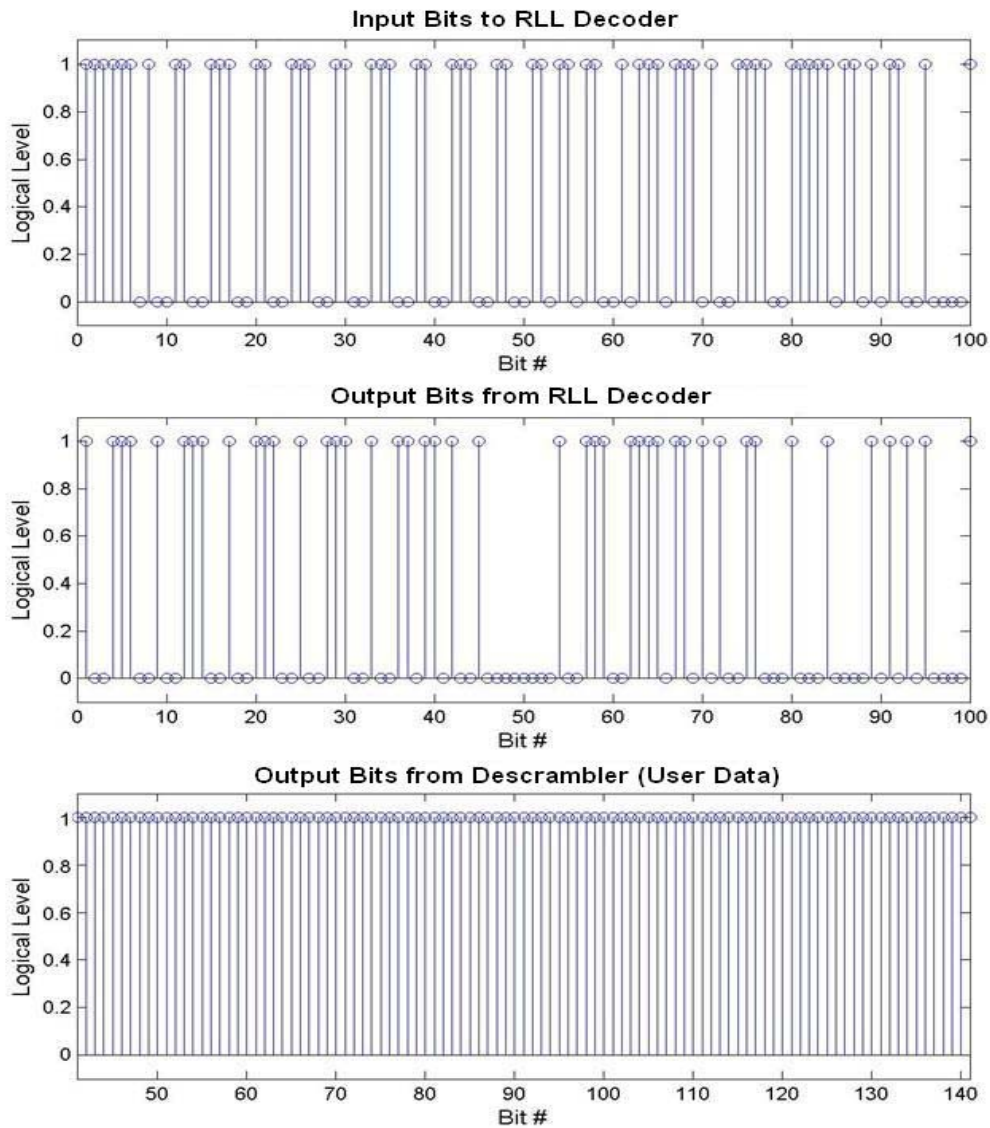
Figure 7.5: An example of channel decoding process.

Figure 7.6: Result of recovering gray JPEG image via spin-stand data recovery.

Recovered Image before Error Correction
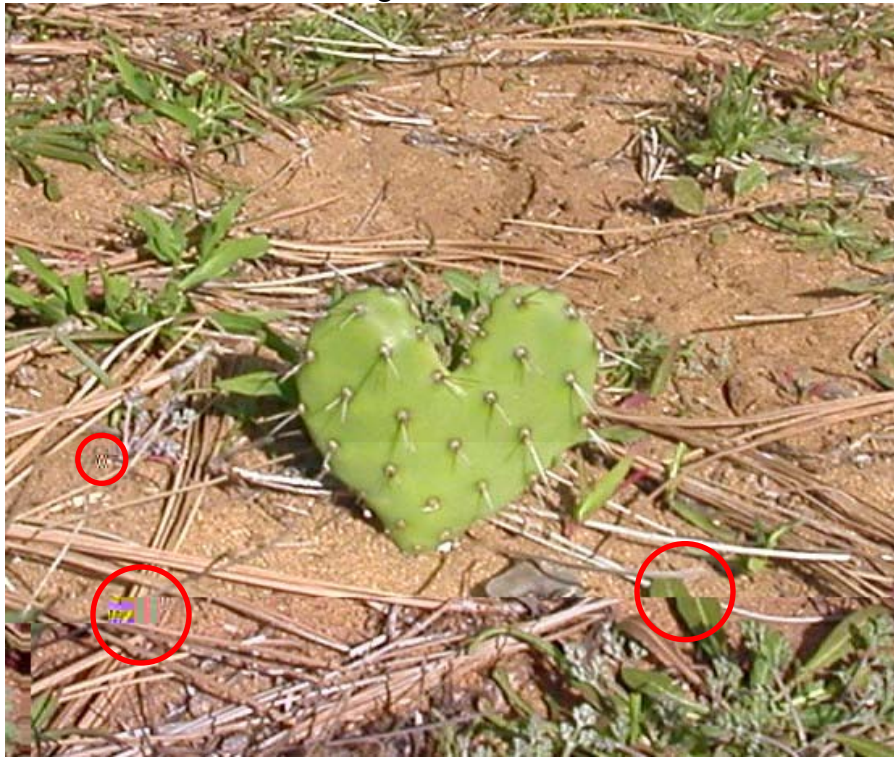
Recovered Image after Error Correction

Figure 7.7: Result of recovering color JPEG image via spin-stand data recovery.

7.4 Summary

Drive independent data recovery based on the technology of spin-stand microscopy has been demonstrated. Procedures of recovering hard disk data on a spin-stand have been illustrated. The experimental results prove that hard disk data on failed hard disk platters can be completely recovered without using any hardware component from the original drive or donor drives. Therefore, this technique can recover hard disk data that was considered to be unrecoverable by current standard data recovery practices. It has applications to both hard disk data recovery and computer forensics.

Chapter 8

Conclusions and Further Study

While several other alternative storage technologies have become available in recent years, hard disk drives (HDD) still dominate the mass data storage market due to their large capacity and low production cost. Meanwhile, the demand in digital storage remains very strong and the data storage market also continues to grow rapidly. This trend has urged the tremendous progress of HDD technology during the recent couple of decades.

The technological progress of HDDs highly relies on the instruments that are capable of performing magnetic microscopy on hard disk platters. A magnetic force microscope was once the most popular device used to execute this task. It has been found that the technique of spin-stand microscopy can be employed to perform the function of a magnetic force microscope with higher imaging rate and larger scanning area [25]. In this dissertation, we improved the accuracy of the spin-stand microscopy technique by

implementing a PZT-based external micro-positioning device on the spin-stand. Special algorithms have been developed to control this micropositioning system. We also derived a track-centering algorithm for removing the track eccentricity. With all the required knowledge in software and computer engineering, the technique of spin-stand microscopy was extended to the application of recovering actual hard disk data from failed HDDs. The following section summarizes the work presented in this dissertation.

8.1 Dissertation summary

An automatic data acquisition system has been developed for the purposes of performing spin-stand microscopy on prewritten hard disk data tracks and accomplishing drive-independent data recovery. This is a PC-based control system and the controlling algorithms are programmed in C++. The PC-based nature of this system enables the automation of the process of data acquisition with low cost and high speed. By using C++ programming, it offers advantages of both programmability and real-time control. As a result, this system provides a high data acquisition rate comparable to an actual HDD.

At the heart of this system are the three techniques: the track-centering technique, the dynamic track-following technique and the servo-based track-following technique. By using the track-centering technique, we are able to efficiently make the center of the prewritten data tracks coincide with the rotational center of the spin-stand spindle so that the track eccentricity can be eliminated. Both the dynamic track-following and servo-based track-following techniques utilize a small piezoelectric actuator (PZT) as the micropositioning device. The former is of an open-loop feedback control scheme, and the feedback comes from the whole-track spin-stand images. The latter is of a closed-loop

feedback control scheme, and the feedback signals are from the existing servo patterns on the disk. The former deals with PZT hysteresis by using a special algorithm based on the Preisach model while the approach taken by the latter is based on iterative compensation.

All the above three techniques play essential roles in this system. The track-centering technique substantially reduces the repeatable runout due to eccentricity. The strength of the dynamic track-following technique is in its ability to handle large track irregularity. The servo-based track-following technique is especially effective at compensating the nonrepeatable runout with high accuracy. The advantages of the two track-following techniques can be combined together when they are integrated to form a dual-stage system, where the first stage (dynamic track following) is for the coarse positioning and the second stage (servo-based track following) is for the fine positioning.

By using the developed techniques, we are able to perform spin-stand microscopy on hard disks taken from commercial hard drives with ultra-high areal densities. Images of hard disk data written on longitudinal media with areal density approaching the predicted superparamagnetic limit (100 Gbits/in^2) have been obtained. Microscopy of hard disk data written on perpendicular media with areal density of as high as 131.5 Gbits/in^2 has also been shown. These images of hard disk data reveal critical information about state-of-the-art technologies employed in modern hard disk drives.

Finally, the automatic data acquisition system was applied to recover actual hard disk data from failed HDDs. It was demonstrated that computer data files such as JPEG images can be successfully and completely recovered through the five phases of spin-stand data recovery process. The approach of recovering hard disk data on a spin-stand can be the only solution to some particular cases of data lost due to hardware failures.

8.2 Future directions

It has been shown that the developed data acquisition system is capable of obtaining magnetic microscopy and performing data recovery on modern hard disks. However, the capability of this system might not be adequate in the near future since the HDD technology is still making progress every year. Consequently, this system must be improved in three different aspects: accuracy, resolution and efficiency.

It is certain that the track density will be further increased with the advancement of HDD technology. When the track pitch become smaller and smaller, nonrepeatable runout (NRRO) due to disk vibration, spindle vibration and spindle bearing runout will be more and more pronounced. Unfortunately, the technique developed in Chapter 5 only deals with NRRO due to thermal drift. In order to maintain the *accuracy* of track following within one-tenth of the track pitch, we might not be able to neglect the NRRO due to sources other than thermal drift when we encounter hard disks with much higher track densities. One of the solutions to this issue is to upgrade the spindle of the existing spin-stand (Guzik 1701-MP) which has been in use for more than ten years. A newer design of spindle can offer better stability and reduce NRRO. Another approach is to develop a track-following technique that provides high servo bandwidth and takes care of the high-frequency runout.

The spin-stand microscopy presented in Chapter 6 shows that distortion due to intersymbol interference (ISI) becomes very severe in hard disks with areal density approaching and beyond 100 Gbits/in^2. Although the distortion due to ISI in the images can be removed by the technique proposed in [67], it is also desirable to obtain raw images of hard disk data with comparable *resolution* to magnetic force microscopy

(MFM). The resolution of spin-stand microscopy can be most effectively improved by using more advanced heads. A potential candidate is a head with an active-head slider, which carries a microactuator and can control the flying height of the head [75]-[77]. As the magnetic sensor of the head is positioned more closely to the recording surface, the interference between adjacent readback pulses will be greatly reduced. Accordingly, the resolution of spin-stand microscopy can be considerably improved by using such a head with flying height control mechanism.

Finally, the *efficiency* of the data acquisition system must also be improved. The most time-consuming part in the process of data acquisition is the algorithm computation performed by a personal computer (PC), which executes various tasks at the same time. We can improve the efficiency of data acquisition by taking away the burden on the CPU of the PC for computing algorithms and putting it on dedicated digital signal processors (DSP). For example, we have to process thousands of data points in order to generate one single feedback signal for servo-based track following. The processing time for the PES generation algorithm could be substantially reduced if the feedback is directly generated by a dedicated DSP.

Appendix A

Recall equation (5.15)

$$y_{k+1}(t) = \phi\left(\alpha \sum_{i=0}^{k-1} y_i(t)\right) - \phi\left(\alpha \sum_{i=0}^{k} y_i(t)\right), \tag{A.1}$$

and also (5.17)

$$\left|y_{k+1}(t)\right| \leq \left(\alpha \max_{0 < V < Vm} \left|\frac{d\phi}{dV}\right|\right) \times \left|y_k(t)\right|. \tag{A.2}$$

We can derive the inequality (A.2) from equation (A.1) if the operator ϕ for the first and second terms in the right hand side of equation (A.1) refers to the same hysteresis loop. This is true if and only if $\sum_{i=0}^{k} y_i(t)$ has only one and the same maximum for any k, which occurs at the same value of t. According to equation (5.13), $\sum_{i=0}^{k} y_i(t)$ can be expressed as:

$$\sum_{i=0}^{k} y_i(t) = y_0(t) - \phi\left(\alpha \sum_{i=0}^{k-1} y_i(t)\right). \tag{A.3}$$

In order to find the critical points of $\sum_{i=0}^{k} y_i(t)$, we have to take the derivative of it. The expression of $\left[\sum_{i=0}^{k} y_i(t)\right]'$ for $k = n$ can be obtained by induction. For $k = 1$,

106

$$\left[\sum_{i=0}^{1} y_i(t)\right]' = [y_0(t)]' - [\phi(\alpha y_0(t))]'.$$ (A.4)

By defining the function ϕ_1 as $\phi(\alpha y_0(t))$, equation (A.4) can be written in the form:

$$\left[\sum_{i=0}^{1} y_i(t)\right]' = [y_0(t)]'\left(1 - \alpha\phi_1'\right).$$ (A.5)

By taking derivative of equation (A.3) for $k = 2$, we have the following equality:

$$\left[\sum_{i=0}^{2} y_i(t)\right]' = [y_0(t)]' - \left[\phi\left(\alpha \sum_{i=0}^{1} y_i(t)\right)\right]'.$$ (A.6)

By using equation (A.3) for $k = 1$, equation (A.6) can also be written as:

$$\left[\sum_{i=0}^{2} y_i(t)\right]' = [y_0(t)]' - \{\phi[\alpha(y_0(t) - \phi(\alpha y_0(t)))]\}'.$$ (A.7)

By employing the definition of ϕ_1 and introducing the function ϕ_2 as $\phi[\alpha(y_0(t) - \phi(\alpha y_0(t)))]$, equation (A.7) can be expressed in the form:

$$\left[\sum_{i=0}^{2} y_i(t)\right]' = [y_0(t)]'\left(1 - \alpha\phi_2' + \alpha^2\phi_1'\phi_2'\right).$$ (A.8)

By taking derivative of equation (A.3) for $k = 3$, we have the following equality:

$$\left[\sum_{i=0}^{3} y_i(t)\right]' = [y_0(t)]' - \left[\phi\left(\alpha \sum_{i=0}^{2} y_i(t)\right)\right]'.$$ (A.9)

By using equation (A.3) for $k = 2$ and $k = 1$, equation (A.9) can also be written as:

$$\left[\sum_{i=0}^{3} y_i(t)\right]' = [y_0(t)]' - \left\{\phi\left[\alpha\left(y_0(t) - \phi\left(\alpha \sum_{i=0}^{1} y_i(t)\right)\right)\right]\right\}'$$

$$= [y_0(t)]' - \{\phi[\alpha[y_0(t) - \phi[\alpha(y_0(t) - \phi(\alpha y_0(t)))]]]\}'.$$ (A.10)

By employing the definition of ϕ_1, ϕ_2 and introducing the function ϕ_3 as

$\phi[\alpha[y_0(t) - \phi[\alpha(y_0(t) - \phi(\alpha y_0(t)))]]]$, equation (A.10) can be written as follows:

$$\left[\sum_{i=0}^{3} y_i(t)\right]' = [y_0(t)]'\left(1 - \alpha\phi_3' + \alpha^2\phi_2'\phi_3' - \alpha^3\phi_1'\phi_2'\phi_3'\right). \tag{A.11}$$

Therefore, the derivative of $\sum_{i=0}^{k} y_i(t)$ for $k = n$ can be expressed as:

$$\left[\sum_{i=0}^{n} y_i(t)\right]' = [y_0(t)]'\left(1 - \alpha\phi_n' + \alpha^2\phi_{n-1}'\phi_n' - \alpha^3\phi_{n-2}'\phi_{n-1}'\phi_n' + \cdots + (-\alpha)^n\phi_1'\phi_2'\cdots\phi_{n-1}'\phi_n'\right),$$

where $\phi_n = \phi\left(\alpha\sum_{i=0}^{n-1} y_i(t)\right)$. \tag{A.12}

Next, we define q by formula:

$$q = \alpha \max_{0 < V < Vm} \left|\frac{d\phi}{dV}\right|. \tag{A.13}$$

By using formula (A.13), we have the following inequality.

$$\left|\alpha\phi_n' - \alpha^2\phi_{n-1}'\phi_n' + \alpha^3\phi_{n-2}'\phi_{n-1}'\phi_n' - \cdots - (-\alpha)^n\phi_1'\phi_2'\cdots\phi_{n-1}'\phi_n'\right|$$
$$\leq \left(q + q^2 + q^3 + \cdots q^n\right) = s. \tag{A.14}$$

The sum s can be expressed as:

$$s = \frac{q - q^{n+1}}{1 - q}. \tag{A.15}$$

From (A.15), it can be readily derived that s is less than 1 if q is less than 0.5.

If $s < 1$, then

$$1 - \alpha\phi_n' + \alpha^2\phi_{n-1}'\phi_n' - \alpha^3\phi_{n-2}'\phi_{n-1}'\phi_n' + \cdots + (-\alpha)^n\phi_1'\phi_2'\cdots\phi_{n-1}'\phi_n' > 0 \quad \text{for any } n. \tag{A.16}$$

From (A.12) and (A.16), it can be concluded that $\left[\sum_{i=0}^{n} y_i(t)\right]' = 0$ if and only if

$[y_0(t)]' = 0$. Thus, the maximum of $\sum_{i=0}^{n} y_i(t)$ and $y_0(t)$ occur at the same time. Next, we

show that $\sum_{i=0}^{n} y_i(t)$ has only one maximum, whose value is $\max[y_0(t)]$ if $y_0(t)$ has only one

maximum. Recall (5.10):

$$y_k(t) = y_0(t) - F\left(\alpha \sum_{i=0}^{k-1} y_i(t)\right).$$ (A.17)

By using (A.17), we shall prove the above statement by invoking the induction argument.

Applying (A.17) for $k = 1$ gives

$$y_1(t_0) = y_0(t_0) - F(\alpha y_0(t_0)), \text{ where } y_0(t_0) = \max[y_0(t)].$$ (A.18)

Since $\alpha y_0(t_0) = V_m$ and $F(V_m) = \max[y_0(t)]$, equation (A.18) can be written as:

$$y_1(t_0) = y_0(t_0) - F(V_m) = y_0(t_0) - \max[y_0(t)] = 0.$$ (A.19)

Applying (A.17) for $k = 2$ with the fact that $y_1(t_0) = 0$ and $\alpha y_0(t_0) = V_m$ gives

$$y_2(t_0) = y_0(t_0) - F\{\alpha[y_0(t_0) + y_1(t_0)]\} = y_0(t_0) - F(V_m) = 0.$$ (A.20)

Applying (A.17) for $k = 3$ with the fact that $y_1(t_0) = y_2(t_0) = 0$ and $\alpha y_0(t_0) = V_m$ gives

$$y_3(t_0) = y_0(t_0) - F\{\alpha[y_0(t_0) + y_1(t_0) + y_2(t_0)]\} = y_0(t_0) - F(V_m) = 0.$$ (A.21)

According, $y_k(t_0) = 0$ for any $k \geq 1$. As a result,

$$\max \sum_{i=0}^{n} y_i(t) = \sum_{i=0}^{n} y_i(t_0) = y_0(t_0) = \max[y_0(t)].$$ (A.22)

In conclusion, if q is less than 0.5 and $y_0(t)$ has only one maximum, then $\sum_{i=0}^{n} y_i(t)$ has only

one and the same maximum. Consequently, on each iteration the same hysteresis loop is

followed.

Appendix B

B.1 FAT file system

Most file systems, including FAT, group consecutive sectors to form a data unit (called a cluster) and assign it a logical file system address. It is not necessary that a file system assigns a logical file system address to every sector in the volume. Figure B.1 shows a volume with 20 sectors and their logical volume addresses. Below them are the logical file system addresses. This file system creates data units in groups of four sectors and the file system does not assign file system addresses until sector 3 [78].

Volume Address	0	1	2	3	4	5	6	7	8	9	10	11	12	13	14	15	16	17	18	19

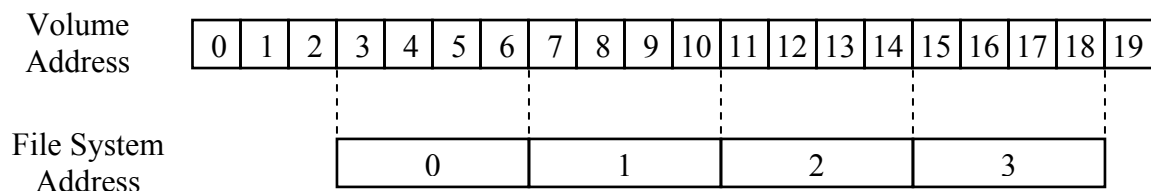| File System Address	0	1	2	3

Figure B.1: Example of assigning file system addresses to sectors in a volume.

The layout of the FAT file system has three sections as shown in Fig. B.2. The first section is the *reserved area*, and it starts in sector 0 of the volume (partition). The boot

sector, storing information about the volume, can be found in the beginning of the reserved area. The second section is the *FAT area*, and it contains the primary and backup file allocation tables, index tables indicating which data is contained in which cluster. It starts in the sector following the reserved area. The third section is the *data area*, occupying the majority of the volume space. It contains the clusters that will be allocated to store file and directory content.

Reserved FAT Root   Data
Area Area Directory   Area

Figure B.2: Layout of the FAT file system.

In the FAT file system, a directory is also a file. The content of a directory file is a table of directory entries which describes the list of files in that directory. A directory entry contains the file name, file size, time stamp and the address of the first cluster of the file content. The root directory, which contains directory entries for files and sub-directories on the root, can be found in the beginning of the data area. In order to find a file in the volume, one must start from the root directory and go through a certain number of sub-directories until one reaches the sub-directory under which the file is located. If a file has allocated more than one cluster, the other clusters are found by using the FAT.

Figure B.3 illustrates an example of accessing a file in a volume using FAT file structure with cluster size of 4096 bytes. The directory entry of the file indicates that the file whose file name is "File1.txt" with file size of 5,000 bytes starts at cluster 20 (cluster addresses start from the beginning of the data area). Because the size of the file is over 4096 bytes (cluster size), one must refer to the FAT entry for cluster 20 and obtain the

cluster address of the next part of the file. The entry contains the value 21, which means that cluster 21 is the next cluster in the file. The FAT entry for cluster 21 contains the End of File (EOF) marker as it is the final cluster in the file [79].
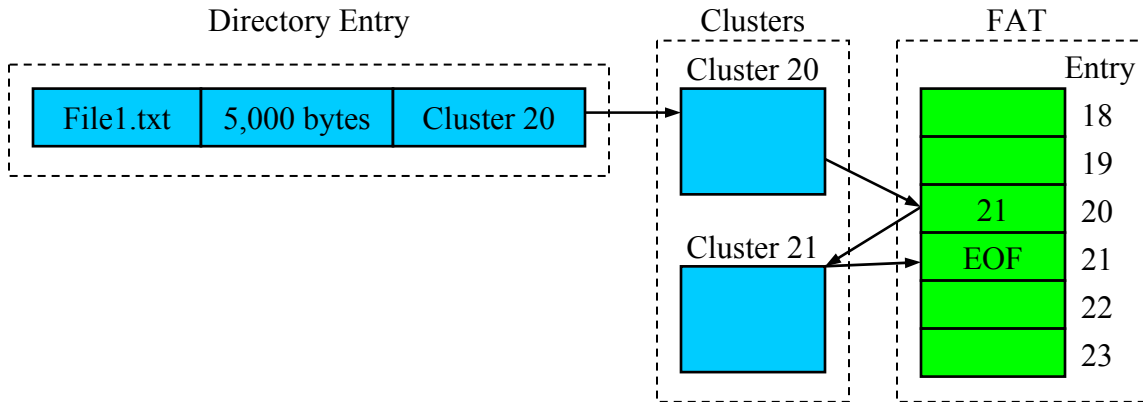
Figure B.3: Relationship between directory entries, clusters and FAT.

B.2 Hard disk data encoding schemes

B.2.1 Error correction encoding

It is not abnormal for a HDD to encounter errors during reading. There are generally two types of errors, single-bit errors and burst errors. Single-bit errors typically occur due to a single short-duration noise event, which results in an extra pulse or a missing pulse. Burst errors usually occur due to defects of magnetic medium, which cause a group of bits detected erroneously. However, having errors appear to the user while using a HDD for data storage is unacceptable. Several different types of ECC codes have been invented over the years. Nowadays, Reed-Solomon algorithm is commonly implemented in a modern HDD for error correction because of its symbol oriented property, which makes it especially well suited to correcting burst errors.

A Reed-Solomon code is usually specified as RS (n,k) and operates on s-bit symbols, where $n = 2^s - 1$. The encoder takes k data symbols unchanged and adds $2t$ parity symbols to make an n symbol codeword as shown in Fig. B.4. In the decoding procedure, the decoder processes the received data symbols along with the parity symbols in order to locate the errors and correct them. If multiple bits in a symbol are corrupted, it only counts as a single error. Errors whose locations are known in advance are called erasures. A Reed-Solomon decoder is capable of correcting up to t errors or up to $2t$ erasures in a codeword, where $2t = n - k$. The most popular family of Reed-Solomon codes used in HDDs is RS (255,223) with 8-bit symbol, where a symbol is a byte. The decoder of RS (255,223) can locate and correct up to 16 bytes of errors occurred anywhere in the codeword [80].
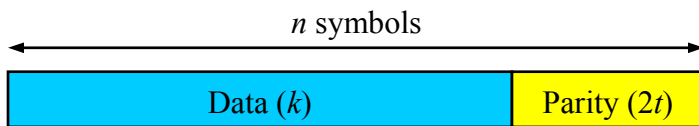
Figure B.4: A Reed-Solomon codeword.

B.2.2 Channel encoding

One of the early codes used to minimize the length of continuous regions of uniformly magnetization was the frequency modulation (FM) code. In the scheme of FM code, a one is recorded as two consecutive transitions, and a zero is recorded as a transition followed by no transition. The average number of transitions per bit on a random stream pattern with FM code is 1.5. A modified frequency modulation (MFM) code was later proposed to improve FM code by reducing the number of transitions per bit. In the scheme of MFM code, a one is recorded as a transition preceded by no

transition. A zero is recorded as a transition followed by no transition only if it is preceded by another zero. Otherwise a zero is recorded as no transitions. The average number of transitions per bit on a random stream pattern with FM code is 0.75 [81]-[82].

Since the average number of transitions per bit of MFM is only half that of FM, the MFM encoded bit rate can be twice as high as the FM encoded bit rate (assuming that the minimum distance between two consecutive transitions is fixed). Although FM and MFM codes are simple, they are not economical because they actually encode each user data bit into two channel bits. The code rate, ratio of the user bits to the encoded channel bits, equals 0.5. In other words, 50% of the disk space is lost to channel encoding.

Run-length-limited (RLL) codes improve the code rate by grouping several bits together instead of encoding one bit at a time. RLL codes are typically characterized by four parameters: m, n, d, k, and are referenced as m/n (d,k) codes. It maps m user data bits into n channel bits. Therefore, the code rate of RLL codes equals m/n. The closer the code rate approaches 1.0, the less the disk space is lost to channel encoding. Parameters d and k are the minimum and maximum number of consecutive "0"s between two "1"s. A typical encoding table for 2/3 (1,7) code is shown in Table B.1 [83].

User bits	00	01	10	11	0000	0001	1000	1001
Encoded Channel bits	101	100	001	010	101000	100000	001000	010000

Table B.1: An encoding table for 2/3 (1,7) code.

When encoded channel bits are written on the magnetic medium, each "0" or "1" is transformed into write current waveform. In longitudinal recording, the read head detects only transitions between different directions of magnetization. Therefore, it is often

114

convenient to represent the write current waveform in the manner of denoting each "0" as "no transition" and each "1" as a transition. This representation is usually called the NRZI scheme [84]. Figure B.5 compares the write current waveforms of the byte "11000110" encoded by FM, MFM and 2/3 (1,7) RLL codes respectively. Using the same distance between two consecutive transitions in the waveform, it can be seen that MFM encodes the same number of user data bits in half of the disk space required by FM encoding. The 2/3 (1,7) RLL code further reduces the amount of disk space required for MFM to encodes the same user data bits by 25 percent because it converts the 8 user data bits into 12 channel bits rather than 16 channel bits [85].
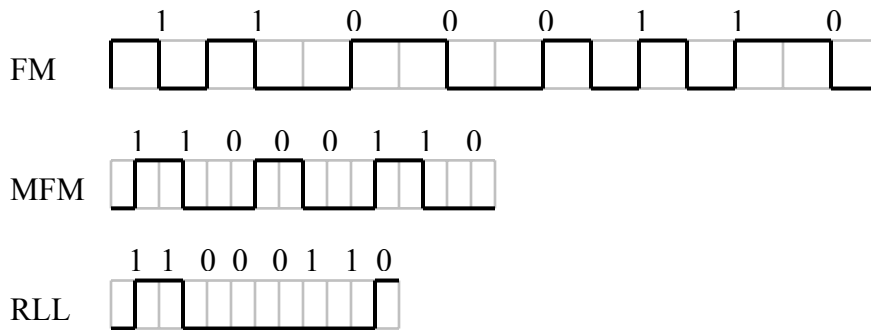
Figure B.5: Write current waveforms of encoded channel bits for the byte "11000110".

B.2.3 Data scrambler

Figure B.6 shows the block diagram of a typical data scrambler, where $x(n)$ is the scrambler input and $y(n)$ is its output. The symbol D represents a single stage of a shift register (a delay element). All the adders perform modulo-2 addition, which is equivalent to the XOR logical operation. The scrambler input and output are related by the equation

$$y(n) = x(n) + \sum_{k=1}^{m} h_k y(n-k) \tag{B.1}$$

The h_k's can be 0 or 1, with 0 indicating no connection to the adder and 1 indicating a connection. Assuming that the input $x(n)$ is 0, the scrambler generates a periodic output sequence of period no greater than $2^m - 1$ if the initial shift register state is nonzero [86].

Figure B.6: The block diagram of a typical data scrambler.

Bibliography

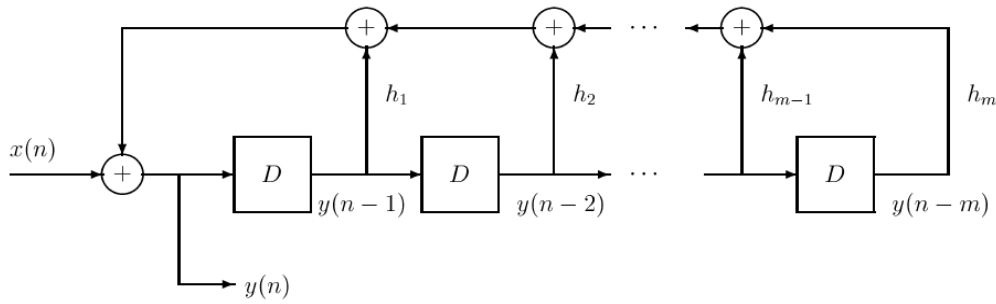1. E. Daniel, C. Mee, and M. Clark, *Magnetic Recording The First 100 Years*, chapter 18, IEEE Press, 1999.

2. H. N. Bertram, H. Zhou, and R. Gustafson, "Signal to noise ratio scaling and density limit estimates in longitudinal magnetic recording," *IEEE Trans. Magn.*, vol. 34, pp. 1845–1847, 1998.

3. D. Weller and A. Moser, "Thermal effect limits in ultrahigh-density magnetic recording," *IEEE Trans. Magn.*, vol. 35, pp. 4423–4439, 1999.

4. M. L. Plumer, J. van Ek and D. Weller (Eds.), *The Physics of High Density Magnetic Recording*, chapters 5 and 6, Springer, Berlin, 2001.

5. Perpendicular Recording, available at www.hitachigst.com/hdd/research/recording_head/pr/index.html

6. Seagate Breaks World Magnetic Recording Density Record - 421 Gbits Per Square Inch Equivalent to Storing 4,000 Hours of Digital Video on Your PC, available at www.seagate.com/cda/newsinfo/newsroom/releases/article/0,1121,3301,00.html

7. H. Katayama, S. Sawamura, Y. Ogimoto, J. Nakajima, K. Kojima, and K. Ohta, "New magnetic recording method using laser assisted read/write technologies," *J. Magn. Soc. Jpn.*, vol. 23, pp. 233–234, 1999.

8. H. Katayama, M. Hamamoto, J. Sato, Y. Murakami, and K. Kojima, "New developments in laser-assisted magnetic recording," *IEEE Trans. Magn.*, vol. 36, pp. 195–199, 2000.

9. H. Saga, H. Nemoto, H. Sukeda, and M. Takahashi, "New recording method combining thermo-magnetic writing and flux detection," *Jpn. J. Appl. Phys.*, vol. 38, pp. 1839–1840, 1999.

10. S. E. Lambert, I. L. Saunders, A. M. Patlach, M. T. Krounbi, and S. R. Hetzler, "Beyond discrete tracks: other aspects of patterned media," *J. Appl. Phys.*, vol. 69, pp. 4724–4726, 1991.

11. S. Y. Chou, M. S. Wei, P. R. Krauss, and P. B. Fisher, "Single-domain magnetic pillar array of 35 nm diameter and 65 Gbits/in.^{2} density for ultrahigh density quantum magnetic storage," *J. Appl. Phys.*, vol. 76, pp. 6673–6675, 1994.

12. R. L. White, R. M. H. New, and R. F. W. Pease, "Patterned media: a viable route to 50 Gbit/in^2 and up for magnetic recording?," *IEEE Trans. Magn.*, vol. 33, pp. 990–995, 1997.

13. C. T. Rettner, M. E. Best, and B. D. Terris, "Patterning of granular magnetic media with a focused ion beam to produce single-domain islands at >140 Gbit/in^2," *IEEE Trans. Magn.*, vol. 37, pp. 1649–1651, 2001.

14. R. L. White, "The physical boundaries to high-density magnetic recording," *J. Magn. Magn. Mater.*, vol. 209, pp. 1–5, 2000.

15. T. W. McDaniel, "Ultimate limits to thermally assisted magnetic recording," J. Phys.: Condens. Matter, vol. 17, R315–R332, 2005.

16. E. Grochowski, "Average price of storage," available at www.hitachigst.com/hdd/hddpdf/tech/chart03.pdf

17. Y. Martin and H. K. Wickramasinghe, "Magnetic imaging by 'force microscopy' with 1000 $\overset{o}{A}$ resolution," *Appl. Phys. Lett.*, vol. 50, pp. 1455–1457, 1987.

18. H. J. Mamin, D. Rugar, J. E. Stern, B. D. Terris, and S. E. Lambert, "Force microscopy of magnetization patterns in longitudinal recording media," *Appl. Phys. Lett.*, vol. 53, pp. 1563–1565, 1988.

19. D. Rugar, H. J. Mamin, P. Guethner, S. E. Lambert, J. E. Stern, I. McFayden, and T. Yogi, "Magnetic force microscopy: General principles and application to longitudinal recording media," *J. Appl. Phys.*, vol. 68, pp. 1169–1183, 1990.

20. P. Rice, B. Hallett, and J. Moreland, "Comparison of magnetic fields of thin-film heads and their corresponding bit patterns using magnetic force microscopy," *IEEE Trans. Magn.*, vol. 30, pp. 4248–4250, 1994.

21. X. Song, J. Sivertsen, and J. Judy, "Magnetic force microscopy images of ultrahigh-density bit patterns recorded on high-coercivity longitudinal and perpendicular thin-film media," *J. Appl. Phys.*, vol 79, 4912–4914, 1996.

22. K. Sin, P. Glijer, J. M. Sivertsen, and J. H. Judy, "Magnetic force microscopy studies of ultrahigh density magnetic recording on longitudinal and perpendicular media," *IEEE Trans. Magn.*, vol. 33, pp. 1052–1057, 1997.

23. E. B. Svedberg, S. Khizroev, and D. Litvinov, "Magnetic force microscopy study of perpendicular media: Signal-to-noise determination and transition noise analysis," *J. Appl. Phys.*, vol 91, 5365–5370, 2002.

24. D. Guarisco and H. Nguy, "High linear density in perpendicular recording," *J. Appl. Phys.*, vol 93, 6745–6747, 2003.

25. I. D. Mayergoyz, C. Serpico, C. Krafft, and C. Tse, "Magnetic imaging on a spin-stand," *J. Appl. Phys.*, vol 87, 6824–6826, 2000.

26. S. G. McCarthy and Z. A. Keirn, "Distance enhancing codes for E^2PRML: performance comparison using spinstand data," *IEEE Trans. Magn.*, vol. 33, pp. 2734–2736, 1997.

27. J. S. Goldberg and J. K. Wolf, "Implementation and analysis of nonlinear effects in the microtrack model," *IEEE Trans. Magn.*, vol. 35, pp. 2256–2258, 1999.

28. P. Dhagat, R. S. Indeck and M. W. Muller, "Spin-stand measurements of time and temperature dependence of magnetic recording," *J. Appl. Phys.*, vol 85, 4994–4996, 1999.

29. E. N. Abarra*,* I. Okamoto, K. Sato, Y. Yoshida, H. Akimoto, and Y. Uematsu, "Low noise properties and thermal stability of Co-based thin film media for high density longitudinal recording," *IEEE Trans. Magn.*, vol. 36, pp. 86–91, 2000.

30. S. Shi, F. Liu, H. Chen, Y. Chen, K. Stoev, R. Saha, H. Tong, and S. Dey, "Demonstration of 1 Gbit/sec magnetic recording using an integrated inductive write/GMR read head," *IEEE Trans. Magn.*, vol. 36, pp. 2517–2519, 2000.

31. R. M. Brockie and H. J. Richter, "Thermal decay study of various magnetization patterns," *IEEE Trans. Magn.*, vol. 38, pp. 1946–1948, 2002.

32. P.D. Mathur and W.C. Messner, "Evaluation of test procedures for determining servo compatibility of heads and media in magnetic disk drives," *IEEE Trans. Magn.*, vol. 38, pp. 1575–1592, 2002.

33. Z. Jin, C. Fu, X. Wang, Y. Zhou, and J. Fernandez-de-Castro, "Spinstand measurement of head keeper spacing in perpendicular recording," *IEEE Trans. Magn.*, vol. 42, pp. 2270–2272, 2006.

34. C. Tse, I.D. Mayergoyz, C. Krafft, and A. Adly, "Spin-stand study of data dependent thermal relaxations of magnetization patterns," *J. Materials Processing & Manufacturing Science*, vol. 9, 82, 2000.

35. I.D. Mayergoyz, C. Tse, C. Krafft, and R.D. Gomez, "Spin-stand imaging of overwritten data and its comparison with magnetic force microscopy," *J. Appl. Phys.*, vol. 89, pp. 6772–6774, 2001.

36. I.D. Mayergoyz, C. Tse, C. Krafft, and A. Adly, "Spin-stand imaging of transverse magnetization profiles of recorded tracks," *J. Appl. Phys.*, vol. 89, pp. 6775–6777, 2001.

37. C. Tse, D.I. Mircea, I.D. Mayergoyz, C. Krafft, and P. Andrei, "Spatial and vectorial characterization of thermal relaxation using the spin-stand imaging technique," *J. Appl. Phys.*, vol. 91, pp. 8846–8848, 2002.

38. I.D. Mayergoyz, C. Tse, C. Krafft, D.I. Mircea, and P. Andrei, "Extraction of the response function of GMR head for spin-stand imaging," *IEEE. Trans. Magn.*, vol. 38, pp. 2453–2455, 2002.

39. C. Tse, I.D. Mayergoyz, C. Krafft, and D.I. Mircea, "High-speed massive imaging of hard disk data by using the spin-stand imaging technique," *J. Appl. Phys.*, vol. 93, pp. 6578–6580, 2003.

40. I.D. Mayergoyz, C. Tse, C. Krafft, and D.I. Mircea, "Scaling of head response function in the spin-stand imaging technique," *J. Appl. Phys.*, vol. 93, pp. 6581–6583, 2003.

41. C. Tse, "Magnetic imaging of hard disk drives on a spin-stand," *Ph.D. dissertation*, University of Maryland, 2003.

42. A. S. Chekanov, E. N. Abarra and G. Choe, "Perpendicular recording media imaging using dynamic read-back microscopy," *IEEE. Trans. Magn.*, vol. 42, pp. 2345–2347, 2006.

43. C. H. Sobey, "Recovering unrecoverable data: the need for drive-independent data recovery," available at www.actionfront.com

44. C. Tse, C. Krafft, I. Mayergoyz, P. McAvoy, and C. Y. Tseng, "Forensic recovery of hard disk data by using the spin-stand imaging technique," *Proc. SPIE*, vol. 5778, pp. 595–606, May 2005.

45. C. H. Sobey, L. Orto, and G. Sakaguchi, "Drive-independent data recovery: the current state-of-the-art," *IEEE. Trans. Magn.*, vol. 42, pp. 188–193, 2006.

46. P. K. Subrahamanyan, P. J. Korkowski, W. A. Farahat, S. C. Ehret, G. J. Severson, T. S. Rasmussen, A. Van der Schans, A. H. Sacks and J. H. McGlennen, "High bandwidth large stroke spin-stand for data storage component testing," U.S. Patent Application Publication, Pub. No. U.S. 2003/0002198, January 2003.

47. C. Tse, C. Tseng, P. McAvoy, I. Mayergoyz, and C. Krafft, "Whole-track imaging and diagnostics of hard disk data using the spin-stand imaging technique," *J. Appl. Phys.*, vol. 97, 10P104, 2005.

48. C. Tseng, I. Mayergoyz, C. Tse, P. McAvoy, and C. Krafft, "Dynamic following of off-centered hard disk tracks in spin-stand imaging," *J. Appl. Phys.*, vol. 97, 10R301, 2005.

49. Guzik 1701-MP Spin-stand, Guzik Technical Enterprises.

50. R. C. Gonzalez and R. E. Woods, *Digital Image Processing*, pp. 613-615, Prentice Hall, Upper Saddle River, NJ, 2002.

51. Singiresu S. Rao, *Mechanical Vibrations (Third Edition)*, section 3.8, Addison-Wesley, 1995.

52. I. D. Mayergoyz, *Mathematical Models of Hysteresis and Their Applications,* chapter 1, Elsevier, New York, 2003.

53. X. Tan, J. S. Baras, P.S. Krishnaprasad, "Control of hysteresis in smart actuators with application to micro-positioning," *Systems Control Lett*., vol. 54, pp. 483–492, 2005.

54. S. Mori, M. Hatano, S. Aikawa, H. Takagi, Y. Shibuya, and K. Ouchi, "Highly precise actuator with PZT and displacement expander for track following," IEICE, Tech. Rep. MR2001–104, pp. 23–28, 2002.

55. S. Mori, T. Hoshino, G. Obinata*,* and K. Ouchi, "Air-bearing linear actuator for highly precise tracking," *IEEE Trans. Magn.*, vol. 39, pp. 812–818, 2003.

56. S. Mori, H. Tada, A. Naganawa, G. Obinata, and K. Ouchi, "Damping effect on precise track following for nano-motion actuator," *IEEE Trans. Magn.*, vol. 41, pp. 842–848, 2005.

57. W. E. Wong, L. Feng, G. Guo, W. Ye, and A. Al-Mamun, "Implementation of a servo positioning system on spin stand," *Proc 29th Annu. Conf. IEEE Industrial Electronics Society*, pp. 2114–2119, Roanoke, VA, Nov. 2003.

58. J. Liu, W. E. Wong, L. Feng, and G. Guo, "Implementation of a high performance multirate control system using PC," *Proc. IEEE Int. Conf. Power Electronics and Drive Systems*, pp. 636–641, Singapore, Nov. 2003.

59. W. E. Wong, L. Feng, Z. He, J. Liu, C. M. Kan, and G. Guo, "PC-Based Position Error Signal Generation and Servo System for a Spinstand," *IEEE Trans. Magn.*, vol. 41, pp. 4315–4322, 2005.

60. A. H. Sacks, "Position signal generation in magnetic disk drives," *Ph.D. Thesis*, Carnegie Mellon University, 1995.

61. R. D. Hampshire, L. R. McKenzie, P. R. Woods and C. E. Goodner, III, "Dynamic compensation of servo burst measurement offsets in a disc drive," U.S. Patent 5,774,297, June 1998.

62. H. Kupferman, "Disk drive having a disk including a servo burst pattern having a normal servo burst field and a quadrature servo burst field," U.S. Patent 6,980,389, December 2005.

63. C. J. Lee and C. Mavroidis, "PC-based control of robotic and mechatronic systems under MS-Windows NT workstation," *IEEE/ASME Trans. Mechatronics,* vol. 6*,* pp. 311–321, 2001.

64. H. N. Bertram and M. Williams, "SNR and Density Limit Estimates: A comparison of longitudinal and perpendicular recording," *IEEE Trans. Magn.*, vol. 36, pp. 4–9, 2000.

65. Shan X. Wang and Alexander M. Taratorin, *Magnetic Information Storage Technology*, p. 4, Academic Press, 1999.

66. S. Khizroev and D. Litvinov, *Perpendicular Magnetic Recording*, pp.1-22, Kluwer Academic, 2004.

67. R. H. Victora, J. Xue, and M. Patwari, "Areal density limits for perpendicular magnetic recording," *IEEE Trans. Magn.*, vol. 38, pp. 1886–1891, 2002.

68. I. Mayergoyz, C. Tse, C. Krafft, and P. McAvoy, "A novel approach to removing intersymbol interference from spin-stand images," *IEEE Trans. Magn.*, vol. 40, pp. 2197–2199, 2004.

69. M. J. Hassel, I. C. Felix, and C. E. Camp, "Modular unitary disk file subsystem with differing density zones," U.S. Patent 4,858,034, Aug 1989.

70. Maxtor's DiamondMax^{TM} 2160 Series, available at http://www.maxtor.com/_files/maxtor/en_us/documentation/manuals/dm2160_ultra_ata_manual.pdf

71. B. Carrier, *File System Forensic Analysis,* chapter 4, Addison-Wesley, 2005.

72. B. Carrier, *File System Forensic Analysis,* chapter 5, Addison-Wesley, 2005.

73. File System, available at http://en.wikipedia.org/wiki/File_system

74. Shan X. Wang and Alexander M. Taratorin, *Magnetic Information Storage Technology*, section 8.1, Academic Press, 1999.

75. M. Kurita, T. Yamazaki, H. Kohira, M. Matsumoto, R. Tsuchiyama, J. Xu, T. Harada, Y. Inoue, L. Su, and K. Kato, "An active-head slider with a piezoelectric actuator for controlling flying height," *IEEE Trans. Magn.*, vol. 38, pp. 2102–2104, 2002.

76. J. Juang, D. Chen, and D. B. Bogy, "Alternate air bearing slider designs for areal density of 1 Tb/in^2," *IEEE Trans. Magn.*, vol. 42, pp. 241–246, 2006.

77. T. Shiramatsu, M. Kurita, K. Miyake, M. Suk, S. Ohki, H. Tanaka, and S. Saegusa, "Drive integration of active flying-height control slider with micro thermal actuator," *IEEE Trans. Magn.*, vol. 42, pp. 2513–2515, 2006.

78. B. Carrier, *File System Forensic Analysis,* chapter 8, Addison-Wesley, 2005.

79. B. Carrier, *File System Forensic Analysis,* chapter 9, Addison-Wesley, 2005.

80. S. Ardalan, K. Raahemifar, F. Yuan and V. Geurkov, "Reed-Solomon encoder & decoder design, simulation and synthesis," *IEEE CCECE*, vol. 1, pp. 255–258, 2003.

81. Frequency Modulation (FM), available at

http://www.storagereview.com/guide2000/ref/hdd/geom/dataFM.html

82. Modified Frequency Modulation (MFM), available at

http://www.storagereview.com/guide2000/ref/hdd/geom/dataMFM.html

83. Shan X. Wang and Alexander M. Taratorin, *Magnetic Information Storage Technology*, section 8.3, Academic Press, 1999.

84. Shan X. Wang and Alexander M. Taratorin, *Magnetic Information Storage Technology*, section 8.2, Academic Press, 1999.

85. Run Length Limited (RLL), available at

http://www.storagereview.com/guide2000/ref/hdd/geom/dataRLL.html

86. S. A. Tretter, *Communication System Design Using DSP Algorithms*, chapter 9, Springer, 2003.